Direct observation of North Atlantic nutrient transport and biological pump variability linked to the Meridional Overturning Circulation

Lidia Carracedo

lidia.carracedo@ifremer.fr

University of Brest, CNRS, Ifremer, IRD, Laboratoire d'Océanographie 17 Physique et Spatiale (LOPS), IUEM, Plouzané, 29280, France https://orcid.org/0000-0003-3316-7651

Elaine McDonagh

NORCE Norwegian Research Centre, Bjerknes Centre for Climate Research, 19 Bergen, Norway; National Oceanography Centre Southampton, European Way, Southampton SO14 3ZH, UK.

Richard Sanders

NORCE Norwegian Research Centre, Bjerknes Centre for Climate Research, 19 Bergen, Norway; National Oceanography Centre Southampton, European Way, Southampton SO14 3ZH, UK.

C. Mark Moore

School of Ocean and Earth Science, National Oceanography Centre Southampton, University of Southampton, Southampton SO14 3ZH, UK.

Herle Mercier

University of Brest, CNRS, Ifremer, IRD, Laboratoire d'Océanographie 17 Physique et Spatiale (LOPS), IUEM, Plouzané, 29280, France https://orcid.org/0000-0002-1940-617X

Peter Brown

National Oceanography Centre Southampton, European Way, Southampton SO14 3ZH, UK. https://orcid.org/0000-0002-1152-1114

Sinhué Torres-Valdés

Alfred Wegener Institute, Am Handelshafen 12, 27570 Bremerhaven, Germany.

Edward Mawji

National Oceanography Centre Southampton, European Way, Southampton SO14 3ZH, UK.

Molly Baringer

NOAA/AOML, 4301 Rickenbacker Causeway, Miami, FL 33149, USA.

David Smeed

NORCE Norwegian Research Centre, Bjerknes Centre for Climate Research, 19 Bergen, Norway

Gabriel Rosón

University of Vigo, Campus Lagoas-Marcosende, 36200, Vigo, Spain.

Article

Keywords:

Posted Date: April 11th, 2024

DOI: https://doi.org/10.21203/rs.3.rs-4186952/v1

Additional Declarations: There is **NO** Competing Interest.

FRONT MATTER

Title

Direct observation of North Atlantic nutrient transport and biological pump variability linked to the Meridional Overturning Circulation

Authors

L.I. Carracedo[1*], E. McDonagh[2,3], R. Sanders[2,3], C.M. Moore[4], H. Mercier[1], P.J. Brown[3], S. Torres-Valdés[5], E. W. Mawji[3], M. Baringer[6], D. Smeed[2], and G. Rosón[7]

Affiliations

[1] University of Brest, CNRS, Ifremer, IRD, Laboratoire d'Océanographie Physique et Spatiale (LOPS), IUEM, Plouzané, 29280, France.

[2] NORCE Norwegian Research Centre, Bjerknes Centre for Climate Research, Bergen, Norway.

[3] National Oceanography Centre Southampton, European Way, Southampton SO14 3ZH, UK.

[4] School of Ocean and Earth Science, National Oceanography Centre Southampton, University of Southampton, Southampton SO14 3ZH, UK.

[5] Alfred Wegener Institute, Am Handelshafen 12, 27570 Bremerhaven, Germany.

[6] NOAA/AOML, 4301 Rickenbacker Causeway, Miami, FL 33149, USA.

[7] University of Vigo, Campus Lagoas-Marcosende, 36200, Vigo, Spain.

* Corresponding author: lidia.carracedo@ifremer.fr

Abstract

The ocean biological carbon pump (BCP) plays a pivotal role in the global carbon cycle. The BCP magnitude is determined by the fraction of nutrients utilised in biological production and remineralised at depth, with the remainder being subducted into the interior unused as 'preformed' nutrients. This fraction is currently around 50% and subject to the interaction of biological processes and global scale circulation. Consequently, changes in circulation can potentially impact biological carbon storage. Here we provide observational evidence that the reduction in the Atlantic Meridional Overturning Circulation (AMOC) that occurred over the 2004-2018 period has been accompanied by substantial changes in nutrient transports and associated carbon storage. Persistent southward net nutrient transport across 26.5°N exceeded nutrient sources, except by the end of the period when the system approached balance. This transient net loss of nutrients from the North Atlantic was accompanied by increases in the ratio of remineralized to preformed nutrients, indicating an increasing BCP efficiency (and carbon storage). Our results thus demonstrate observable transient changes in large scale nutrient transports linked to AMOC changes over interannual - decadal timescales, with implications for future ocean carbon storage.

MAIN TEXT

Introduction

The production, sinking and remineralisation of organic matter by the Biological Carbon Pump (BCP) stores enough carbon in the ocean interior to keep atmospheric CO_2 substantially lower (~200 µatm) than it would otherwise be[1,2]. It is often assumed that the BCP is operating in steady state, i.e. that the only perturbation to ocean fluxes is driven by the increase in anthropogenic CO_2 in the atmosphere invading the surface ocean. However, ongoing reductions in ocean oxygen concentrations[3] suggest that carbon storage by the BCP is increasing slowly, likely as a result of circulation changes[4–6]. Altered circulation can lead to an adjustment in BCP strength in a number of ways. Biological production is spatially heterogeneous, with, for example, elevated levels occurring in the North Atlantic Basin, where the upper limb of the Atlantic Meridional Overturning Circulation (AMOC)[7,8] and terrestrial and atmospheric processes introduce macronutrients (N, P, Si) and micronutrients (Fe) to the sea surface, allowing extensive phytoplankton blooms to occur[2]. The resulting organic material sinks through the water column and progressively remineralizes returning nutrients (henceforward termed remineralized, Fig. 1B) to the inorganic pool[9,10]. The BCP thus facilitates a downward diapycnal carbon and nutrient transfer that short-circuits physical advection. Any nutrients that remain unused at the surface at the end of the growing season due to, for example, iron limitation[11] are either retained within surface waters or subducted into the interior via newly formed deep water, unaccompanied by biologically fixed carbon (hence they are termed preformed, Fig. 1B), thereby not contributing to biological carbon storage[12]. The net contribution of a region to global carbon storage via the BCP is thus ultimately set by the processes determining the regional divergence of remineralized and preformed nutrients[9]. Integrated globally, the BCP is currently operating with about 50%

efficiency[9,13], as only around half of the total macronutrient supply to the surface is biologically utilised[10,13] the remainder being subducted back to depth within the preformed pool. Correspondingly, BCP efficiency (BCPe), as measured by the fraction of nutrients in the regenerated pool[9,10] (Fig. 1B), generally decrease from low to high latitudes, reflecting the generation of deep water masses containing preformed nutrients in (sub)-polar regions[9] (Fig. 1A).

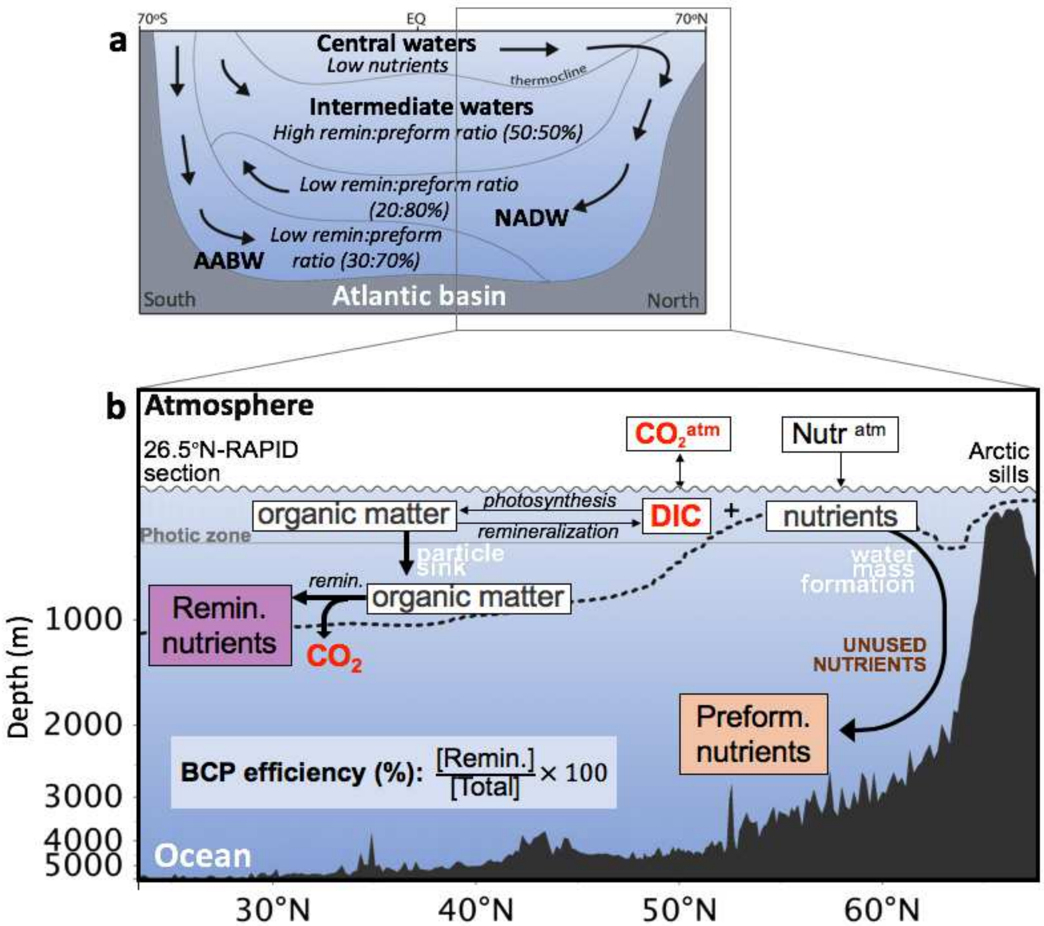

Fig. 1. Schematic of the nutrient content of the major water masses and the coupling between the CO_2 and nutrient cycles. (**A**) South to North view of the Atlantic meridional overturning circulation (AMOC). Arrows mark the approximate path of main water masses characterising the AMOC. NADW is North Atlantic Deep Water; and AABW, Antarctic Bottom Water. Nutrient fractions based on [14]. (**B**) Schematic diagram of the coupling between CO_2 and nutrient cycles in the North Atlantic. DIC refers to dissolved inorganic carbon, Remin. refers to remineralized and Preform. to preformed. Dashed line represents the σ_1 isopycnal (potential density referred to 1000 dbar) of 32.15 kg m^{-3}, broadly separating the upper and lower limbs of the AMOC[15,16]. Note that at 26.5°N this isopycnal is broadly equivalent to the ~1100 dbar pressure level[17].

Model simulations suggest that variability in ocean circulation can lead to changes in biological ocean carbon storage on multiple timescales[5,18–22]. Thus, although it is often assumed that the strength and efficiency of the BCP is invariant on multi-annual timescales (e.g. for anthropogenic carbon calculations[23,24]), large circulation variability patterns are expected to cause corresponding changes in the contemporary nutrient distribution (Fig. 2) and BCP strength (e.g. [15]), altering the biological component of ocean carbon storage over both short[15,25] and longer timescales[3–6,19,26].

Here we evaluate, based on observations, BCP functioning in the North Atlantic in terms of nutrient transports and convergence and the partitioning between preformed and remineralized pools and, ultimately, the biological component of oceanic CO_2 storage within the North Atlantic for the period 2004-2018 of observed reduced AMOC[27,28].

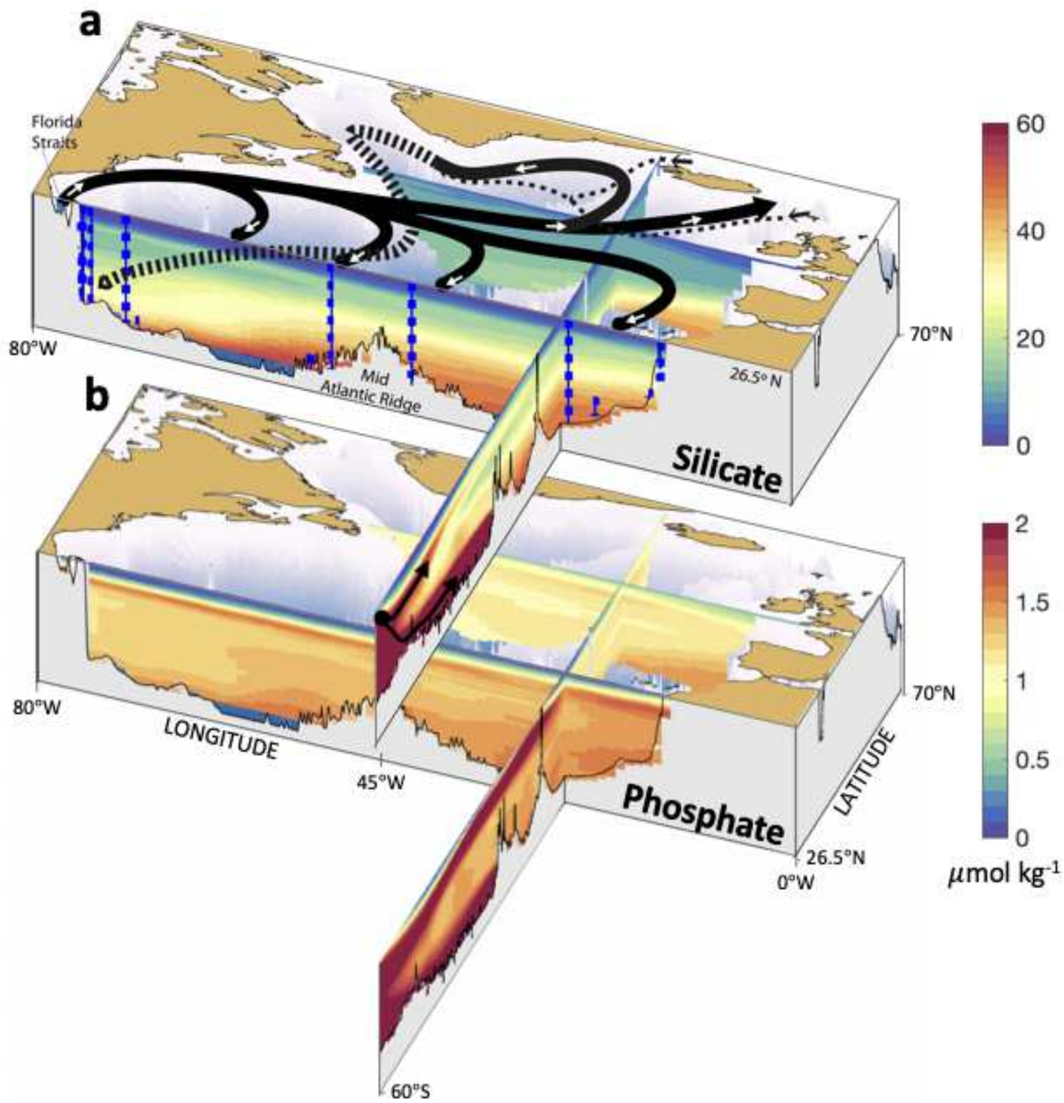

Fig. 2. Schematics of the nutrient distribution in the Atlantic Ocean. (**A**) Silicate and (**B**) phosphate distributions (in µmol kg^{-1}, source: WOA18 database). Thick black lines represent the upper circulation (gyre and upper Atlantic meridional overturning circulation, AMOC), the dashed black line marks the main path of the lower AMOC, and the dotted black lines account for the Arctic overflow contribution to the lower AMOC limb (Iceland and Denmark Strait overflow waters). Thin black arrows indicate the signature of the Antarctic Intermediate and Bottom Waters. The RAPID array of moorings used to measure the interior geostrophic transport is illustrated (blue dash-dot vertical lines).

Results

Time series of inorganic nutrient transport at 26.5°N

The RAPID array at 26.5°N in the North Atlantic (Fig. 2) has monitored the AMOC since 2004[29], providing volume[27,28,30], heat[31,32], freshwater[33] and anthropogenic carbon[34] transport estimates every 10 days along a transect which is regularly surveyed by trans-basin research GO-SHIP expeditions (fig. S1A). Here we combine observations from the international RAPID, Argo and GO-SHIP programs (see 'Data Sources' in Materials and Methods) (table S1) to generate time-varying inorganic nutrient (silicate, $Si(OH)_4$ or Si for simplicity; nitrate, NO_3^- or N for simplicity; and phosphate, PO_4^{3-} or P for simplicity) fields via a predictive Multi-Linear Regression (MLR, this study), and the existing locally interpolated regressions ESPER_LIR[35] and neural networks CANYON-B[36] and ESPER-NNs[35] (see Materials and Methods). Extensive sensitivity analyses indicate mean total nutrient transport uncertainties of up to 20% (more details are in the 'Nutrient transport uncertainties' and 'Sensitivity analysis' sections in Supplementary Methods) (tables S2 to S4), while the three independent methods resulted in no substantive differences to our analysis (fig. S2). For simplicity, we present the analysis using the MLR estimated in this study. The MLR-generated nutrient fields (fig. S3) are combined with the velocity fields from the freshwater calculation[33] to compute meridional nutrient transport every ten days for the period from 2004–2018. The time series (Fig. 3A to C) show total (net) southward transport of nutrients with mean values (± standard error) of -384 ± 16 kmol-Si s^{-1}, -170 ± 9 kmol-N s^{-1} and -11.8 ± 0.6 kmol-P s^{-1}, comparable to previous cruise-based estimates at the same location[37,38]. The time series also show considerable variability at a range of timescales from seasonal to interannual, with an overall change in total nutrient transport from being strongly southward at the beginning of the time series to rather less so later in the time series (more details in Supplementary Note 'Impact of interannual variability'). Hereafter we consider P, unless otherwise specified, noting that results are also supported by, and relevant to, Si and N.

Gyre vs overturning circulation counteracting role in the transport of inorganic nutrients

The nutrient transport across 26.5°N has two principal and largely opposing terms: the gyre (or horizontal) circulation component, and the overturning circulation component (eq. 10 in Materials and Methods). In agreement with former cruise-based inference[37], this study shows for the first time that the gyre component always (i.e. year-round) transports nutrients north, and the overturning predominantly south (Fig. 3A to C), although subject to seasonal-to-interannual variability, especially linked to the overturning component. The gyre-driven nutrient transport, mostly (>99%) constrained to the upper 1100 dbar, is the result of relatively high-nutrient waters (P = 0.60 ± 0.03 μmol kg^{-1}, table S5) advected polewards, mainly as part of a sub-surface 'nutrient stream' core[39] by the Florida and Antilles Currents (namely the Gulf Stream), and the eastern gyre recirculation at a lower transport-weighted property (nutrient transport divided by volume transport) (P = 0.34 ± 0.13 μmol kg^{-1}, table S5). Consequently, a balanced gyre flow leads to an unbalanced gyre-driven nutrient transport, directed northwards. The southward overturning transport of nutrients, which dominates the total nutrient transport (as depicted in the time series, Fig. 3; and fig. S4A to C), results from the recently ventilated nutrient-enriched North Atlantic Deep Water (NADW) having a transport-weighted preformed nutrient concentration in the lower limb of the AMOC (P = 0.95 ± 0.01 μmol kg^{-1}) that is much larger than that flowing northwards in the upper limb of the AMOC (P = 0.39 ± 0.08 μmol kg^{-1}) (table S5).

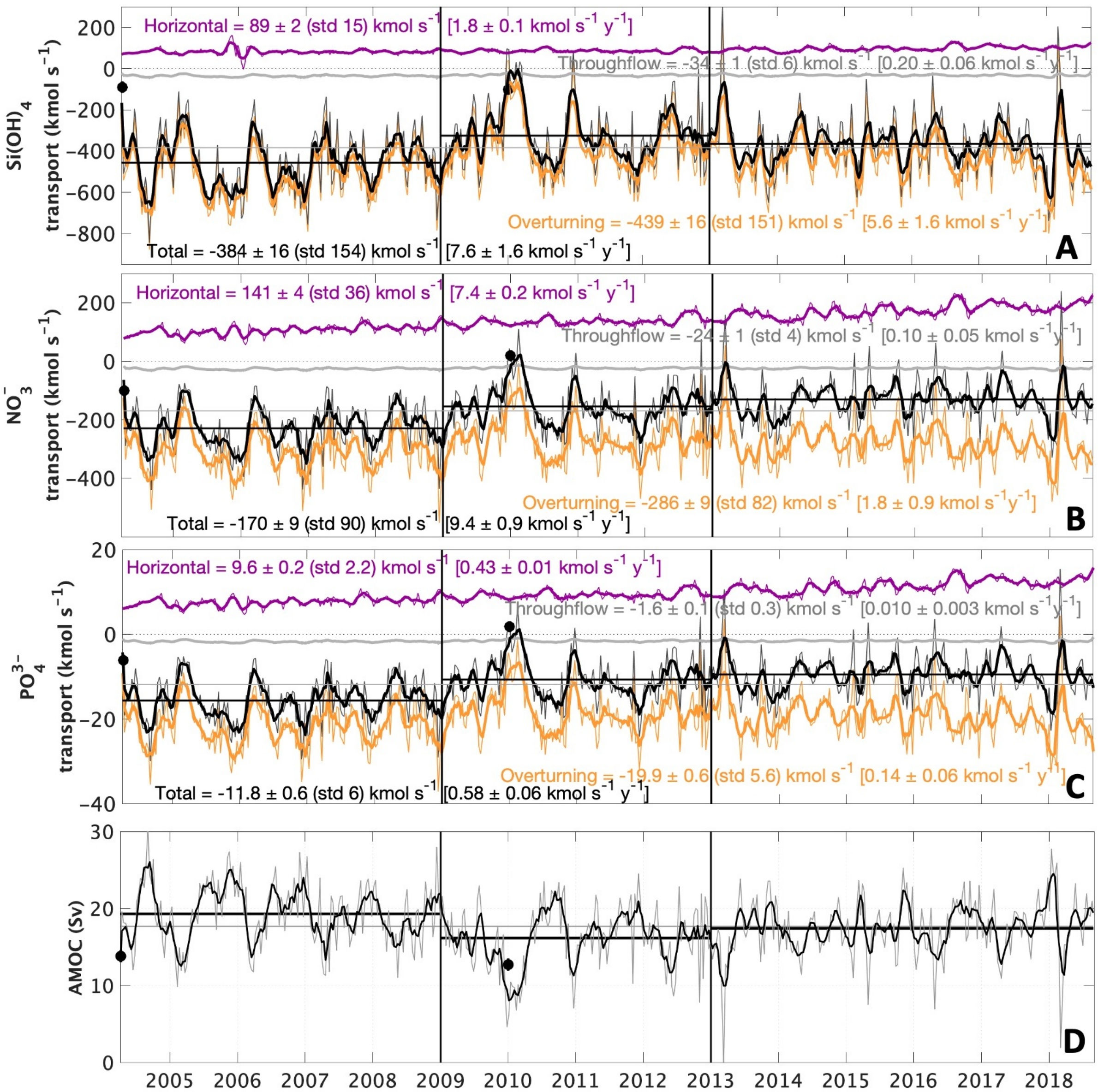

Fig. 3. Time series of inorganic nutrient transports across the 26.5°N section. Total (**A**) silicate, $Si(OH)_4$, (**B**) nitrate, NO_3^-, and (**C**) phosphate, PO_4^{3-}, transports (black), and their overturning (orange), horizontal (purple) and throughflow or barotropic (solid grey) components. Thin lines are the 10-day time series and bold lines are smoothed versions (moving average filter of 5-point running mean). Thin grey lines represent the total 2004-2018 mean transports, and thin black lines are the 2004-2009, 2009-2013 and 2013-2018 period averages. Coloured text/numbers are the 14-year averages ± standard error (negative fluxes mean southwards); in parenthesis, the standard deviation of the transports; and, in brackets, the model tendencies ±

standard error of the tendency (positive tendencies refer to an increase of transport to the North over time). Black dots are the hydrographic cruise-based estimates (cruise references in table S1). (**D**) Atlantic Meridional Overturning Circulation (AMOC) RAPID time series, as the sum of the Florida Current transport, the upper ocean (surface to 1100 dbar) geostrophic transport east of the Bahamas, and the Ekman transport[17].

Nutrient budgets north of 26.5°N

The total (net) southward transport of nutrients can be partially accounted for by sources of nutrients to the Atlantic north of 26.5°N. Potential sources are both internal, via lateral advection[7] [i.e., advection of inorganic nutrients across the Arctic Sills, and the Gibraltar Strait] or remineralization of organic matter, namely DOM, and nitrogen fixation north of 26.5°N; and external [e.g. rivers and atmospheric deposition] (more details are in the 'Nutrient sources' section in Supplementary Methods). We estimate that the total of these contribute 7 ± 1 kmol-P s^{-1} (table S6), around 44% of the total transport across the 26.5°N section at the beginning of the time series (16.0 kmol-P s^{-1}), and 59% of the mean southward 11.8 kmol-P s^{-1} transport across the 26.5°N section. Careful analysis of the uncertainties associated with these nutrient supply terms indicates that internal components constitute about 95% of the nutrient supply, with e.g. the Arctic Sills term having an uncertainty of around 17% derived from the range of transport estimates in the literature[40,41] (see 'Nutrient sources' section in Supplementary Methods). In contrast, external terms are minor components of the budget (e.g. [37,38,42]; 16% for Si, 36% for N, 5% for P, this study) implying that their associated large uncertainties (~100% in the case of atmospheric deposition) are unlikely to significantly affect the total.

We therefore suggest that the diagnosed total southward nutrient transport, particularly over the first half of the time series, represents a net loss of nutrients from the North Atlantic corresponding to around 1% per decade for P (and N) and 5% per decade for Si (see 'Total North Atlantic nutrient inventories' section in Materials and Methods), or put another way, a change of 0.03 μmol kg^{-1} for P (0.5 μmol kg^{-1} for N and 1.6 μmol kg^{-1} for Si) in the 14-year period, assuming that the change is spatially uniform. Evidence of decreasing mixed layer Si concentration in the subpolar North Atlantic of this order[43], supports this hypothesis. In contrast, the inferred changes in P concentrations are similar to the uncertainties in nutrient measurements[44]. Thus, the interior nutrient changes inferred from our new transport estimates would as yet remain undetectable. Although the observation-based inferred inventory/concentration changes remain uncertain, ECCO-Darwin model[45] output does show significant water-column nutrient concentration changes in the North Atlantic (Fig. 4A) and decreasing AMOC[46,47] for the period 2004-2018, which is consistent with a basin-average decrease in the North Atlantic nutrient inventories, in agreement with our results (more details in 'Total North Atlantic nutrient inventories' section in Materials and Methods).

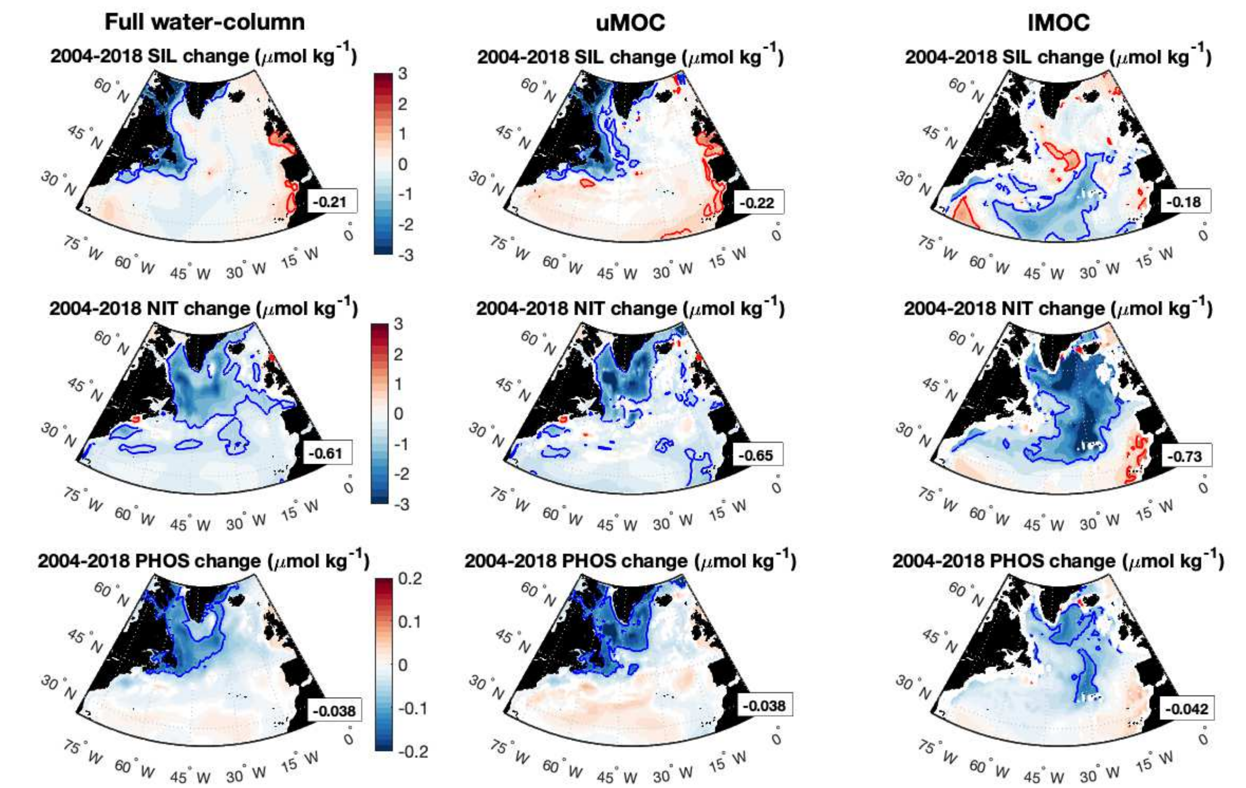

A

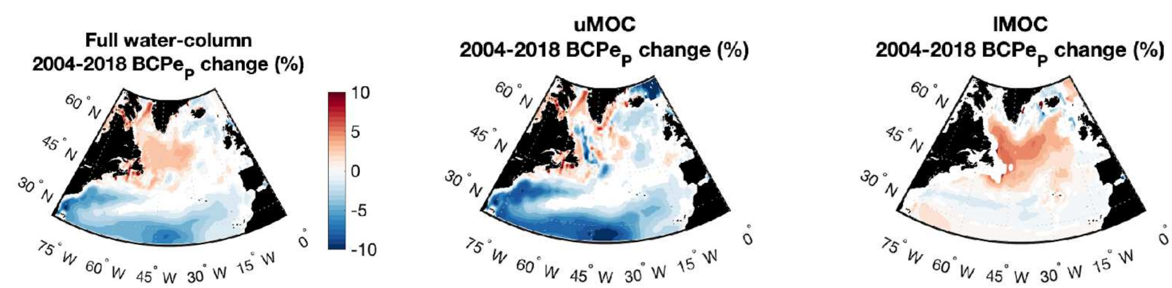

B

Fig. 4. 2004-to-2018 water-column nutrient and BCP efficiency (BCPe) change (in μmol kg^{-1}). (**A**) Full water-column (averaged) change (left panels); upper AMOC limb (averaged) change (central panels); and lower AMOC limb (averaged) change (bottom panels) over a 14-year (2004 to 2018) period for silicate (upper row), nitrate (middle row), phosphate (bottom row). Negative (positive) values indicate a decrease (increase) in nutrient concentration (first to third rows). Thick colour lines indicate the minimum concentration-change required (0.68 μmol-Si kg^{-1}, 0.69 μmol-N kg^{-1}, and 0.09 μmol-p kg^{-1}) for it to be robustly detectable by observations (see main text for explanation). Numbers in the inset box represent the average value for the whole region. Upper-lower AMOC interface was chosen at the σ1 isopycnal (σ1 is the potential density referenced to 1000 dbar) 32.15 kg m^{-3} [15,16]. (**B**) Same as A but for BCPe, as estimated from phosphate concentrations (see Materials and Methods for details). Data source: ECCO-Darwin Data-Assimilative Global Ocean model by [45].

We propose that the observed non-steady state behaviour of nutrient transports across the 26.5°N section at multiple time scales (Fig. 3) will be related to differences between the timescales of circulation changes (seasons-decades, Fig. 3D) and corresponding dynamic adjustments to such circulation-state variations (days-weeks) and the much longer advective timescales for nutrients in this system (decades and longer). To illustrate this in the context of the AMOC we considered a simplified conceptual case of the expected consequences of an AMOC slowdown (see ‘Conceptual Model’ section in Materials and Methods). Starting from a steady state scenario (Fig. 5A, panel 1) with a balanced nutrient budget, an assumed perturbation through reducing volume transports which maintained export production at the same rate (Fig. 5A, panel 2) would result in sinking organic matter now being remineralised into a reduced flow of water (Fig. 5A, panel 2). However, due to the advection timescale, the preformed nutrient concentration within the lower AMOC limb water mass could initially remain unchanged, leading to a larger preformed nutrient concentration in the lower limb than in the upper limb and hence a larger nutrient transport south. However, as a larger fraction of the nutrient advected north across the section is used in export production under this scenario (from 6 out of 20 kmol s^{-1}, Fig. 5A, panel 1; to 6 out of 10 kmol s^{-1}, Fig. 5A, panels 2 and 3), eventually (over 10s to 100s of years, fig. S5) the reduced nutrient water would advect around the overturning cell leading to the establishment of a new steady state (Fig. 5A, panel 3).

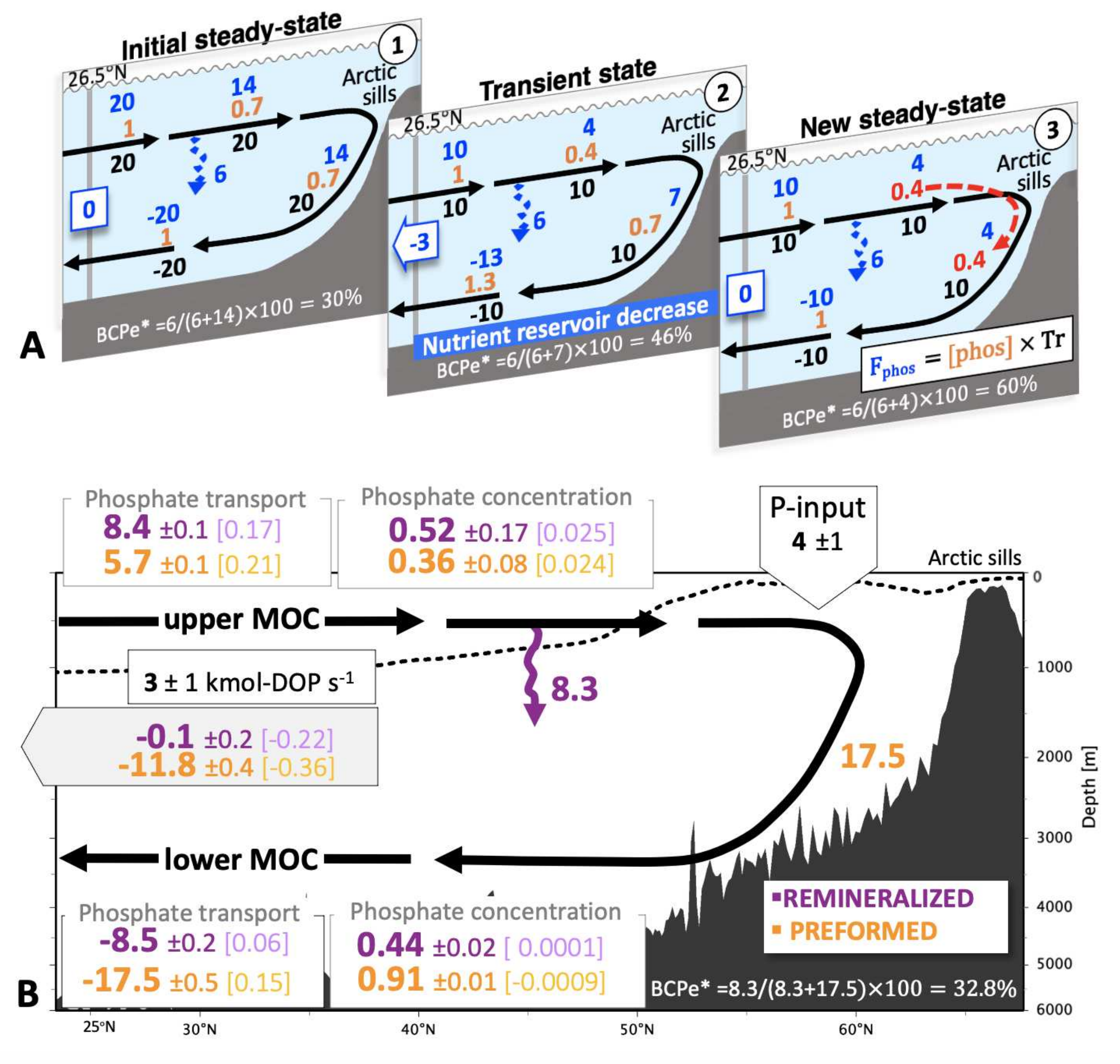

Fig. 5. Changes in the North Atlantic nutrient inventory in response to the Atlantic meridional overturning circulation (AMOC). (**A**) Conceptual model of the nutrient inventory variability as result of an assumed AMOC slowdown. Black arrows represent the simple schematic of the AMOC, and dashed blue arrows the vertical transfer of nutrients by remineralization of organic matter sinking through the water column. Blue numbers are indicative phosphate transports (kmol s^{-1}); orange/red numbers are phosphate concentrations (µmol kg^{-1}); and black values are volume transports (Sv, 1 Sv = 10^6 m^3 s^{-1}). BCPe* refers to the biological carbon pump efficiency proxy (see eq. 7 in Materials and Methods). Note the transient state (panel 2) reflects changes first felt in the upper AMOC that aren't yet transmitted to depth (red dashed arrow in panel 3). (**B**) Schematics of the actual remineralized and preformed phosphate 2004-2018 mean transports. Dashed line is the σ_1 isopycnal (potential density referred to 1000 dbar) of 32.15 kg m^{-3}, broadly separating the upper and lower limbs of the AMOC. Pink arrow represents the vertical nutrient transfer as result of the export production. Pink (orange) numbers are the remineralized (preformed) phosphate average transports (kmol s^{-1}); and values in brackets are the tendencies over the period of study (kmol s^{-1} yr^{-1}). Numbers in the grey shaded boxes are net transports (i.e., include horizontal and overturning transports) across the 26.5°N section. Black

numbers refer to other inputs of phosphorus (kmol s^{-1}): additional nutrient sources north of 26.5°N (P-input), and net transport of dissolved organic phosphorus (DOP) across 26.5°N.

Overall, the reduction in the overturning-driven southward nutrient transport and the increase in the northward gyre-driven transports, appeared to bring the system closer to balance over the observation period. Indeed, towards the end of the time series the total (southward) nutrient transport is so reduced that the total net transport approaches zero once an estimated 7 ± 1 kmol-P s^{-1} integral source is included (Fig. 3), that is the system is close to balance for P and N (i.e. nutrient ocean divergence in balance with additional nutrient sources). In contrast to P (and N), Si is still far from balance by the end of the period, with the total (southward) Si transport exceeding (by 3 times) the estimated additional Si sources (117 ± 12 kmol-Si s^{-1}).

Overturning regulation of the remineralized:preformed nutrient pool north of 26.5°N

Decomposing nutrient transports further into preformed and remineralized constituents (see 'Remineralized and preformed nitrate and phosphate' section in Materials and Methods), we find that the 14.2 ± 0.3 kmol P s^{-1} (table S5) transported north by the upper limb of the AMOC (i.e. surface-to-0-1100 dbar integrated transport, thus comprising the gyre circulation), is predominantly in the remineralised fraction (8.4 ± 0.1 kmol P s^{-1}), compared to a return flow at depth which is carrying a lower remineralised (-8.5 ± 0.2 kmol-P s^{-1}) and higher preformed (-17.5 ± 0.5 kmol-P s^{-1}) burden (Fig. 5B, table S5). This result highlights that the preformed fraction is predominantly within (and associated with) the lower AMOC limb (the overturning component), whereas the remineralized fraction is split between the upper and lower AMOC limbs, with a slight dominance of the gyre component over the overturning component (table S5). With the remineralized total transport by the upper and lower AMOC limbs being in balance on average (observation-period average of 0 ± 0.2 kmol-P s^{-1}, table S5), the preformed nutrient pool is mainly responsible for the total net southward nutrient transfer from the North to the South Atlantic Basins. Notably, the remineralized transport changed from being southwards during the first half of the time series to being positive afterwards (fig. S6). Observing that by the end of the period the system was close to balance (i.e. nutrient ocean divergence in balance with additional nutrient sources), we can argue that the apparent convergence of remineralized nutrients north of 26.5°N in the Atlantic by the end of the period (of 1.6 ± 1.1 kmol-P s^{-1} on average for the last half year of the time series) is indicative of a transient net loss of biologically fixed carbon at high latitudes (of up to 0.07 ± 0.05 Pg-C yr^{-1}).

The observed AMOC variability and associated slowdown (Fig. 3D) is further reflected in the balance between the preformed and remineralized pools, and hence BCPe. Noting that the presented tendencies can only currently be interpreted in terms of a transient state over the observed period (i.e., interannual to decadal timescales), the decomposed remineralised and preformed (transport-weighted) concentrations and transports also show significant tendencies over the time series (Fig. 5B, table S5). Focusing on the overturning component, both the remineralized and preformed nutrient overturning transports became less southward (0.03 ± 0.02 and 0.12 ± 0.04 kmol-P s^{-1} yr^{-1}, respectively, table S5), co-incident with the reduction of the AMOC over the time period[27,28] (Fig. 3D). The AMOC variability dominates change in the overturning component (91%, table S7), with the southward transport of preformed nutrients decreasing at a faster rate (0.12 ± 0.04 kmol-P s^{-1} yr^{-1}) than the transport of remineralized nutrients (0.03 ± 0.02 kmol-P s^{-1} yr^{-1}) (table S5). The decrease in the preformed nutrient overturning transport southward (0.12 ± 0.04 kmol-P s^{-1} yr^{-1}, table S5) is driven by both the AMOC reduction (explaining >90% of the total tendency, table S7) and reduction in preformed transport-weighted nutrients in the lower AMOC limb (-0.0009 ± 0.0005 μmol-P kg^{-1} yr^{-1}, Fig. 5B, table S5). In contrast, the decreasing remineralized nutrient overturning transport southward (0.03 ± 0.02 kmol-P s^{-1} yr^{-1}, table S5) is driven by a decreasing AMOC (explaining ~70% of the total tendency, table S7) but dampened by a slight (though non-significant) increase in the remineralized transport-weighted nutrient concentration in the lower AMOC limb (0.0001 ± 0.0002 μmol-P kg^{-1} yr^{-1}, Fig. 5B).

In the case of the total tendency (decrease) in the net total southward nutrient transport (Fig. 3, Table S7), it is important to remark that the overturning component (and ultimately, the AMOC magnitude) only dominates the signal for Si. For N and P, however, the changes in the upper AMOC limb, dominated by increasing (remineralized and preformed) nutrient concentrations and mostly linked to the horizontal component, are more substantial in decreasing the net southward nutrient transport that the corresponding changes in the lower AMOC limb.

Regardless of the driver, the relative changes in the lower AMOC limb volume transport and N and P transports indicate increasing transport-weighted remineralized nutrients relative to transport-weighted preformed nutrients, and hence an increased efficiency of the BCP north of the section. Based on our time-series results, we infer a BCPe* proxy (eq. 7 in Materials and Methods) in the deep North Atlantic of 32.4% (±1.2%), as an average for the 14-year time period (Fig. 5B), and an overall small (but significant) increase of 0.5% (±0.1%) for the 2004-2018 period; 1.7% (±0.3%) increase for the 2004-2010 period of the AMOC slowdown). Thus, at a time of reduced deep-water production and overturning strength[27,29], the BCPe* increase appears to be dominated by the reduced production of deep preformed nutrients (as depicted in our conceptual model, Fig. 5A) and the increase in the (remineralized) fraction (Fig. 3A to C). However, the direct estimate of the BCPe term as the ratio of remineralized to total nutrient concentration at the section (as defined in eq. 6 in Materials and Methods), indicate relative changes in the nutrient concentrations through time compatible with reduced BCPe in the lower AMOC limb at 26.5°N. To better understand this apparent inconsistency, we computed the BCPe change for the period 2004-2018 in the North Atlantic basin by means of the nutrient and oxygen data from the ECCO-Darwin model[45] (Fig. 4B). This 3D spatial view allows us to see that there is a subpolar vs subtropical dipole pattern north/south of 45°N of increasing (decreasing) BCPe (water-column average) in the subpolar (subtropical) region (Fig. 4B, first panel). Even if by looking at the lower AMOC BCPe average (Fig. 4B, third panel) such a dipole weakens at the expense of the increasing BCPe pattern, yet a latitudinal band of decreasing BCPe nearby 30°N can be identified, which could explain our results at 26.5°N.

Discussion

The current study provides an observational basis indicating a major role for AMOC variability in North Atlantic nutrient cycling on all of the time scales considered. For the full time series the AMOC strength describes >80% of the variability in the total nutrient transports (~90% for Si, ~80% for N and P), whereas the horizontal circulation and nutrient concentration changes in the upper AMOC limb also play an important role in the decadal tendencies for N and P.

The additional nutrient sources are minor components of the budget (e.g. [37,38,42]; this study). Hence, even if the anthropogenic sources are increasing[11,48–52], they are unlikely to significantly affect (overcome) the total convergence/divergence advective term. Hence, we hypothesise that AMOC variability is a potential mechanism by which the North Atlantic seems to be 'losing' nutrients (Si particularly). Clearly the real situation is more complex, and a number of potential caveats likely apply to the presented simplified scenario (Fig. 5). If, for instance, some other perturbation enhanced (reduced) export productivity and/or deepened (shallowed) the remineralization depth, this could cause a magnified (decreased) vertical nutrient gradient and, ultimately, the transient net southward nutrient transport would be enhanced (reduced). This might be particularly relevant to the observed imbalance in the Si budget, which is the largest of the three nutrients considered ([15]; this study). For example, any decrease in diatom contribution to phytoplankton communities at high latitudes[53,54] might be hypothesized to result in slower/shallower sinking organic matter (i.e., biologically-mediated carbon export radio decrease) and hence a strengthening of the vertical Si gradient which could increase the upper/lower AMOC limb imbalance. However, irrespective of the details, differences between the circulation change (AMOC + gyre circulation) and nutrient anomaly advection timescales (Fig. 5) should always ultimately result in the former influencing the inventories of nutrients which are dictated by the latter. Observations suggest this decoupling between the AMOC and ocean interior property fields is larger than previously thought[55].

Our results have also shown that towards the end of the time series (i.e. 2018) the overturning component was so reduced that the total net transport approached zero once the additional nutrient sources were taken into account. Hence, this may be indicative of an ongoing transition from a transient-state scenario towards a plausible new steady-state (i.e. advection and nutrient sources/sinks in balance) or, more likely, a point within ongoing AMOC secular variability[56–58] where the basin becomes net convergent for nutrients for a period (see fig. S7). Moreover, the inferred net loss of nutrients from the basin over the study period further implies that at some stage in the past (potentially over centennial timescales[59]) nutrient transports must have been such that a convergence within the basin occurred. Continuous monitoring of the meridional basin-scale tracer transports will be crucial if we aim to build time series long-enough to diagnose long-term anthropogenic signals and the impact of extreme events (i.e. the 2009/2010 abrupt AMOC slowdown) on these long-term signals and differentiate those from other natural variability patterns. Providing observational evidence of the tracer ocean variability at these time scales will be key to improving climatic predictions.

Our calculations also demonstrate that the preformed nutrient pool is predominantly responsible for the total southward nutrient transport from the North to the South Atlantic basis, with the transport of remineralized nutrients by the upper and lower AMOC limbs being mostly in balance. We contemplated that the vigour of deep-water formation (the source waters for the AMOC lower limb) controls the preformed nutrient concentration in deep-water formation regions. The changes which occurred during the 2004-2018 time period further point to a feasible reorganization between the remineralized (increasing remineralized fraction) and preformed (decreasing preformed fraction in the lower AMOC limb) nutrient pools in the North Atlantic, which is broadly as predicted by models[5,22,60]. Collectively, this study provides new observational evidence of large-scale reorganization of nutrient pools and the associated BCP efficiency over multi-annual – decadal timescales in response to changing AMOC. The assessment of the remineralized vs. preformed nutrient pool ratio variability proves to be a useful metric of integral BCP changes[6], and so we advocate for the consideration of this kind of basin-scale calculations in BCP research to advance its understanding in a changing climate.

Overall and consistent with our observations, by slowing down the overturning circulation as most climate models predict in the coming century[61], we would expect that the North Atlantic begins to resemble more and more the North Pacific, where the regional BCP efficiency is higher[9], due to less vigorous generation of deep waters.

Materials and Methods

Data sources

Datasets used in this study were:

(i) 10-day resolution velocity fields used for the freshwater flux time series calculation at 26.5°N[33], obtained by means of transport estimates from the UK-US 26.5°N RAPID array (see Fig. 2 in [29]), Ekman transport from ERA-Interim winds[62], and submarine cable-based estimates of transport through the Florida Straits at 27°N[63].

(ii) Salinity (S) and potential temperature (θ) fields from an Argo-derived optimal interpolation (OI) product[33]. The source data are Argo temperature and salinity profiles with a quality control (QC) flag of 1 (good data), and the gridded mooring temperature and salinity data from the RAPID-Array moorings in the upper interior (upper 1760 dbar, 1 dbar = 10^4 Pa). The OI produces gridded fields of temperature and salinity on a 0.25° longitude grid at 26.5°N down to 2000 dbar every 10 days (the repeat profiling period of most Argo floats), and at each time-step, the S and θ grids are completed to bottom[33]. The 10-day S and θ fields are referred to in this study as the 26.5°N-RAPID dataset.

(iii) Historical hydrographic oxygen and nutrient bottle data from seven transatlantic hydrographic repeats at 24.5°N (fig. S1A): 1981 (available at the Word Ocean

Database), 1992, 1998, 2004, 2010, 2011, 2015 (all available at the GLODAPv2.2021 database[64]), and 2020 (available at CCHDO); and ten additional hydrographic repeats at Florida Straits: 2012 GOMECC (Gulf of Mexico and East Coast Carbon) cruise, 2015 NOAA-ABC (Atlantic BiogeoChemical Fluxes) cruises (4 repeats), 2016 NOAA-ABC (5 repeats) (table S1).

(iv) Additional nutrient sources in the North Atlantic. Data sources and their references are summarized in table S6 (more details in the 'Nutrient sources' section in Supplementary Methods).

(v) Inorganic nutrient and oxygen data from the World Ocean Atlas 2018 (WOA18)[65]. Annual nutrient fields were used to illustrate the nutrient distribution in the Atlantic Ocean in Fig. 2, and to estimate the mean nutrient inventories (see 'Total North Atlantic nutrient inventories' section). Seasonal WOA18 oxygen-adjusted fields were used as input variable to the MLR method (more details in the next section).

(vi) Further additional data used to complement the study are: inorganic nutrient and oxygen data from the ECCO-Darwin Data-Assimilative Global Ocean model[45], to look at the model nutrient change (2004-to-2018) at a larger spatial scale (North Atlantic basin) (Fig. 4); and velocity and nitrate monthly fields from the 1° NEMOv3.2-MEDUSA-2.0 ocean model[66] between 1980 and 2100 at 26.5°N, to assess the MLR method ('Sensitivity analysis' section in Supplementary Methods), and to look into end-of-century tendency-prediction (fig. S5).

Multilinear Regression method applied to nutrients

Multi-Linear Regression (MLR) models describe the relationship between a dependent variable y_i (also called response variable), and independent variables X_{ip} (also named explanatory or predictor variables), in the form:

$$y_i = c_0 + c_1 X_{1i} + c_2 X_{2i} + \ldots + c_n X_{ni} + \varepsilon, \quad (1)$$

$$i = 1, \cdots, \text{number of observations}$$

$$n = 1, \cdots, \text{number of predictor variables}$$

where c_n are the *nth* coefficients, i.e., the regression parameters that are determined by a simple linear square regression, and c_o is the constant term in the model. The term ε represents the model residual.

In order to reconstruct time-varying nutrient fields (every 10 days), we used *in situ* data from the hydrographic repeats at 24.5°N to calculate nutrients (silicate, nitrate, or phosphate) from a predictive linear regression based on temperature, salinity, oxygen, pressure and time, as follows:

$$N_{obs} = c_0 + c_1\, \Theta_{obs} + c_2\, S_{obs} + c_3\, O_{2obs} + c_4\, P_{obs} + c_5\, lon_{obs} + c_6\, t_{obs} + \varepsilon = N_{model} + \varepsilon, \quad (2)$$

where the subscript 'obs' refers to the data field used as input to the MLR, with N referring either to silicate, nitrate or phosphate, Θ to potential temperature, S to salinity, O_2 to oxygen, P to pressure, lon to longitude, and t to time. Input data correspond to nine different hydrographic cruises spanned between August 1981 and March 2020, including the most recent A05 DY040 and JC191 cruise data (table S1, fig. S1A). We conducted a sensitivity test by modifying the amount of input data used to compute the MLR algorithms (further details in the 'Sensitivity analysis' section in Supplementary Methods). We applied a backward stepwise MLR method, i.e., departing from all the parameters, the adjustment iterated removing each time those variables whose *p-value* exceeded by 0.1. In other words, at each iterative step, the function searches for terms to remove from the model based on the value of the 'Criterion' argument (in our case, a p-value of 0.1). Note *p-values* range between 0-1, so that the closer the *p-value* is to 0, the more significant the predictor variable is to the correlation. Despite the existence of correlations and collinearity among a number of predictors, from a predictive point of view they should not be removed if their presence improves the prediction. The MLR was applied separately for each nutrient (silicate, nitrate and phosphate) and for each of the different regions or MLR-boxes into which the section was spatially divided (fig. S1B), thus obtaining as many MLR equations by nutrient as subregions defined (table S8). The MLR-box definition has a negligible impact on results ('Sensitivity analysis' section in Supplementary Methods). Residuals, that is, differences between the observed nutrient value N_{obs} and that predicted by the model N_{model} (ε in eq. 2), are shown in fig. S8. Overall, the percentage of variance of the nutrient fields explained by the predictive variables ranged between 41 to 99% in the case of silicate, between 19 to 99% for nitrate, and 11 to 99% for phosphate (R^2, table S8), with an average (excluded the mixed layer) of 85%, 74% and 75% of variance of the nutrient fields (silicate, nitrate and phosphate, respectively) explained by the predictive variables.

The MLR equations thus obtained were then applied to the 10-day resolution 26.5°N-RAPID potential temperature and salinity datasets and the WOA18 oxygen-adjusted fields, for the period between April 2004 and August 2018, to generate a nutrient field $N_{model}(x,z)$ at each time step. As illustration, fig. S2 shows the average of the 14-year MLR-derived nutrient fields. It is important to note that contrary to the 26.5°N-RAPID potential temperature and salinity datasets, original WOA18 oxygen fields represent seasonal climatological means and, therefore, lack any temporal trend. We therefore used WOA18 oxygen-adjusted fields. The term adjusted refers to a correction offset added at each grid point and time-step, which was calculated based on the observational oxygen tendencies estimated by means of the hydrographic data (table S9). The overall impact on results of using WOA18 data with/without adjusted tendency, as well as the impact of not using oxygen at all as a predictive variable, was assessed in the 'Sensitivity analysis' section in Supplementary Methods.

Following [34], the Florida Straits box was treated separately from the MLR analysis. For the Florida Straits the high-frequency velocity at each grid point is not available, but a velocity profile based on the high-frequency time series of subsea-cable-derived volume transport estimates is used instead[63]. Based in the method applied by [33], we used the 2004, 2010, 2012, 2015 and 2016 cruise data at the Florida Straits (gridded nutrient distributions and absolute transports) to estimate *a)* the Florida Straits transport-weighed nutrients (i.e., Florida Strait nutrient transport divided by volume transport), N_{obs}^{t} (fig.

S9A), in analogy to [33]; and *b)* transport-weighted nutrient profiles, N_{obs}^{t} (z) (not shown). The latter were used to create temporally predictive regressions according to:

$$N_{obs}^{t}(z) = c(z)\, t_{obs}, \tag{3}$$

with N_{obs}^{t} (z) the transport-weighted nutrient profile as estimated from hydrographic data, t_{obs} the time of the cruise, and c(z) the slope of the linear fit given by the model at each depth level z (fig. S9B). Once c(z) is obtained from observations, we estimated the time-varying nutrient profile at the 10-day RAPID time resolution according to:

$$N_{RAPID}^{t}(z) = c(z)\, t_{RAPID} \tag{4}$$

Neural Network and Empirical Seawater Property Estimation Routines applied to nutrients

We additionally generated MLR-independent time-varying nutrient fields by means of more sophisticated neural network (NN) approaches, using pressure, temperature, salinity, oxygen, location, and time as predictors: CANYON-B[36], and the more recent Empirical Seawater Property Estimation Routines (ESPERs)[35]. ESPER routines provide estimates from both neural networks (ESPER_NN), and locally interpolated regressions (ESPER_LIR) (fig. S2). Another advantage of ESPER is that macronutrients (silicate, nitrate and phosphate) can be predicted when given at least two predictors (e.g., temperature and salinity, here referred to as ESPER_LIR_TS), thus allowing us to provide an estimate of nutrients not impacted by the use of WOA18 oxygen data as an input variable to the predictive algorithms ('Sensitivity analysis' section in Supplementary Methods; test 3, table S3).

Remineralized and preformed nitrate and phosphate

In order to put the lateral exchange of nitrate and phosphate into the context of the BCP, we deconvolved the MLR-derived 10-day resolution nitrate and phosphate fields into their preformed ($[NO_3^-]^0$, $[PO_4^{3-}]^0$) and remineralized ($[NO_3^-]^{rem}$, $[PO_4^{3-}]^{rem}$) fractions. The preformed fraction accounts for the nutrient concentration a water mass had when it was being formed in its source region; and the remineralized fraction accounts for those nutrients that are regenerated due to biological respiration of the organic matter at subsurface/depth levels. So that nutrient decomposition is expressed as:

$$[NO_3^-] = [NO_3^-]^0 + [NO_3^-]^{rem}$$

$$[PO_4^{3-}] = [PO_4^{3-}]^0 + [PO_4^{3-}]^{rem} \tag{5}$$

where $[NO_3^-]^{rem}$=AOU/$r_{O/N}$ and $[PO_4^{3-}]^{rem}$=AOU/$r_{O/P}$, with $r_{O/N}$ and $r_{O/P}$ the Redfield remineralization ratios (with $r_{O/N}$= 10.5 and $r_{O/P}$ = 175, [67]) and AOU is the apparent oxygen utilization, that is, the oxygen consumption due to respiration of the organic matter: AOU= O_2^{sat} - O_2, where O_2 is the measured concentration, and O_2^{sat} the oxygen saturation value. To assess the impact of using constant stoichiometric ratios, we conducted a sensitivity test by modifying the main components of organic matter, the nitrogen:carbon ratio ($r_{N:C}$) and the phosphorus:carbon ratio ($r_{P:C}$), between a minimum and maximum value ([min, max]) according to the observed ranges of marine organic matter composition[40,68]: $r_{N:C}$=

[8, 24]:117, and $r_{P:C}$= [0.5,1.5]:117; i.e., $r_{O/N}$= [7, 21] and $r_{O/P}$ = [113, 340] (further details in the 'Sensitivity analysis' section in Supplementary Methods). Remineralized and preformed nitrate and phosphate distributions are shown in fig. S3D to G.

We also inferred from our time series the biological carbon pump efficiency (BCPe) at 26.5°N in function of time (t), defined as the fraction of nutrients in the remineralized pool (remin) to the total inorganic nutrient (total) pool[9,10] (as in Fig. 1A):

$$BCP_e(t)\ [\text{in\%}] = \overline{[\mathrm{N}]}^{\mathrm{remin}}_{\mathrm{lAMOC}} / \overline{[\mathrm{N}]}^{\mathrm{total}}_{\mathrm{lAMOC}} * 100 \qquad (6)$$

where N refers either to nitrate or phosphate at the 26.5°N section, and the upper bar refers to the section average at the lower AMOC limb (subscript lAMOC). If averaged over the full time period, then we refer to BCP_e.

In addition to the above definition, and based on our nutrient transport time series, we also inferred the BCPe north of the 26.5°N section by means of a BCPe proxy (BCPe*), estimated as the rate of remineralized transport of nutrients by the lower AMOC (F_{Nrem}^{lAMOC}) to the total inorganic nutrient transport by the lower AMOC (F_{Ntotal}^{lAMOC}) at 26.5°N (as in Fig. 5A):

$$BCP_e^*(t)\ [\text{in\%}] = \mathrm{F}^{\mathrm{lAMOC}}_{\mathrm{Nrem}}(t) / \mathrm{F}^{\mathrm{lAMOC}}_{\mathrm{Ntotal}}(\mathrm{t}) * 100 \qquad (7)$$

Finally, the BCPe term was also directly computed for the whole North Atlantic basin based on the ECCO-Darwin model data, equivalently to equation (6). In this case, the BCPe average was done by the lower AMOC limb, the upper AMOC limb or for the full water column (Fig. 4B).

Continuous nutrient fluxes and transport decomposition

The nutrient flux perpendicular to the 26.5°N section is defined as

$$F_N(t) = \iint \rho(x,z,t)\, N(x,z,t)\, v(x,z,t)\, dx\, dz, \qquad (8)$$

where F_N is given by spatial integration (with x the section coordinate, and z the vertical coordinate, i.e. depth, in m) of the nutrient field N (with N the general notation for silicate, $Si(OH)_4$; nitrate, NO_3; or phosphate, PO_4^{3-}, as obtained from the MLR method -or also as obtained by CANYONB or ESPER; or nitrate and phosphate preformed and remineralized fractions, as obtained from equation (5), multiplied by the (absolute) velocity orthogonal to the section, v(x,z,t). ρ(x,z,t) refers to seawater density. For the Florida Straits the velocity at each grid point is not available, but a velocity profile is used instead[63], so that in this particular region the nutrient transport estimate, $F_N^{FS}(t)$, is given by

$$F_N^{FS}(t) = \int N^t(z,t)\, v(z,t)\, dz, \qquad (9)$$

where N^t is the nutrient concentration obtained according to equation (4). $F_N^{FS}(t)$ time series is shown in fig. S9C, where we also tested the impact of using, instead of the time-variant transport-weighted nutrient profile, $N^t(z,t)$, either a time-variant transport-weighted property, $N^t(t)$, or an averaged transport-weighted property, $\overline{\mathrm{N^t(t)}}$. Combining Florida Straits nutrient transports with ocean interior analogues yields ten-day nutrient transports across 26.5°N, as shown in Fig. 3. The total nutrient time series recalculated with the

CANYONB_NN-derived, ESPER_NN-derived, ESPER_LIR-derived and ESPER_LIR_TS-derived ocean interior nutrient fields (instead of the MLR-derived nutrient fields) are shown in fig. S2. The results from ESPER compared better to the MLR than those from CANYON-B, our results lying in between those from ESPER_NN and ESPER_LIR. But overall, the nutrient transports by using CANYON-B or ESPER did not show significant differences to those based on the MLR in neither their magnitude, variability nor the linear tendencies. Additionally to the nutrient transport time-series, hydrographic cruise-based estimates by [15], based on the 2004 and 2010 24.5°N hydrographic section repeats (table S1), were included in Fig. 3, as independent estimates of the basin-wide nutrient transports (black dots in Fig. 3).

To gain further insight into the elements of the circulation controlling the advection of nutrients and the basin-scale biochemical cycles, nutrient transports were split into throughflow or barotropic ($T_N^{through}$), overturning (T_N^{over}) and horizontal (T_N^{horiz}) components (e.g. [69]), such that:

$$T_N^{net} = T_N^{through} + T_N^{over} + T_N^{horiz} = \rho \bar{N} \bar{v} \int L(z)\, dz + \rho \, \langle N \rangle(z) \, \langle v \rangle(z) \, \rho \int \langle N \rangle(z) \, \langle v \rangle(z) \, L(z)\, dz + \rho \int \int N'(x,z) \, v'(x,z) \, L(x,z)\, dz\, dx \quad (10)$$

where $\int L(z)\, dz$ accounts for the area of the section, $\bar{v}$ is the section-averaged velocity that results from the total transport across the section, $\bar{v}$ = T/A, with T the total volume transport across the section; $\langle v \rangle(z)$ is the mean vertical profile of the velocity anomalies, $\langle v \rangle(z) = v(x,z) - \bar{v}$ and $v'(x,z)$ represents the deviations from the mean vertical profile, $v'(x,z) = v(x,z) - \langle v \rangle(z)$. Equivalently, for the nutrient concentration $\bar{N}$ represents the section mean; $\langle N \rangle(z)$ accounts for the mean vertical profile of the nutrient anomalies, $\langle N \rangle(z) = N(x,z) - \bar{N}$; and $N'(x,z)$ are the deviations from the corresponding mean vertical profile, $N'^{(x,z)} = N(x,z) - \langle N \rangle(z)$. The annual mean transports (total transport and split by overturning, horizontal and throughflow components) are summarized in table S10. The same transport decomposition depicted in equation (10) was also applied to the remineralized and preformed nutrients transports. The annual mean preformed and remineralized nutrient transports (total transport and split by overturning, horizontal and throughflow components) are summarized in table S10.

Note that in addition to the above transport decomposition, in this study we also used the notation upper/lower AMOC limb transport to refer to the transport in the upper/lower 1100 dbar[17]. Such upper/lower limb separation corresponds broadly to the surface to σ_{moc} integrated transport, with σ_{moc} as σ_1 = 32.15 kg m^{-3} (potential density referred to 1000 dbar)[15,16,70]. For illustration, fig. S10 shows the (upper-limb) AMOC transport time series computed as surf-to-1100 dbar and as surf-to-σ_{moc}.

Observation-period changes and tendencies

For all nutrient fluxes (total, remineralized and preformed fractions, and throughflow, overturning and horizontal components), we estimated the linear least-square fit of the time series, namely observation-period tendencies (table S5). We also computed the percentage of change at the end of the 8-year period (2012) with regards the total nutrient transport at the beginning of the period (2004), computed as the difference between the final $T_N^{fitted}(2012)$ and initial $T_N^{fitted}(2004)$ nutrient transport given by the fitted tendencies, divided by T_N^{fitted} (2004) and multiplied by 100 (table S10).

Regarding the tendencies in the nutrient concentrations, it is important to note that our 10-day nutrient fields are estimated following an MLR method. Hence, these may actually be influenced by long-term changes in the thermohaline field rather than in the nutrients themselves. Therefore, and in order to validate tendencies as a methodologically-independent feature, we assessed the long-term change in nutrient concentrations separately from the available hydrographic data set (table S1). In-situ nutrient-data based increase-decrease rates were computed by density layers (dividing the main water masses) and regions (table S9).

Total North Atlantic nutrient inventories

North of 26.5°N, the North Atlantic comprises approximately a volume of water of 7.15×10^{16} m^3 (total area of 16.6×10^{12} m^2 and average depth of 4300 m). Given average nutrient concentrations of 17.0, 17.2 and 1.13 µmol kg^{-1} for silicate, nitrate and phosphate, respectively (source data WOA18), the inferred total nutrient inventories are 1.24×10^{12} kmol-Si, 1.26×10^{12} kmol-N, and 8.27×10^{10} kmol-P. Having the total inventories, and the total flux across 26.5°N (-384 kmol-Si s^{-1}, -170 kmol-N s^{-1} and -11.8 kmol-P s^{-1}, 14-year mean values), the residence time for each of the nutrient can be estimated as the quotient of the total inventory divided by the flux across the section, i.e., 103, 237 and 222 years for silicate, nitrate, and phosphate, respectively; or 148, 477 and 546 years for silicate, nitrate, and phosphate, respectively, if we consider that 30%, 51%, and 59% of the total silicate, nitrate, and phosphate transports across the section (which are southwards) are balanced by other additional nutrient inputs. Given that 70% of the silicate flux across the section (49% for nitrate, and 41% for phosphate) cannot be balanced against other inputs, our results point to a change in the total inventories of 5% per decade for silicate, and 1% per decade for nitrate and phosphate. Given that the accuracy limits for measured nutrient concentrations are around 2% for silicate and nitrate, and 4% for phosphate[71], and considering the average North Atlantic nutrient inventory estimated from the (annual climatology-based) nutrient concentrations above, the minimum water-column concentration change required to be robustly detectable (i.e. assuming a required change of at least twice the accuracy limits), would be 0.68 µmol kg^{-1}, 0.69 µmol kg^{-1}, and 0.09 µmol kg^{-1} for silicate, nitrate and phosphate, respectively. Based on the residence times estimated above, when taking into account the additional nutrient sources, we inferred total nutrient inventory changes in the North Atlantic of -1.65 µmol-Si kg^{-1}, -0.41 µmol-N kg^{-1} and -0.029 µmol-P kg^{-1} for the 2004-to-2018 period.

Results from the ECCO-Darwin model (Fig. 4) illustrate the spatial patterns of the nutrient change for the 2004-to-2018 period, and the extension of the estimated minimum change (decrease/increase) required to be robustly observable in the water column (indicated by the blue/red contour line). Estimates obtained from the ECCO-Darwin model for nitrate and phosphate (14-year North Atlantic basin average$\pm$std nutrient change of -0.61 ± 0.22 µmol-N kg^{-1} and -0.038 ± 0.018 µmol-P kg^{-1}) support our results (-0.41 µmol-N kg^{-1} and -0.029 µmol-P kg^{-1}). However, there is a discrepancy in the magnitude of the silicate inventory change, our results pointing to a 8-time larger basin-scale overall decrease (-1.65 μmol-Si kg^{-1}) than that estimated from ECCO-Darwin model data (-0.21 μmol-Si kg^{-1}).

Conceptual Model

Under the premise that the AMOC drives most of the variability and magnitude of the total nutrient transports at 26.5°N, we formulate a simple conceptual model to illustrate how the AMOC decrease might actually be the (potential) first-order mechanism by which the North Atlantic seems to be 'losing' nutrients. We use phosphate as a reference, as it is the only macronutrient not affected by additional biological processes in the ocean other than the production and decomposition of organic matter. As an initial state, we start from a simplistic two AMOC-limb schematics defining an enclosed domain between the 26.5°N-RAPID section and the Arctic Sills (Fig. 5A). We start with a mean AMOC of 20 Sv and an average phosphate concentration for the upper AMOC limb of 1 μmol kg^{-1}, leading to a total phosphate transport of 20 kmol-P s^{-1} (assuming a reference density of 1000 kg m^{-3}, for simplicity). In order to only evaluate the AMOC contribution to the nutrient inventory, we disregarded any additional input of phosphate (atmospheric, rivers, Arctic Sills, etc.) and just accounted for the biological nutrient consumption/regeneration within the enclosed domain. To include this aspect in the conceptual model, a biological term was introduced, initially assumed stationary and with a mean value of 6 kmol-P s^{-1} (equivalent to a remineralized:preformed nutrient fraction for the North Atlantic upper AMOC limb of 30:70, in agreement to [14]). In this initial setup (Fig. 5A, panel 1), we assume the North Atlantic to be in an idealized steady-state in which phosphate is not being either accumulated nor depleted with time. If we then let the AMOC decrease until it halves in magnitude, keeping the same mean phosphate concentration in the upper AMOC limb, then the horizontal phosphate advection decreases (Fig. 5A, panel 2). If we assume the BCP strength remains constant (6 kmol-P s^{-1}), then the nutrient concentration in the upper AMOC limb reaching higher latitudes must be lower (in the assumed case 0.4 μmol kg^{-1}, Fig. 5A, panel 2) than in the initial model setup (0.7 μmol kg^{-1}, Fig. 5A, panel 1). BCP efficiency, however, will have increased from 30% (6/[6+14]*100; Fig. 5A, panel 1) to 46% (6/[6+7]*100; Fig. 5A, panel 2). The AMOC transport reduction is rapidly compensated between both upper and lower AMOC limbs, i.e., there is a rapid dynamic reorganization in response to the volume transport anomaly (AMOC decrease). However, as the flushing time of a tracer exceeds the timescales at which ocean dynamics balances, the tracer anomaly (decrease in nutrient concentration from 0.7 to 0.4 μmol kg^{-1}), takes longer to be transferred between the upper and the lower AMOC limbs. This differential behaviour is ultimately responsible for a net southward nutrient transport from the North Atlantic (-3 kmol-P s^{-1}, Fig. 5A, panel 2). If we then allow for the nutrient anomaly to propagate to the lower AMOC limb (i.e. assume sufficient time has passed for a new equilibrium to be reached, Fig. 5A, panel 3), the preformed nutrient fraction of the newly formed North Atlantic Deep Water would decrease as result of diminishing the nutrients being advected northwards by the upper AMOC limb. Ultimately, under a new scenario in which AMOC is in a reduced state, a new steady-state (reduced nutrient inventory) could be reached.

Under this last scenario, the BCP efficiency will increase to 60% (6/[6+4]*100; Fig. 5A, panel 3).

The conceptual model was tested with and without the contribution of the northward bottom AMOC branch (i.e. the AABW water mass with the highest inorganic nutrient content, Fig. 1A). When including the AABW contribution, we are able to reproduce a more realistic vertical nutrient distribution, though the net response of the nutrient inventory to the variability of the AMOC magnitude stays the same. Hence, for simplicity, we just show the schematics based on the upper-lower AMOC limbs.

In order to provide a more quantitative assessment that supports the hypothesis drawn by the conceptual model, we created a theoretical 2-box model (fig. S5A), by which:

$$V_1 \frac{\partial N_1}{\partial t} = T\,(N_0 - N_1) - R + I \quad (11)$$

$$V_2 \frac{\partial N_2}{\partial t} = T\,(N_1 - N_2) + R \quad (12)$$

where V_1 and V_2 refer to the volume of the upper and lower boxes, respectively; N is the general notation for the nutrient concentration (subindex 0, 1 and 2 referring to boxes 0, 1, and 2, respectively), $\frac{\partial N}{\partial t}$ refers to the time derivative of the nutrient concentration, T refers to the AMOC transport, R to remineralization, and I to the additional nutrient input. Note that V_1/T and V_2/T represent the flushing times (λ_1 and λ_2, respectively) for the upper and lower boxes. For $T=T^0=20$ Sv, and given $V_1= 1.7 \times 10^{16}$ m^3 and $V_2= 5.5 \times 10^{16}$ m^3, then λ_1~27 yr and λ_2~87 yr, respectively. Under the steady-state assumption, $\frac{\partial N_1}{\partial t} = 0$, $\frac{\partial N_2}{\partial t} = 0$, so that equations (11) and (12) become:

$$N_1{}^0 = N_0 + \frac{(I-R)}{T^0} \quad (13)$$

$$N_2{}^0 = N_0 + \frac{I}{T^0} \quad (14)$$

where the super index 0 refers to the initial state (steady-state). If we now apply a perturbation (50% reduction) to the AMOC (T'), then:

$$N_1{}' = N_0 + \frac{(I-R)}{T'} \quad (15)$$

$$N_2{}' = N_0 + \frac{I}{T'} \quad (16)$$

The system of differential equations (11) and (12) were solved by parameterising and integrating it over a time scale of 1000 years. By means of this simple 2-box model, we tested the sensitivity of our results to a given range of changes in the input variables (N_0, R, I), detailed in the 'Sensitivity Analysis' section in Supplementary Methods (and fig. S5).

Acknowledgments: We thank the captains, crew, technicians and scientists who contributed to the acquisition, processing, and quality control of the hydrographic data used in this study. We particularly thank B. Moat for the availability of the RAPID gridded fields used to update the time series to 2018. We also thank the programs that make cruise data available: GO-SHIP (www.go-ship.org), CLIVAR (www.clivar.org) and CCHDO (cchdo.ucsd.edu).

Funding: This work is a contribution to ABC-Fluxes (NERC-funded grant No NE/M005046/1), AtlantOS (EU Horizon 2020 grant No 516 633211), and CLASS (NERC-funded grant No NE/R015953/1) projects. PB, EM and RS were supported by Horizon Europe project OceanICU (Ocean - Improving Carbon Understanding) under grant agreement and 101083922, EM and RS were supported by The Bjerknes Centre for Climate Research programme Dynasor. L.I.C. was supported by the University of Vigo through the Galician I2C Plan, NERC and Ifremer. E.M., R.S. and P.B. were financed by NERC and NORCE; H.M. by CNRS; C.M.M. and D.S. by NERC, S.T. by AWI; M.B. by NOAA; G.R. by the University of Vigo.

Author contributions: L.I.C. conceived and carried out the study, produced the display contents, and wrote the manuscript. E.M., R.S. and C.M.M., contributed to the conceptualization, interpretation of results, and manuscript writing. P.B. provided a source version of the MLR coding over which L.I.C built the inorganic nutrient MLR method. R.S. oversaw the nutrient analyses of the 2004 cruise, S.T.V. the nutrient analyses of the 2010 and 2015 cruises, and E.M. the nutrient analyses of the 2020 cruise. All authors read and contributed to the improvement of the manuscript.

Competing interests: The authors declare no competing interests.

Data and materials availability: The main results presented in this paper (nutrient time series) are available on SEANOE, and the AMOC time series at BODC. Hydrographic data of the A05-24.5N GO-SHIP section are available at the Word Ocean Database (1981), GLODAP (1992, 1998, 2004, 2010, 2011, 2015) and CCHDO (2020); Florida Current absolute transports are available at www.aoml.noaa.gov/phod/floridacurrent, and the Florida Straits repeated hydrography at ftp://ftp.aoml.noaa.gov/phod/pub/WBTS/WaltonSmith/. Further materials that support the findings of this study are available from the corresponding author upon request.

References

1. Parekh, P., Dutkiewicz, S., Follows, M. J. & Ito, T. Atmospheric carbon dioxide in a less dusty world. *Geophysical Research Letters* **33**, (2006).
2. Sanders, R. *et al.* The Biological Carbon Pump in the North Atlantic. *Progress in Oceanography* **129**, 200–218 (2014).
3. Schmidtko, S., Stramma, L. & Visbeck, M. Decline in global oceanic oxygen content during the past five decades. *Nature* **542**, 335–339 (2017).
4. Koeve, W., Kähler, P. & Oschlies, A. Does Export Production Measure Transient Changes of the Biological Carbon Pump's Feedback to the Atmosphere Under Global Warming? *Geophysical Research Letters* **47**, e2020GL089928 (2020).
5. Liu, Y., Moore, J. K., Primeau, F. & Wang, W. L. Reduced CO2 uptake and growing nutrient sequestration from slowing overturning circulation. *Nat. Clim. Chang.* **13**, 83–90 (2023).
6. Frenger, I. *et al.* Misconceptions of the marine biological carbon pump in a changing climate: Thinking outside the "export" box. *Global Change Biology* **30**, e17124 (2024).
7. Letscher, R. T., Primeau, F. & Moore, J. K. Nutrient budgets in the subtropical ocean gyres dominated by lateral transport. *Nature Geosci* **9**, 815–819 (2016).
8. Williams, R. G., Roussenov, V. & Follows, M. J. Nutrient streams and their induction into the mixed layer. *Global Biogeochemical Cycles* **20**, GB1016 (2006).
9. DeVries, T., Primeau, F. & Deutsch, C. The sequestration efficiency of the biological pump. *Geophysical Research Letters* **39**, (2012).

10. Ito, T. & Follows, M. J. Preformed phosphate, soft tissue pump and atmospheric CO2. *Journal of Marine Research* **63**, 813–839 (2005).

11. Moore, C. M. *et al.* Processes and patterns of oceanic nutrient limitation. *Nature Geosci* **6**, 701–710 (2013).

12. DeVries, T. The oceanic anthropogenic CO_2 sink: Storage, air-sea fluxes, and transports over the industrial era. *Global Biogeochem. Cycles* **28**, 631–647 (2014).

13. Williams, R. G. & Follows, M. J. *Ocean Dynamics and the Carbon Cycle: Principles and Mechanisms*. (Cambridge University Press, Cambridge, UK, 2011).

14. Gruber, N. Chapter 1 - The Marine Nitrogen Cycle: Overview and Challenges. in *Nitrogen in the Marine Environment (Second Edition)* (eds. Capone, D. G., Bronk, D. A., Mulholland, M. R. & Carpenter, E. J.) 1–50 (Academic Press, San Diego, 2008). doi:10.1016/B978-0-12-372522-6.00001-3.

15. Carracedo, L. I. *et al.* Counteracting Contributions of the Upper and Lower Meridional Overturning Limbs to the North Atlantic Nutrient Budgets: Enhanced Imbalance in 2010. *Global Biogeochemical Cycles* **35**, e2020GB006898 (2021).

16. Mercier, H. *et al.* Variability of the meridional overturning circulation at the Greenland–Portugal OVIDE section from 1993 to 2010. *Progress in Oceanography* **132**, 250–261 (2015).

17. Smeed, D. *et al.* Atlantic meridional overturning circulation observed by the RAPID-MOCHA-WBTS array at 26N from 2004 to 2018. *British Oceanographic Data Centre* (2019) doi:10/c72s.

18. Schmittner, A. & Galbraith, E. D. Glacial greenhouse-gas fluctuations controlled by ocean circulation changes. *Nature* **456**, 373–376 (2008).

19. Sigman, D. M. & Boyle, E. A. Glacial/interglacial variations in atmospheric carbon dioxide. *Nature* **407**, 859–869 (2000).

20. Bopp, L. *et al.* Multiple stressors of ocean ecosystems in the 21st century: projections with CMIP5 models. *Biogeosciences* **10**, 6225–6245 (2013).

21. Steinacher, M. *et al.* Projected 21st century decrease in marine productivity: a multi-model analysis. *Biogeosciences* **7**, 979–1005 (2010).

22. Schmittner, A. Decline of the marine ecosystem caused by a reduction in the Atlantic overturning circulation. *Nature* **434**, 628 (2005).

23. Gruber, N. Anthropogenic CO2 in the Atlantic Ocean. *Global Biogeochemical Cycles* **12**, 165–191 (1998).

24. Khatiwala, S. *et al.* Global ocean storage of anthropogenic carbon. *Biogeosciences* **10**, 2169–2191 (2013).

25. Bryden, H. L., King, B. A., McCarthy, G. D. & McDonagh, E. L. Impact of a 30% reduction in Atlantic meridional overturning during 2009–2010. *Ocean Sci.* **10**, 683–691 (2014).

26. Marinov, I. *et al.* Impact of oceanic circulation on biological carbon storage in the ocean and atmospheric pCO2. *Global Biogeochemical Cycles* **22**, (2008).

27. Smeed, D. A. *et al.* Observed decline of the Atlantic meridional overturning circulation 2004-2012. *Ocean Science* **10**, 29–38 (2014).

28. Smeed, D. A. *et al.* The North Atlantic Ocean Is in a State of Reduced Overturning. *Geophys. Res. Lett.* **45**, 2017GL076350 (2018).

29. McCarthy, G. D. *et al.* Measuring the Atlantic Meridional Overturning Circulation at 26°N. *Progress in Oceanography* **130**, 91–111 (2015).

30. Cunningham, S. A. *et al.* Temporal Variability of the Atlantic Meridional Overturning Circulation at 26.5 N. *Science* **317**, 935–938 (2007).

31. Moat B. I. *et al.* Major variations in subtropical North Atlantic heat transport at short (5 day) timescales and their causes. *Journal of Geophysical Research: Oceans* **121**, 3237–3249 (2016).

32. Bryden, H. L. *et al.* Reduction in Ocean Heat Transport at 26°N since 2008 Cools the Eastern Subpolar Gyre of the North Atlantic Ocean. *Journal of Climate* **33**, 1677–1689 (2020).

33. McDonagh, E. L. *et al.* Continuous Estimate of Atlantic Oceanic Freshwater Flux at 26.5°N. *Journal of Climate* **28**, 8888–8906 (2015).

34. Brown, P. J. *et al.* Circulation-driven variability of Atlantic anthropogenic carbon transports and uptake. *Nat. Geosci.* 1–7 (2021).

35. Carter, B. R. *et al.* New and updated global empirical seawater property estimation routines. *Limnology and Oceanography: Methods* **19**, 785–809 (2021).

36. Bittig, H. C. *et al.* An Alternative to Static Climatologies: Robust Estimation of Open Ocean CO_2 Variables and Nutrient Concentrations From T, S, and O_2 Data Using Bayesian Neural Networks. *Front. Mar. Sci.* **5**, (2018).

37. Lavín, A. M., Bryden, H. L. & Parrilla, G. Mechanisms of heat, freshwater, oxygen and nutrient transports and budgets at 24.5°N in the subtropical North Atlantic. *Deep Sea Research Part I: Oceanographic Research Papers* **50**, 1099–1128 (2003).

38. Ganachaud, A. & Wunsch, C. Oceanic nutrient and oxygen transports and bounds on export production during the World Ocean Circulation Experiment. *Global Biogeochemical Cycles* **16**, 5-1-5–14 (2002).

39. Pelegrí, J. L. & Csanady, G. T. Nutrient transport and mixing in the Gulf Stream. *J. Geophys. Res.* **96**, 2577–2583 (1991).

40. Fontela, M., Mercier, H. & Pérez, F. F. Long-term integrated biogeochemical budget driven by circulation in the eastern subpolar North Atlantic. *Progress in Oceanography* (2019).

41. Torres-Valdés, S. *et al.* Export of nutrients from the Arctic Ocean. *J. Geophys. Res. Oceans* **118**, 1625–1644 (2013).

42. Alvarez, M., Bryden, H. L., Pérez, F. F., Ríos, A. F. & Rosón, G. Physical and biogeochemical fluxes and net budgets in the subpolar and temperate North Atlantic. *Journal of Marine Research* **60**, 191–226 (2002).

43. Hátún, H. *et al.* The subpolar gyre regulates silicate concentrations in the North Atlantic. *Scientific Reports* **7**, 14576 (2017).

44. Hydes, D. *et al.* Determination of dissolved nutrients (N, P, Si) in seawater with high precision and inter-comparability using gas-segmented continuous flow analysers. (2010).

45. Carroll, D. *et al.* The ECCO-Darwin Data-Assimilative Global Ocean Biogeochemistry Model: Estimates of Seasonal to Multidecadal Surface Ocean pCO_2 and Air-Sea CO_2 Flux. *Journal of Advances in Modeling Earth Systems* **12**, e2019MS001888 (2020).

46. Consortium ECCO. gcmfaces analysis of ECCO V4, Release 4 (1992-2017). https://ecco-group.org/docs/v4r4_overview_plots.pdf (2019).

47. Consortium, E. *et al. Synopsis of the ECCO Central Production Global Ocean and Sea-Ice State Estimate, Version 4 Release 4*. https://zenodo.org/records/4533349 (2021).

48. Behrenfeld, M. J. *et al.* Climate-driven trends in contemporary ocean productivity. *Nature* **444**, 752–755 (2006).

49. Duce, R. A. *et al.* Impacts of Atmospheric Anthropogenic Nitrogen on the Open Ocean. *Science* **320**, 893–897 (2008).

50. Beusen, A. H. W., Bouwman, A. F., Van Beek, L. P. H., Mogollón, J. M. & Middelburg, J. J. Global riverine N and P transport to ocean increased during the 20th century despite increased retention along the aquatic continuum. *Biogeosciences* **13**, 2441–2451 (2016).

51. Jickells, T. D. *et al.* A reevaluation of the magnitude and impacts of anthropogenic atmospheric nitrogen inputs on the ocean. *Global Biogeochem. Cycles* **31**, 2016GB005586 (2017).

52. Hawkings, J. R. *et al.* Ice sheets as a missing source of silica to the polar oceans. *Nature Communications* **8**, 14198 (2017).

53. Bopp, L., Aumont, O., Cadule, P., Alvain, S. & Gehlen, M. Response of diatoms distribution to global warming and potential implications: A global model study. *Geophysical Research Letters* **32**, (2005).

54. Boot, A., von der Heydt, A. S. & Dijkstra, H. A. Effect of Plankton Composition Shifts in the North Atlantic on Atmospheric pCO_2. *Geophysical Research Letters* **50**, e2022GL100230 (2023).

55. Fu, Y., Li, F., Karstensen, J. & Wang, C. A stable Atlantic Meridional Overturning Circulation in a changing North Atlantic Ocean since the 1990s. *Science Advances* **6**, eabc7836 (2020).

56. Knight, J. R., Allan, R. J., Folland, C. K., Vellinga, M. & Mann, M. E. A signature of persistent natural thermohaline circulation cycles in observed climate. *Geophysical Research Letters* **32**, (2005).

57. Moore, G. W. K., Halfar, J., Majeed, H., Adey, W. & Kronz, A. Amplification of the Atlantic Multidecadal Oscillation associated with the onset of the industrial-era warming. *Scientific Reports* **7**, 40861 (2017).

58. Schlesinger, M. E. & Ramankutty, N. An oscillation in the global climate system of period 65–70 years. *Nature* **367**, 723 (1994).

59. Voldoire, A. *et al.* Evaluation of CMIP6 DECK Experiments With CNRM-CM6-1. *Journal of Advances in Modeling Earth Systems* **11**, 2177–2213 (2019).

60. Riebesell, U., Körtzinger, A. & Oschlies, A. Sensitivities of marine carbon fluxes to ocean change. *PNAS* **106**, 20602–20609 (2009).

61. IPCC. *IPCC Special Report on the Ocean and Cryosphere in a Changing Climate [H.- O. Pörtner, D.C. Roberts, V. Masson-Delmotte, P. Zhai, M. Tignor, E. Poloczanska, K. Mintenbeck, M. Nicolai, A. Okem, J. Petzold, B. Rama, N. Weyer (Eds.)].* (2019).

62. Dee, D. P. *et al.* The ERA-Interim reanalysis: configuration and performance of the data assimilation system. *Q.J.R. Meteorol. Soc.* **137**, 553–597 (2011).

63. Baringer, M. O. & Larsen, J. C. Sixteen years of Florida Current Transport at 27° N. *Geophys. Res. Lett.* **28**, 3179–3182 (2001).

64. Lauvset, S. K. *et al.* An updated version of the global interior ocean biogeochemical data product, GLODAPv2.2021. *Earth System Science Data* **13**, 5565–5589 (2021).

65. Garcia, H. E. *et al.* Dissolved Inorganic Nutrients (phosphate, nitrate and nitrate+nitrite, silicate). in *World Ocean Atlas 2018* vol. 4 35 (NOAA Atlas NESDIS 84, 2018).

66. Yool, A., Popova, E. E. & Anderson, T. R. MEDUSA-2.0: an intermediate complexity biogeochemical model of the marine carbon cycle for climate change and ocean acidification studies. *Geoscientific Model Development* **6**, 1767–1811 (2013).

67. Anderson, L. A. & Sarmiento, J. L. Redfield ratios of remineralization determined by nutrient data analysis. *Global Biogeochemical Cycles* **8**, 65–80 (1994).

68. Fraga, F., Ríos, A. F., Pérez, F. F. & Figueiras, F. G. Theoretical limits of oxygen: carbon and oxygen: nitrogen ratios during photosynthesis and mineralisation of organic matter in the sea. *Scientia Marina* **62**, 161–168 (1998).

69. Bryden, H. L., King, B. A. & McCarthy, G. D. South Atlantic overturning circulation at 24°S. *Journal of Marine Research* **69**, 38–56 (2011).

70. Daniault, N. *et al.* The northern North Atlantic Ocean mean circulation in the early 21st century. *Progress in Oceanography* **146**, 142–158 (2016).

71. Olsen, A. *et al.* An updated version of the global interior ocean biogeochemical data product, GLODAPv2.2020. *Earth System Science Data* **12**, 3653–3678 (2020).

72. Szuts, Z. B. & Meinen, C. Salinity Transport in the Florida Straits. *Journal of Atmospheric and Oceanic Technology* **30**, 971–983 (2013).

73. Woodgate, R. A. & Aagaard, K. Revising the Bering Strait freshwater flux into the Arctic Ocean. *Geophysical Research Letters* **32**, (2005).

74. Björk, G. The vertical distribution of nutrients and oxygen 18 in the upper Arctic Ocean. *Journal of Geophysical Research: Oceans* **95**, 16025–16036 (1990).

75. Mahowald, N. *et al.* Global distribution of atmospheric phosphorus sources, concentrations and deposition rates, and anthropogenic impacts. *Global Biogeochem. Cycles* **22**, GB4026 (2008).

76. Tréguer, P. J. *et al.* Reviews and syntheses: The biogeochemical cycle of silicon in the modern ocean. *Biogeosciences* **18**, 1269–1289 (2021).

77. Sharples, J., Middelburg, J. J., Fennel, K. & Jickells, T. D. What proportion of riverine nutrients reaches the open ocean? *Global Biogeochem. Cycles* **31**, 2016GB005483 (2016).

78. Dürr, H. H., Meybeck, M., Hartmann, J., Laruelle, G. G. & Roubeix, V. Global spatial distribution of natural riverine silica inputs to the coastal zone. *Biogeosciences* **8**, 597–620 (2011).

79. Peucker-Ehrenbrink, B. Land2Sea database of river drainage basin sizes, annual water discharges, and suspended sediment fluxes. *Geochemistry, Geophysics, Geosystems* **10**, (2009).

80. Curry, B., Lee, C. M., Petrie, B., Moritz, R. E. & Kwok, R. Multiyear Volume, Liquid Freshwater, and Sea Ice Transports through Davis Strait, 2004–10. *J. Phys. Oceanogr.* **44**, 1244–1266 (2013).

81. Huertas, I. E. *et al.* Atlantic forcing of the Mediterranean oligotrophy. *Global Biogeochemical Cycles* **26**, n/a-n/a (2012).

82. Singh, A., Lomas, M. W. & Bates, N. R. Revisiting N2 fixation in the North Atlantic Ocean: Significance of deviations from the Redfield Ratio, atmospheric deposition and climate variability. *Deep Sea Research Part II: Topical Studies in Oceanography* **93**, 148–158 (2013).

83. Roussenov, V., Williams, R. G., Mahaffey, C. & Wolff, G. A. Does the transport of dissolved organic nutrients affect export production in the Atlantic Ocean? *Global Biogeochemical Cycles* **20**, (2006).

84. Mahaffey, C., Williams, R. G., Wolff, G. A. & Anderson, W. T. Physical supply of nitrogen to phytoplankton in the Atlantic Ocean. *Global Biogeochemical Cycles* **18**, (2004).

85. Torres-Valdés, S. *et al.* Distribution of dissolved organic nutrients and their effect on export production over the Atlantic Ocean. *Global Biogeochemical Cycles* **23**, (2009).

86. Letscher, R. T., Hansell, D. A., Carlson, C. A., Lumpkin, R. & Knapp, A. N. Dissolved organic nitrogen in the global surface ocean: Distribution and fate. *Global Biogeochemical Cycles* **27**, 141–153 (2013).

87. Jackson, L. C., Peterson, K. A., Roberts, C. D. & Wood, R. A. Recent slowing of Atlantic overturning circulation as a recovery from earlier strengthening. *Nature Geosci* **9**, 518–522 (2016).

88. Chomiak, L. N., Yashayaev, I., Volkov, D. L., Schmid, C. & Hooper, J. A. Inferring Advective Timescales and Overturning Pathways of the Deep Western Boundary Current in the North Atlantic Through Labrador Sea Water Advection. *Journal of Geophysical Research: Oceans* **127**, e2022JC018892 (2022).

89. Yashayaev, I. The Labrador Sea sets a new reference point in the subpolar North Atlantic climate record. https://www.researchsquare.com (2023) doi:10.21203/rs.3.rs-2663705/v1.

90. Lozier, M. S. *et al.* A sea change in our view of overturning in the subpolar North Atlantic. *Science* **363**, 516–521 (2019).

91. Chafik, L., Holliday, N. P., Bacon, S. & Rossby, T. Irminger Sea Is the Center of Action for Subpolar AMOC Variability. *Geophysical Research Letters* **49**, e2022GL099133 (2022).

92. Koelling, J., Atamanchuk, D., Karstensen, J., Handmann, P. & Wallace, D. W. R. Oxygen export to the deep ocean following Labrador Sea Water formation. *Biogeosciences* **19**, 437–454 (2022).

93. McCarthy, G. *et al.* Observed interannual variability of the Atlantic meridional overturning circulation at 26.5°N: INTERANNUAL VARIABILITY OF THE MOC. *Geophysical Research Letters* **39**, n/a-n/a (2012).

94. Jackett, D. R. & McDougall, T. J. A Neutral Density Variable for the World's Oceans. *Journal of Physical Oceanography* **27**, 237–263 (1997).

95. Roemmich, D. & Wunsch, C. Two transatlantic sections: Meridional circulation and heat flux in the subtropical North Atlantic Ocean. *Deep Sea Research Part A. Oceanographic Research Papers* **32**, 619–664 (1985).

96. Atkinson, C. P., Bryden, H. L., Cunningham, S. A. & King, B. A. Atlantic transport variability at 25° N in six hydrographic sections. *Ocean Science* **8**, 497–523 (2012).

97. Bryden, H. L. *et al.* Decadal changes in water mass characteristics at 24 N in the subtropical North Atlantic Ocean. *Journal of Climate* **9**, 3162–3186 (1996).

98. Hernández-Guerra, A. *et al.* Meridional overturning transports at 7.5N and 24.5N in the Atlantic Ocean during 1992–93 and 2010–11. *Progress in Oceanography* **128**, 98–114 (2014).

99. Wanninkhof, R. *et al.* Ocean acidification along the Gulf Coast and East Coast of the USA. *Continental Shelf Research* **98**, 54–71 (2015).

100. Hooper, J. A. & Baringer, M. O. *Hydrographic Measurements Collected Aboard the UNOLS Ship R/V Walton Smith, 2015 : Western Boundary Time Series Cruise Florida Current : Cruise IDs - WS1501, FC1504, FC1505, FC1507, FC1509, FC1511*. (Atlantic Oceanographic and Meteorological Laboratory, 2016).

101. Hooper, J. A. & Baringer, M. O. *Hydrographic Measurements Collected Aboard the UNOLS Ship R/V Walton Smith, 2016: Western Boundary Time Series Cruise—Florida Current (NOAA Data Report, OAR-AOML-77)*. (Oceanic and Atmospheric Research Laboratories (U.S.);Atlantic Oceanographic and Meteorological Laboratory, 2020).

102. Tréguer, P. *et al.* The silica balance in the world ocean: a reestimate. *Science* **268**, 375–379 (1995).

103. Tréguer, P. J. & Rocha, C. L. D. L. The World Ocean Silica Cycle. *Annual Review of Marine Science* **5**, 477–501 (2013).

104. Mayorga, E. *et al.* Global Nutrient Export from WaterSheds 2 (NEWS 2): Model development and implementation. *Environmental Modelling & Software* **25**, 837–853 (2010).

Supplementary Information for

Direct observation of North Atlantic nutrient transport and biological pump variability linked to the Meridional Overturning Circulation

Lidia I. Carracedo* *et al.*

*Corresponding author. Email: lidia.carracedo@ifremer.fr

This PDF file includes:

Supplementary Methods
Supplementary Notes
Figs. S1 to S11
Tables S1 to S10
References (72 to 104) (Included at the end of the reference section of the main text)

Supplementary Methods

S1. Nutrient transport uncertainties

Nutrient transport uncertainties were estimated based on error propagation as for freshwater flux time series calculations at 26.5°N[33]. We calculated the uncertainty of each of each 10-day estimate of nutrient flux (*σNT*) by combining the transport-derived uncertainty (σNT_T) and the nutrient-derived uncertainty (σNT_N) in quadrature, such that

$$\sigma NT = \sqrt{\sigma NT_T^2 + \sigma NT_N^2} = \sqrt{[\sigma T_{reg} \times (\langle N \rangle_{reg} - \langle N \rangle_{sec})]^2 + \left[\sigma NT_{Nreg}\right]^2} \qquad (7)$$

where the subindex 'reg' refers to the subregions/components into which the overall volume transport across the 26.5°N-RAPID section is originally made up from [33]: the Florida Straits submarine-cable-based transport estimate, the Ekman wind-driven flux, the Western boundary mooring-based flux, the upper interior (<1760 dbar) Argo-data-based transport and the deep interior (>1760 dbar) hydrographic-based transport (details given below). For illustration, fig. S11 shows the nutrient transport split into these subregions. In equation (7), σNT_T was estimated as the product of the transport uncertainty (σT_{reg}) and the nutrient anomaly ($\langle N \rangle_{reg}$-$\langle N \rangle_{sec}$) per region. The uncertainty associated with the MLR-based nutrient concentrations (σNT_N) was estimated by means of a Monte Carlo method in which we randomly perturbed the time-varying nutrient fields. Each value of the space grid, and for each time-step, was perturbed by following a normal distribution, with the mean being the MLR-derived nutrient value and the standard deviation being the standard error of the MLR adjustment for each MLR-region (root mean squared error of the MLR analysis). Note that the Florida Straits subregion was treated separately from the MLR methodology, hence the vertical nutrient profile was perturbed by following a normal distribution with the mean being the nutrient value (according to eq. 4, in Materials and Methods) and the standard deviation of the Florida Straits nutrient data (2004, 2010, 2012 and 2015 cruise data) at each vertical level. 100 perturbations were run at every time step, and the nutrient transport (according to eq. 8, in Materials and Methods) by regions was recomputed. The final uncertainty σNT_N was estimated as the standard deviation of the newly computed 100 mean nutrient transports by regions.

i) *Florida Straits:* The Florida Straits daily transport measurements have a calibration uncertainty of 1.4 Sv[72]. Following [33], the uncertainty in the 10-day average is of 0.99 Sv, assuming 2 degrees of freedom in the average. In combination with the nutrient concentration anomaly obtained as difference between the Florida Straits transport-weighted nutrient (7.9, 14.3 and 0.9 μmol kg^{-1} for silicate, nitrate and phosphate, respectively) and the section-average nutrient (23.6, 18.7 and 1.2 μmol kg^{-1} for silicate, nitrate and phosphate, respectively), we obtain the Florida Current transport-derived uncertainty (16, 4 and 0.2 kmol s^{-1} for silicate, nitrate and phosphate, respectively). The nutrient-derived uncertainties, estimated by means of the Monte Carlo method, are of 7.7, 11.6 and 0.9 kmol s^{-1} for silicate, nitrate and phosphate, respectively. The transport-derived and nutrient-derived uncertainties are combined in quadrature to give a total Florida Straits uncertainty of 18.0, 12.3 and 1.0 kmol s^{-1} for silicate, nitrate and phosphate, respectively.

ii) *Ekman transport:* The average Ekman transport is 3.5 Sv northward, with an uncertainty of 10%[33] (i.e. 0.35 Sv). The average Ekman nutrients 0.6, 0.04, 0.01 µmol kg^{-1} for silicate, nitrate and phosphate, respectively, giving a nutrient anomaly of 23.2, 18.5, 1.2 µmol kg^{-1} for silicate, nitrate and phosphate, respectively. This gives a transport-derived uncertainty of 8.7, 6.8 and 0.4 kmol s^{-1} for silicate, nitrate and phosphate, respectively. As for the MRL nutrient-derived uncertainty, the Monte Carlo method provides uncertainties of 2.3, 1.3 and 0.2 kmol s^{-1} for silicate, nitrate and phosphate, respectively. The combination of these elements contributes to total uncertainty for the Ekman component of 9.0, 6.9 and 0.5 kmol s^{-1} for silicate, nitrate and phosphate, respectively.

iii) *Western Boundary Wedge:* Following [33], we assumed that the uncertainty in this region is concentrated in the more variable upper ocean above 1000 m, with the uncertainty being a 10% of the mean transport, i.e., 0.2 Sv. The nutrients in this region have an average value of 6.2, 10.8, 0.7 µmol kg^{-1}, and an anomaly relative to the interior of 17.6, 7.7, 0.6 µmol kg^{-1} for silicate, nitrate and phosphate, respectively. The MRL nutrient-related uncertainty for this region is negligible, hence the total WBW uncertainty is that due to the transport uncertainty.

iv) *Upper interior:* Following [33], for the upper interior transport we used an uncertainty of 0.9 Sv, based on the comprehensive uncertainty analysis at 26.5°N-RAPID section[29]. The mean nutrients in this subregion are 10.4, 0.03, 0.01 µmol kg^{-1}, and the anomaly 13.4, 2.9, and 0.2 µmol kg^{-1} for silicate, nitrate and phosphate, respectively; giving a transport-derived uncertainty of 13.1, 2.9 and 0.2 kmol s^{-1}. The MRL nutrient-related uncertainty for this region is very low, of 0.05, 0.06 and 0.003 kmol s^{-1}. Both estimates combine to give a total uncertainty for this region of 13.1, 2.9 and 0.2 kmol s^{-1} for silicate, nitrate and phosphate, respectively.

v) *Deep Interior:* Same as for the upper interior, we followed [33] and used an uncertainty of 2.0 Sv, based on the comprehensive uncertainty analysis at 26.5°N-RAPID section[29]. The average nutrient concentrations are 31.5, 20.2, and 1.4 µmol kg^{-1} for silicate, nitrate and phosphate, respectively, which are higher compared with the section average, giving a transport-derived uncertainty of 15.3, 3.5 and 0.3 kmol s^{-1}. Same as for the Western boundary Wedge, the MRL nutrient-related uncertainties are negligible (0.005, 0.003 and 0.0002 kmol s^{-1}). Therefore, the total uncertainty for this region is dominated by the transport uncertainty, i.e., 15.3, 3.5 and 0.3 kmol s^{-1} for silicate, nitrate and phosphate, respectively.

vi) *Barotropic Compensation:* In satisfying the net salinity flux constraint, a uniform velocity at the section-average salinity is applied[33]. Following [33], under the assumption that the offset occurs at the section average property, the uncertainty of the barotropic compensation has only one component due to nutrient uncertainty. The representative transport of the compensation is 3 Sv (the typical size of the compensation added as part of the RAPID calculations[29] plus the freshwater flux calculated in [33]), which combined with the standard deviation of the column average nutrients (1.9, 0.5, and 0.03 µmol kg^{-1} for silicate, nitrate and phosphate, respectively), lead to a nutrient-related uncertainty of 6.0, 1.4 and 0.09 kmol s^{-1} for silicate, nitrate and phosphate, respectively.

vii) *Bering Strait constraint:* The mean volume flux at the Bering strait is 0.8 Sv[73], with a volume uncertainty assigned of 0.2 Sv[33]. With mean nutrient concentrations of 23.0, 7.1, and 1.4 µmol kg^{-1} for silicate, nitrate and phosphate, respectively[74], the corresponding transport-derived uncertainty obtained is of 0.3, 2.4 and 0.04 kmol s^{-1} for silicate, nitrate and phosphate, respectively. As for the nutrient-related uncertainty, it is estimated as the product of the mean volume transport (0.8 Sv) and the standard error of the mean concentrations (3.3, 2.2, and 0.2 µmol kg^{-1} for silicate, nitrate and phosphate, respectively; [74]). Both estimates combine to give a total uncertainty for this component of 2.7, 3.0 and 0.2 kmol s^{-1} for silicate, nitrate and phosphate, respectively.

viii) *Total Uncertainty:* Combining the component estimates of the uncertainty in quadrature gives a total uncertainty in each individual 10-day estimate of the nutrient flux of ±29 kmol-Si s^{-1}, ±15 kmol-N s^{-1} and ±1.2 kmol-P s^{-1}, and ±7 kmol-Si s^{-1}, ±4 kmol-N s^{-1} and ±0.4 kmol-P s^{-1} for the full time-series mean. Assuming that there are 12 independent estimates in the year, gives an uncertainty on the annual mean of ±9 kmol-Si s^{-1}, ±4 kmol-N s^{-1} and ±0.3 kmol-P s^{-1} for annual means. The uncertainty due to the volume transport (σNT_T) dominates the total uncertainty estimate for silicate (>70%), whereas for nitrate and phosphate the uncertainty related to the nutrient concentration (σNT_N) contributes approximately up to 40-45% of the total uncertainty).

Uncertainty components for the regions mentioned above are summarized in table S2. Similarly, for the nutrient transports being re-estimated by using neural-network nutrients fields instead of the MLR-nutrients fields, the uncertainty associated with the neural-network-based nutrient concentrations (σNT_N) was also estimated by means a Monte Carlo method, by which we randomly perturbed the time-varying nutrient fields (each value of the space grid and for each time-step) according to a normal distribution with the mean being the neural-network-derived nutrient value and the standard deviation being the neural-network output uncertainty[35,36]. 100 perturbations were run at every time step and the nutrient transport (according to eq. 8, in Materials and Methods) by regions was recomputed. σNT_N was estimated as the standard deviation of the 100 mean nutrient transports by regions (not shown).

S2. Sensitivity analysis

S2.1. MLR sensitivity tests

The limitations inherent to the MLR method are assessed in this section by means of a number of sensitivity analyses performed on the actual data and method, as well as in model data.

MLR sensitivity to the amount of input data. One constraint inherent to the MLR is the number of observations we use as input to feed the fitting model (i.e. training observation dataset). Either the amount of cruise repeats, the time span between the cruises, or the time of the year in which they were carried out are factors that may constrain the MLR performance. First, in order to assess the impact on the final nutrient transport estimates of the amount of input data used to obtain the MLR, we run two sets of tests by recomputing the nutrient transport time series after *i)* running the MLR with every single available cruise individually as the only input data; and *ii)* running the MLR by sequentially adding one cruise at the time. The discrepancies in the magnitude of the mean nutrient transports from the first set of tests ranged within the uncertainty of the estimate (no shown), and did not exceed by more than 20% of the mean transports by the original solution in which all cruise data available were used as input to the MLR. An exception to that was observed when using the 1992 cruise data to model phosphate and the 2011 cruise data to model nitrate, which might be related to data quality on these nutrients for these particular cruises (see GLODAPv2 comments, https://glodapv2.geomar.de/adjustments/). Regarding the second set of tests, that is, running the MLR by sequentially adding one cruise each time, we found that the results converged towards the original set up (all available cruises used as input to obtain the MLR) after three or more cruises were used (not shown).

Secondly, we assessed the impact of the punctual nature of the observation dataset (e.g., seasonal bias due to the time of the year at which each particular cruise was carried out, etc.) by means of the NEMOv3.2-MEDUSA-2.0 ocean model output[66]. From the 1°×1° (velocity and nitrate) model monthly fields, we subtracted a RAPID-like section (at 26.5° N) spanning between 1980 and 2100. The 'model-truth' nitrate was then combined with the NEMO velocity fields to compute the nitrate transport across the RAPID-like section. Since the magnitude of the total nitrate transport by the NEMO-MEDUSA model differs markedly from observation-based studies (including this study, fig. S7), our goal was to use this 'model truth' as a tool for the MLR method validation, rather than using the model output for comparison of absolute transports for the period of study. As part of this MLR assessment, we applied a MLR-like method equivalent to that we applied to our *in situ* data. That is, we subsampled the 'model-truth' temperature, salinity, nitrate, pressure and oxygen fields to the same time-occurrences as those of the in-situ MLR (table S1). With those, we obtained the MLR algorithms (MLR_{nm}) (equivalently as explained in Methods), with which we computed a MLR_{nm}-predicted nitrate (from predictive variables), and, ultimately, recomputed the nitrate transports at each (monthly) time-step with this new MLR_{nm}-nitrate. We only took nitrate as a reference nutrient because silicate presented larger discrepancies (biases) at depth compared to observations (not shown). The conclusion we got from this second test is that applying a cruise-like training dataset to get MLR predictive equations at this latitude has a quite limited impact on the final total nutrient transport estimate (<5% difference in the magnitude of the total mean transport for the 2004-2018 period) (fig. S7), and thus the MLR method seems a valid approach at this particular location and with the available training dataset.

MLR sensitivity to MLR box definition. The use of different subregions (predefined MLR-boxes) to perform independent MLRs is based on the fact that the relative importance of the parameters used to model the nutrient variability varies for each MLR region. Even though the MLR-box definition is a relatively arbitrary choice, varying the MLR-box spatial limits did not have an impact on the total transport of nutrients across the section larger than 5% of the total magnitude (not shown).

MLR sensitivity to oxygen as a predictive variable. Other potential limitations inherent to our MLR procedure relate to the oxygen data being used to recompute the 10-day resolution nutrient fields when applying the MLR equations. Oxygen data come from the WOA18 oxygen fields, which represent seasonal climatological means and, therefore, lack of any temporal trend. In order to assess the impact of this limitation on our final results, we ran two different tests: *a)* by using the original WOA18 seasonal oxygen data as downloaded from the WOA18 website (test 1, table S3), *b)* by using the WOA18 oxygen data to which we added temporal tendencies as estimated by means of the hydrographic data (table S10), namely WOA18 oxygen-adjusted (*main,* in table S3; corresponding to results presented in the main text). Climatological (trendless) oxygen WOA18 data (test 1) produce a significant difference in the total transport of remineralized nutrients (and its trend), mainly linked to the horizontal component. The time-period mean remineralized nutrient transport in test 1 is positive (northwards) compared to a non-statistically different from zero mean when using of the WOA18 oxygen-adjusted (*main*). The interpretation of such discrepancies is that omitting oxygen changes might overestimate the gyre-driven remineralized nutrient transports (and its positive tendency).

Next, we tested the impact on the results of not using oxygen as input variable for prediction, but using temperature and salinity as only predictors. Firstly, we tested it via ESPER_LIR_TS (test 2, table S3). Using ESPER_LIR_TS nutrients produced an enhancement of 38% in the southward total nutrient transport, partly due to a resulting mean southward transport of the remineralized nutrient fraction, and a significant reduction in all the tendencies. Secondly, we assessed the performance of the MLR method in case no oxygen was used at all as input predictive variable. We performed this assessment on the NEMO-MEDUSA dataset, relying on the 'model truth' nitrate transport time series for the 2004-2018 period as a reference. MLR-predicted nitrate fields (estimated using MLR-like methodology applied to model truth nitrate, temperature, pressure and salinity outputs as for observations) were combined with the same velocity fields, enabling direct comparison with model truth nitrate transports. By doing so, the percentage of variance explained by the predictive variables (i.e. potential temperature, salinity, pressure, longitude and time) decreased, mostly in the upper 2500 dbar (from 95% to 89% on average), with some regions (e.g. region 9) being more affected than others (not shown). Hence, and despite the limitations of the input oxygen dataset, we decided to keep oxygen (oxygen-adjusted) as input variable in this study.

Sensitivity of remineralized-preformed decomposition to varying stoichiometric ratios. The remineralized-preformed decomposition of the MLR-nutrient estimate assumes that there are no time varying changes in elemental stoichiometries during 2004–2018. We conducted a sensitivity test to assess the impact of this assumption on the final results, by modifying the stoichiometric ratios between the main components of organic matter, the nitrogen:carbon ratio ($r_{N:C}$) and the phosphorus:carbon ($r_{P:C}$). The ranges of variation for the ratios used for this test are within the observed ranges of marine organic matter composition ($r_{N:C}$= 8:117 to 24:117, $r_{P:C}$= 0.5:117 to 1.5:117)[40,68]. As might be expected, the transports of the preformed and remineralized nutrients are sensitive to the changing ratios (test 3, lower-bound stoichiometric ratios: $r_{N:C}$= 8:117, $r_{P:C}$= 0.5:117; and test 4, upper-bound stoichiometric ratios: $r_{N:C}$= 24:117, $r_{P:C}$= 1.5:117; table S3). Varying the stoichiometric ratios between these lower and upper theoretical limits resulted, respectively, in significantly larger (55% larger than *main* results) and smaller (48% smaller than *main* results) overturning remineralized nutrients being transported to the south; and about 64% larger (lower-bound stoichiometric ratios) and 44% smaller (upper-bound stoichiometric ratios) horizontal remineralized nutrients being advected to the north. Tendencies in the horizontal component are also sensitive changing ratios, with positive tendencies in the horizontal remineralized (preformed) nutrient transport being larger (lower) than *main* in the lower-bound test, and lower (larger) than *main* in the upper-bound test.

MLR low-performance regions. One of the main objectives of using MLR-independent nutrient fields was to evaluate the impact of the MLR performance in those MLR-box regions with the lowest R^2 (R^2<0.4). In order to do so, we recomputed the nutrient transport for those same regions with the ESPER_NN-derived time varying nutrient fields (table S4). For the total silicate transport time series, the impact of those MLR-regions with the lowest MLR performance is virtually negligible, as the difference between the nutrient transport estimate by means of MLR vs non-MLR derived nutrient fields accounts for <1% of the total transport (representing less than 12% of the magnitude of the uncertainty).

S2.2. Conceptual model sensitivity tests.

We used a simple theoretical 2-box model, presented in Materials and Methods (eqs. 11 to 16), to test how the conceptual model interpretation (Fig. 5A) might change depending on the considered parameters, such as: *i)* in the initial nutrient concentration in the upper AMOC limb (N^0), *ii)* the remineralization rate (R), or *iii)* the additional nutrient input (I). Departing from the same schematics as shown in Fig. 5A (and fig. S5A), we tested the simplest configuration, namely *control*, with $N^0_{control}$ = 1.0 µmol kg^{-1}, $R_{control}$ = 4 kmol s^{-1}, $I_{control}$ = 0 kmol s^{-1}, with T^0 = 20 Sv, T' = 10 Sv (fig. S5A). We also ran, as a reference, a test with an observation-like setup, namely *obs*, such as N^0_{obs}= 0.88 µmol kg^{-1}, R_{obs} = 8.7 - 0.06*t kmol s^{-1} (with t being time), I_{obs} = 7 kmol s^{-1}, and T^0_{obs} = 18.8 Sv, T'_{obs} = 16.1 Sv.

i) *Sensitivity to N^0:* Higher N^0 ($N^0_{control}$ = 1.0 µmol kg^{-1}, N^0_a = 1.5 µmol kg^{-1}, N^0_b = 2.0 µmol kg^{-1}) results in larger southward net nutrient transport (fig. S5B, *i*) and higher nutrient concentration in the lower AMOC (fig. S5B, *ii*). Regardless of the value of N^0, the system goes back to equilibrium, however the time it takes to reach it, between 500 to 750 years, increases with increasing N^0 (fig. S5B, *i*). Interestingly, under the observation-like setup, the equilibrium does not go back to zero, but to a net southward nutrient transport (reached around year 460), accompanied by a lower AMOC with a higher nutrient concentration than before perturbation (N^2_{obs}; fig. S5, *ii*).

ii) *Sensitivity to R:* Varying the remineralization rate to a value 50% lower and larger than the control ($R_{control}$ = 4 kmol s^{-1}, R_a = 2 kmol s^{-1}, R_b = 6 kmol s^{-1}), generates a transient which again goes back to a net zero nutrient transport, regardless of the magnitude of R (fig. S5B, *iii*). The magnitude of the net southward transport during the transient is proportional to R (with approximately 50% increase in the total southward transport per 1 kmol s^{-1}-increase in R), with the nutrient concentration in the lower AMOC limb also being larger for larger R (about 1% increment every 1 kmol s^{-1}-increment in R). However, based on our data analysis (Fig. 5B), R is not constant but is likely decreasing over time (R_{obs} = 8.7 - 0.06*t kmol s^{-1}). We tested this scenario by applying the same rate of R decrease to the control case (i.e. R_c = $R_{control}$ - 0.06*t kmol s^{-1}). By doing so, the lower limb decreased substantially its nutrient concentration (N^2_c, fig. S5B, *iv*), and the system did not return to a net zero nutrient transport, but resulted instead in a net northward nutrient transport (fig. S5B, *iii*).

iii) *Sensitivity to I:* Finally, by adding to the additional nutrient input, I_a = 2 kmol s^{-1} and I_b = 4 kmol s^{-1}, the system did not return to a net zero nutrient transport, as in the control ($I_{control}$ = 0 kmol s^{-1}). Instead, it leads to a net southward nutrient transport that balances the magnitude of I, so that the larger the nutrient input, the larger the net southward nutrient transport (fig. S5B, *v*) and the higher the nutrient concentration in the lower AMOC limb when the system reaches the equilibrium (fig. S5B, *vi*).

Summarizing, according to our simple conceptual model, the steady-state (net zero meridional transport of nutrients) can be reached regardless of the initial nutrient concentration considered in the upper AMOC limb, or the magnitude of remineralization (as far as it remains invariant in time). If the additional nutrients sources are included while keeping remineralization constant, or if remineralization varies as function of time but additional nutrient inputs are not considered, then this simple conceptualization fails neither to reach the steady-state nor reproduce observations. When considering both these potential drivers (as in the observation-like test), then the model gets closer to the observation values at the time of the perturbation (50% AMOC slowdown), with a new transient state being reached by which nutrients converge in the North Atlantic basin (i.e. net nutrient transport southwards < I).

<u>S3. Nutrient sources</u>

We used supplementary data sources from former studies (table S6) to account for the additional inputs of nutrients by atmospheric deposition, river runoff, N2-fixation, seafloor weathering, ground water, hydrothermal and meltwater sources, or the nutrient transports across the open boundaries of the domain (Arctic Sills and Gibraltar Strait). The uncertainties on these additional nutrient supplies are of different nature depending on how the estimate was made, or origin of the original values. The total uncertainty of the additional nutrient sources term was estimated by combining the different uncertainty estimates of the all-additional nutrient sources in quadrature.

i) *Atmospheric deposition:* We considered a mean atmospheric deposition of inorganic oxidized nitrogen (nitrate and nitric acid) in the North Atlantic of 0.12 g-N m^{-2} y^{-1} [51], and a total area of 16.6 $x10^{12}$ m^2 between RAPID and the subpolar region, obtaining a total atmospheric nitrate input of 4.5 kmol s^{-1}. To this estimate, we added the value by [40] for the subpolar region (delimited to the north by the Arctic sills), obtaining a final value of 5.9 kmol s^{-1}. For phosphate, we used the model-based deposition rates by [75] (27.9 Gg-P y^{-1}, i.e., 0.03 kmol s^{-1}). Finally, for silicate, we took into account the global value by [76] of 0.5 ± 0.5 Tmol Si y^{-1} (i.e., 16 ± 16 kmol s^{-1}). From this global estimate, we inferred a proportional rate for the North Atlantic of 0.7 ± 0.7 kmol s^{-1}. Note that given the coarse assumption that silicate deposition rates are homogeneous over the world ocean, we assigned a 100% uncertainty to this estimate. In order to keep consistency for the three nutrients, the same criteria were used for nitrate and phosphate.

ii) *Fluvial inputs:* To obtain the nitrate and phosphate fluvial contribution, we considered 617 river sources to the North Atlantic between RAPID and the subpolar region. Based on [51,77], we calculated nitrate and phosphate river inputs to the open ocean of 2.2 ± 0.5 kmol s^{-1} and 0.13 ± 0.06 kmol s^{-1}, respectively. To these values, we added the estimates by [40] for the subpolar region, obtaining final values of 3.5 and 0.22 kmol s^{-1}, respectively. For silicate, we took into account the net silicate input of rivers to the global ocean by [76] (8.1 ± 2.0 Tmol y^{-1}, i.e., 257 ± 63 kmol s^{-1}), and considering a global river discharge into the world oceans of 39 $x10^{12}$ m^3 y^{-1} [78,79], we estimated the proportional amount for the North Atlantic between RAPID and the subpolar region of 29 ± 7 kmol s^{-1} (river volume discharge of around 4.4 x 10^{12} m^3 y^{-1} [79]), and we added the corresponding estimate for the for the subpolar region by [40], obtaining a final value of 33.7 kmol s^{-1}. Additionally, we considered the input of silicate from the Greenland ice-sheet melting (0.2 Tmol y^{-1} [52], i.e., 6.3 ± 6.3 kmol s^{-1}), which summed up to the river runoff, comprises a total silicate source of 40 ± 9 kmol s^{-1}. In this case, the uncertainties represent twice the difference between the upper and lower bound mean estimates.

iii) *Arctic sills:* For the Davis Strait, we estimated the net nutrient transports by using the volume transport estimates by [80] and the property fields by [41]. We estimated the nutrient transport by three vertical levels (upper, intermediate and deep[41]) as the product of the transport-weighted nutrient concentrations at each level multiplied by the transports by [80] obtaining net silicate, nitrate and phosphate transports of 33 ± 7, 23 ± 6, and 2.7 ± 0. 6 kmol s^{-1}, respectively. To these values, we added the nutrient transport estimates across the Fram Strait and the Barents Sea Opening (BSO) by [40], obtaining net silicate, nitrate and phosphate transports across the Arctic Sills of 64 ± 8, 21 ± 7 and 3.6 ± 0.7 kmol s^{-1}, respectively. The uncertainties were estimated as the root sum square of the uncertainties provided by [41] and [40].

iv) Gibraltar Strait: We used the three-year averages by [81] (3.9 ± 0.3, 4.4 ± 0.1, 0.15 ± 0.01 kmol s^{-1} towards the Atlantic). The uncertainty is also provided by [81].

v) Nitrogen fixation: We made use of two different N_2-fixation rate values: one based the PlankTOM model (0.05 mol-N m^{-2} y^{-1} [51]), from which we inferred a nitrate source of 26.3 kmol s^{-1}; and, the second one, based on the in situ N_2-fixation rate estimates by [82] (12.2 ± 0.9 10^{11} mol-N y^{-1}), from which we inferred a nitrogen source of 39 ± 3 kmol s^{-1}. The average of both being 33 kmol s^{-1}. To this value, we added the estimate by [40] for the subpolar region, obtaining a final estimate of the nitrate source via N_2-fixation for the whole North Atlantic of 38 ± 8 kmol s^{-1}. The uncertainty of the estimate by [82] was about 10% of the value. Based on that here we assumed the uncertainty to be twice that percentage, that is, a 20% of the final estimate.

vi) Additional sources of silicate: Submarine groundwater, seafloor weathering, and deep-sea hydrothermal sources constitute additional silicate inputs. To account for their contribution, we relied on the global estimates by [76], from which we calculated input rates proportional to the extension of the North Atlantic, altogether accounting for a net silicate input of 8.7 ± 2.2 kmol s^{-1}. The uncertainty comes from the square sum of the uncertainty of every term, originally from [76].

vii) Dissolved organic nitrogen and phosphorus: High concentrations of dissolved organic nitrogen (DON) and phosphorus (DOP) generally occur in the upper ocean over the tropics[83]. From there, DON and DOP are transported northwards as result of the Ekman wind-driven and overturning circulation[83]. Of the total DON, less than 10% contributes to the nitrogen supply for export production[83,84]; whereas about 95% of the DOP is semilabile[83,85], therefore of relevance to close the phosphate budget in the North Atlantic[84,86]. In order to assess the contribution of the organic fraction across the 26.5°N section, we evaluated the Florida Straits and the Atlantic basin separately. For the Florida Straits, we used data from *in situ* total dissolved nitrogen, total dissolved phosphorus, nitrate and phosphate, from which DON and DOP were computed as the difference between the total minus the inorganic fraction, and the velocities from seven cruises carried out across between 2015 and 2016 (ftp.aoml.noaa.gov/phod/pub/WBTS/WaltonSmith/). As an average of the 7 cruises (± 2 × standard error), we obtained total DON and DOP transports of 134 ± 60 kmol s^{-1} and 3.5 ± 0.6 kmol s^{-1}, respectively. As for the DON and DOP transport of across the Atlantic basin, we relied on the *in situ* DOP estimates obtained during the 2015-DY040 cruise (table S1), from which we calculated a DOP transport of -0.2 kmol s^{-1} (upper 200 dbar, southwards). By assuming a standard $r_{N:P}$ 16:1 stoichiometric ratio, we inferred a DON transport across the basin of about -3.7 kmol s^{-1}. Summed up to the total DON (DOP) transports across the Florida Straits, and assuming that 10% (95%) of this DON (DOP) transport is available for the phytoplankton demand, led to a total contribution to the nitrate (phosphate) budgets of about 13 ± 6 (3 ± 1) kmol-s^{-1}. We used as uncertainty twice the standard error of the mean of the 7 cruise-based estimates of the total DON and DOP transports across the Florida Straits.

Supplementary Notes

Impact of interannual variability

Nutrient fluxes change from year to year (table S10). However, for most of the observation period, the amplitude of the interannual signal did not exceed the standard error of the annual mean -calculated by assuming one independent measurement for each two integral timescales[33], that is, 6 independent measurements per year-, but for the years 2005 and 2006 (2009 and 2012), which showed a notably larger (lower) annual average compared to the period mean for the three nutrients. These interannual anomalies were largely driven by an increase (reduction) of the southward nutrient transport by the NADW (broadly 2500-5000 dbar), west of the MidAtlantic Ridge (not shown). Considering the ~10-yr timescale advective pathway for the NADW from the Labrador Sea to the subtropical North Atlantic at 26.5°N[87,88], these anomalies agree well with reported changes of LSW production (deep convection) in the Labrador Sea[88,89]. Our results indicate that the inter annual variability of the nutrient transport at 26.5°N is strongly linked to the Deep Western Boundary Current and, at its origin, to the intensity of winter convection in the Labrador Sea. At a time where the Irminger Sea has been identified as the centre of action for AMOC variability[90,91], it is important to point out that for the transport of tracers, such as for inorganic nutrients (this study) or oxygen (e.g. [92]), deep convection in the Labrador Sea appears to largely influence the variability of the biogeochemical imprint by the lower AMOC, at least at interannual timescales.

Based on our results, we have also shown that the 30% drop of the AMOC occurred in 2009/2010[25,93] was accompanied by a 4-month South-to-North reversal on the net nutrient fluxes (this study, time series Fig. 3A to C). As a result, the nutrient divergence in the North Atlantic basin (as observed for the 2004-2018 period) was transitorily in balance with the additional sources. That is, the interannual signal can notably overlay (amplifying or dampening) the transient state and, hence, the length of time series (and so its continuity in time) is crucial to confidently resolve and interpret tendencies of the system at longer time scales.

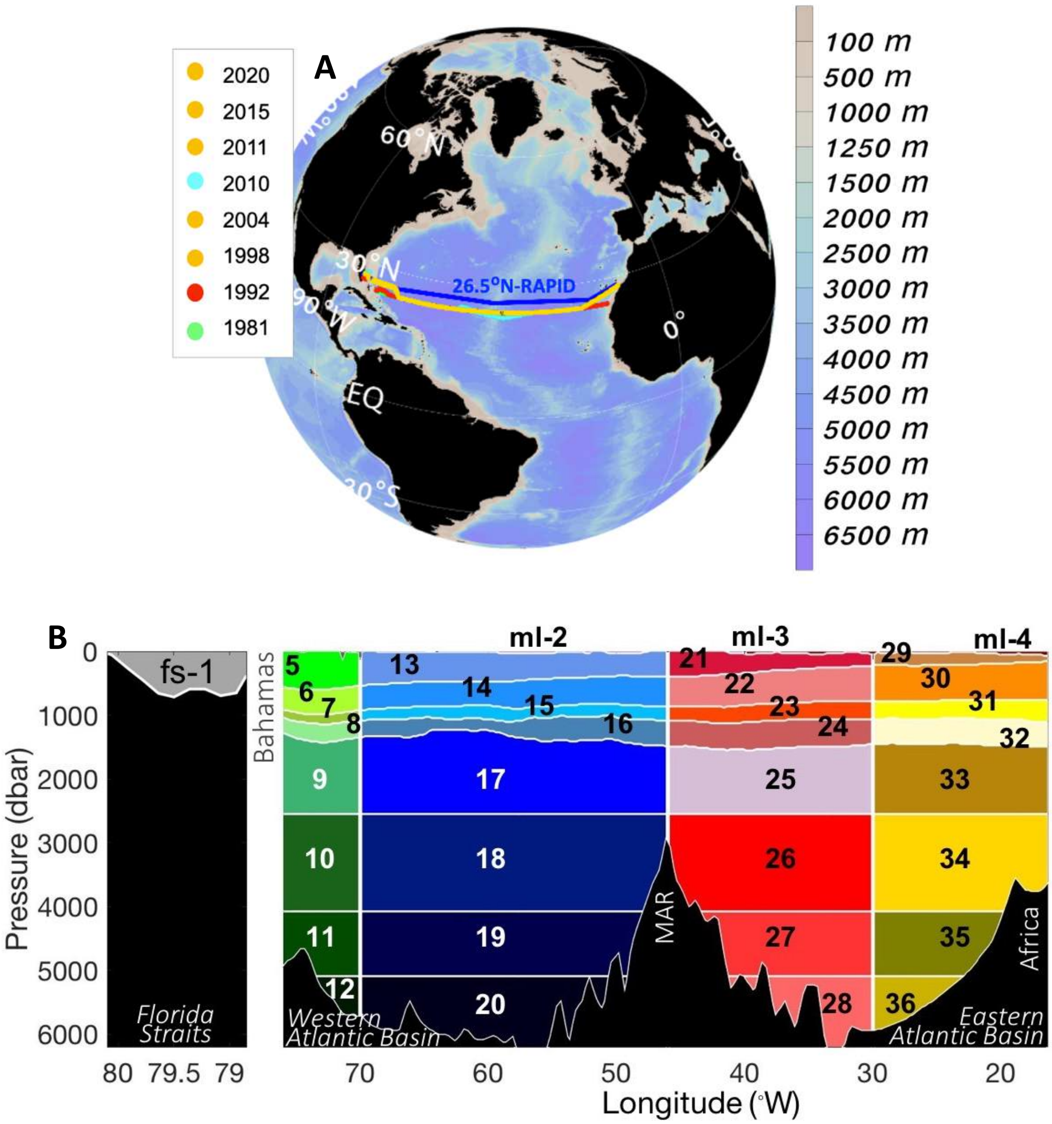

Fig. S1. (**A**) **MLR input data location;** (**B**) **MLR spatial subregion division.** The longitudinal limits (ºW) are: 80 to 79 (fs-1), 79 to 64 (ml-2), 64 to 40 (ml-3), 40 to 10 ml-4), 78 to 70 (boxes 5 to 12), 70 to 46 (boxes 13 to 20), 46 to 30 (boxes 21 to 28), 30 to 10 (boxes 29 to 36); and the vertical limits (applied to the Atlantic basin but not to Florida Strait) are: surface to γ= 26.0 kg m^{-3}; γ= 26.0 to 26.7 kg m^{-3}; γ=26.7 to 27.4 kg m-3; γ= 27.4 to 27.65 kg m^{-3}; γ= 27.65 to 27.85 kg m^{-3}; γ= 27.85 kg m^{-3} to 2500 dbar; 2500 to 4000 dbar; 4000 to 5000 dbar, 5000 dbar to bottom. γ is the so-called neutral density[94], equivalent to the more conventional potential densities. Note MLR boxes Nos. 2 to 4 (ml-2, ml-3, ml-4) refer to the uppermost mixed layer (ml) boxes.

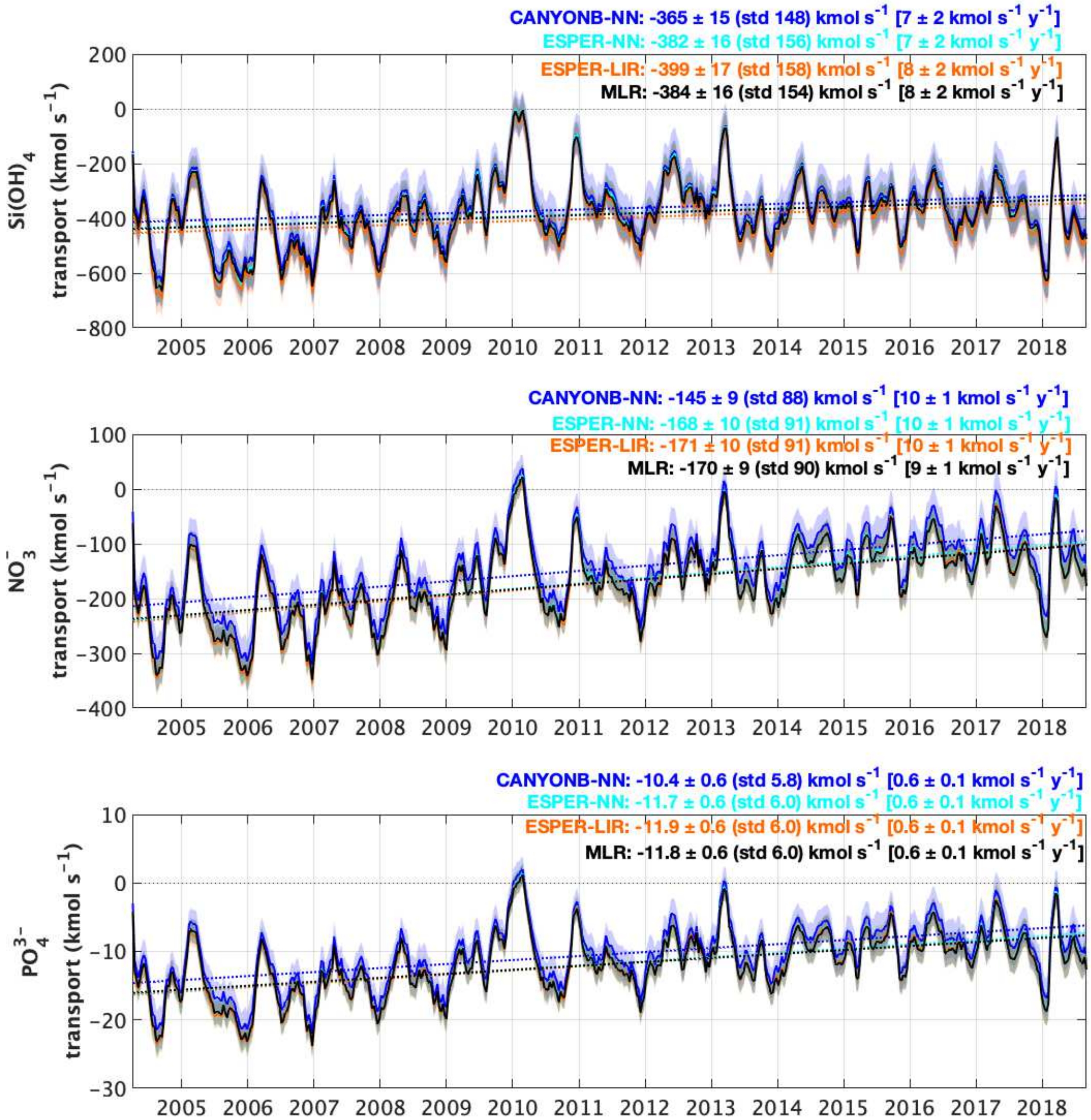

Fig. S2. Neural-network vs MLR nutrient transport time series. Total (**A**) silicate, $Si(OH)_4$, (**B**) nitrate, NO_3^-, and (**C**) phosphate, PO_4^{3-}, total transports across the 26.5°N section. Black lines and numbers refer to the Multi-Linear Regression (MLR)-derived nutrient transports, as presented in Fig. 3. In blue, cyan and orange, the Neural Network (NN) CANYON-B, the ESPER-NN and ESPER-LIR derived nutrient transport. Bold lines are smoothed (moving average filter of 5-point running mean) nutrient transports, the colour shading represent the nutrient transport uncertainties, and dotted lines are the observation-period tendencies. Coloured numbers are the 14-year averages ± standard error (negative fluxes mean southwards); in parenthesis, the standard deviation of the transports (std); and, in brackets, the tendencies ± standard error.

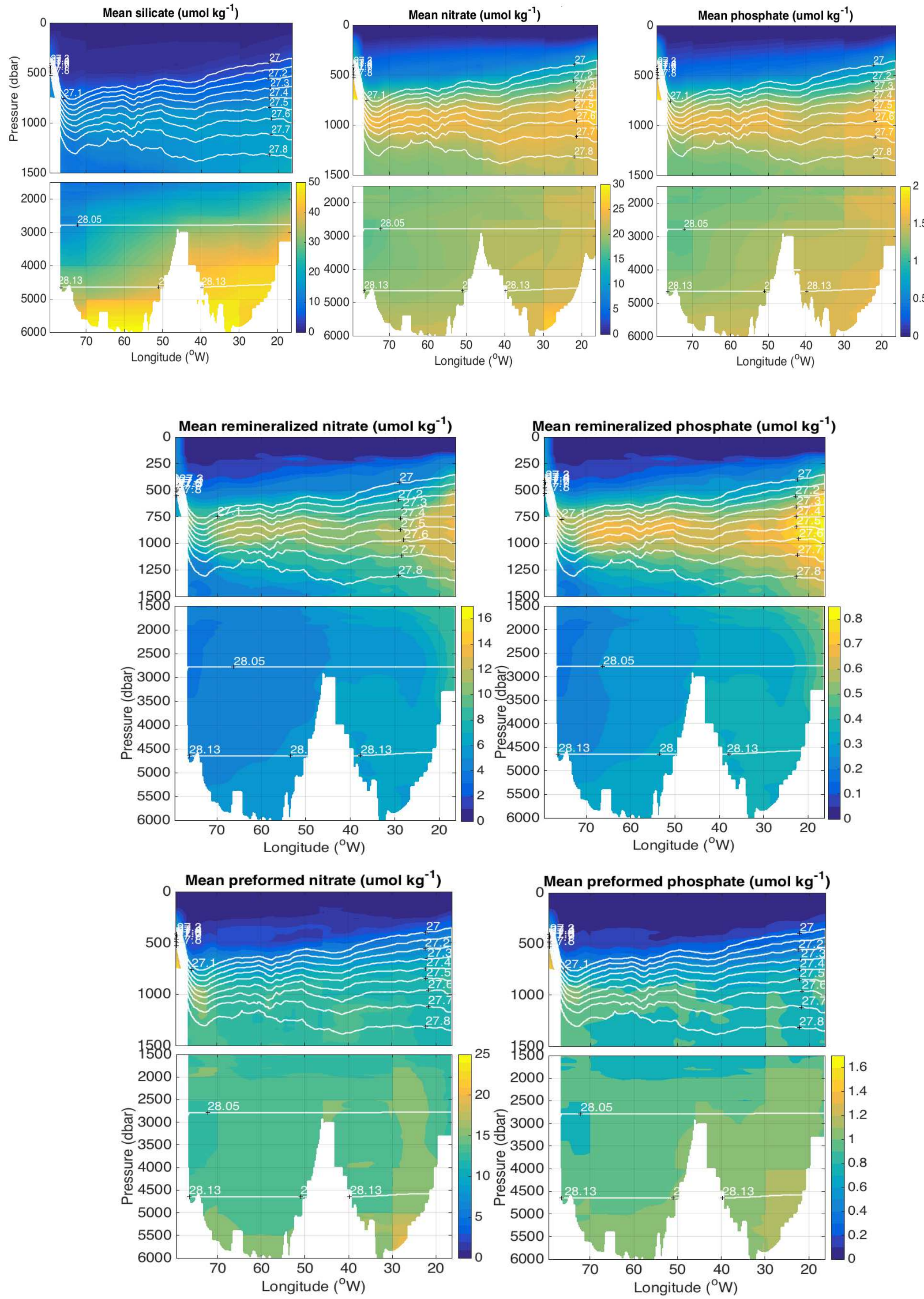

Fig. S3. MLR-derived mean nutrient distributions. (**A**) Silicate, (**B**) nitrate, (**C**) phosphate (14-year average) mean distributions, and nitrate and phosphate decomposed into their remineralized (**D, E**) and preformed (**F, G**) fractions. White contours represent neutral density isopycnals. Note Florida Straits is not included.

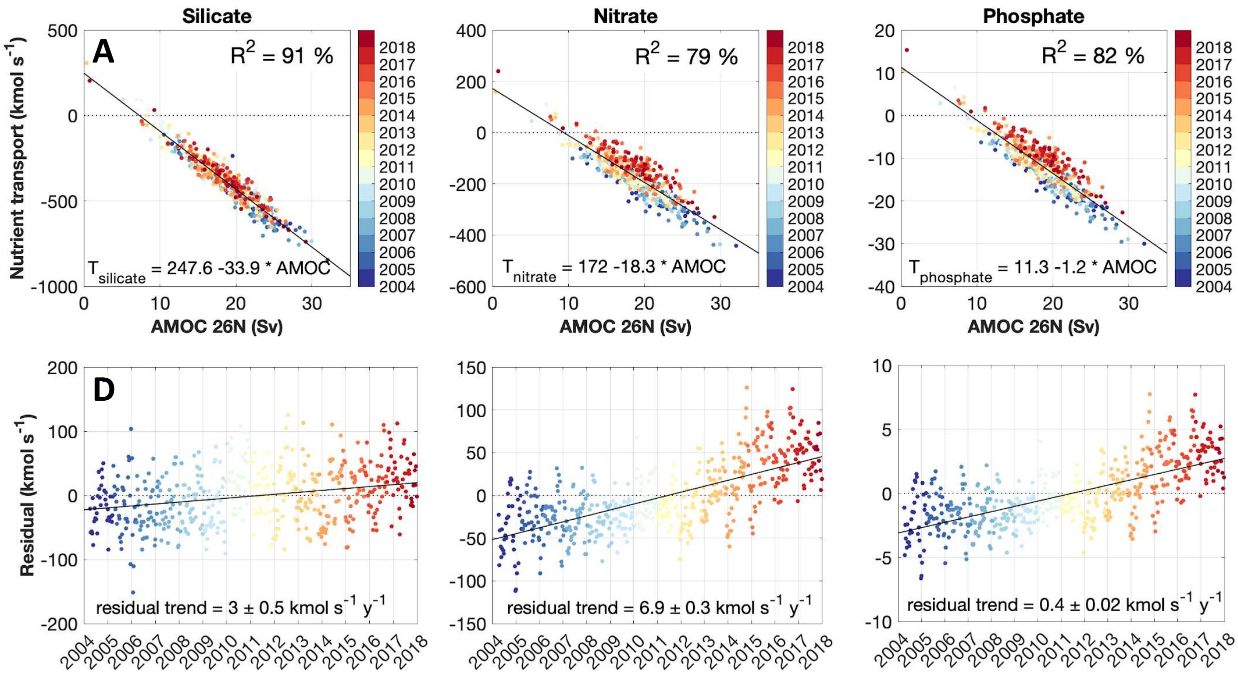

Fig. S4. AMOC vs. nutrient transport co-variability and non-AMOC (residual) variability. Upper panels: (**A**) Silicate, (**B**) nitrate, (**C**) phosphate transports vs AMOC transport. R^2 represents the percentage of variance explained by AMOC. Lower panels: Temporal variability of the residual between observed nutrient transport and that predicted by linear AMOC-nutrient transport relationship for (**D**) silicate, (**E**) nitrate, and (**F**) phosphate. The dotted line represents the linear fitting (tendency) of the residual for the period of study 2004 to 2018.

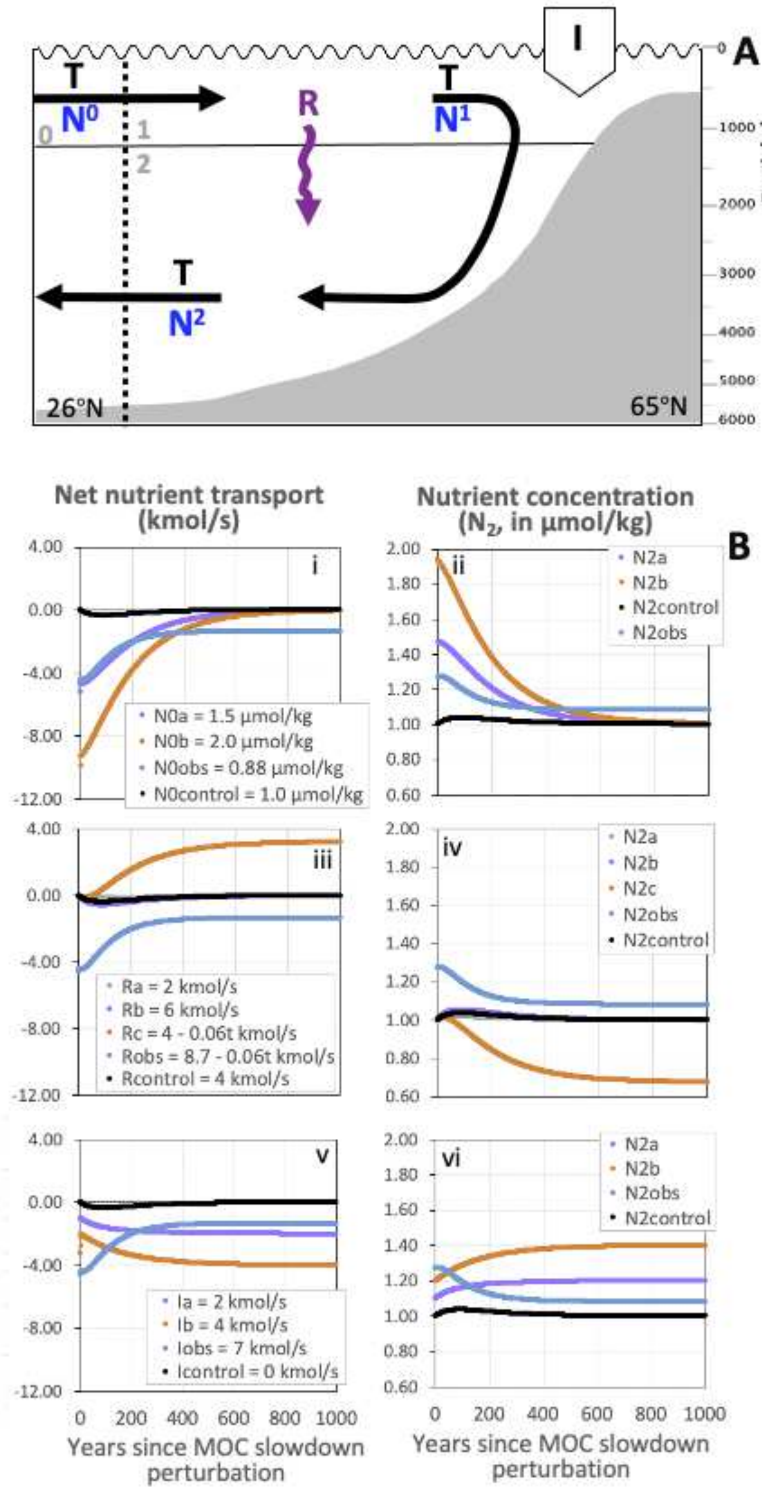

Fig. S5. Theoretical 2-box model. (**A**) Simple schematics of the two-box theoretical model. N is the general notation for the nutrient concentration (subindex 0, 1 and 2 referring to boxes 0, 1, and 2, respectively), T refers to the AMOC transport, R to remineralization, and I to the additional nutrient input, (**B**) Nutrient transport (left panels) and nutrient concentration in the lower AMOC limb (N_2) at different model set ups: changing N_0 (*i, ii*), changing R (*iii, iv*) or changing I (*v, vi*).

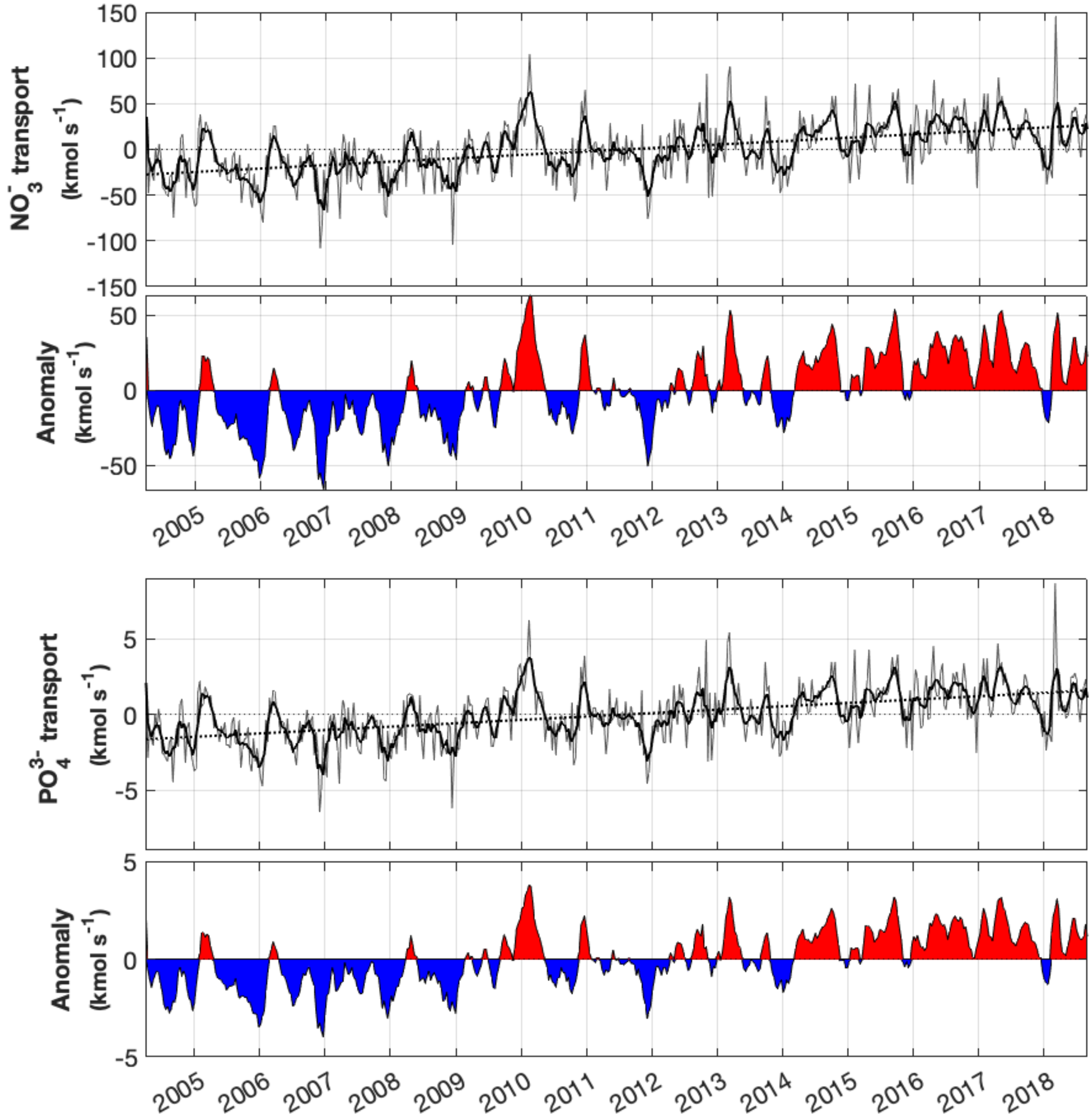

Fig. S6. Remineralized nutrient transport time series. Upper panels: (**A**) remineralized nitrate time series, and (**B**) remineralized nitrate time series anomaly. Lower panels: (**C**) remineralized phosphate, and (**F**) remineralized phosphate transport time series anomaly. In panels A and C, thin lines are the 10-day time series, bold lines are smoothed versions (moving average filter of 5-point running mean), and dotted lines are the linear fits (3.7 ± 0.3 kmol s^{-1} y^{-1}, 0.22 ± 0.2 kmol s^{-1} y^{-1} for remineralized nitrate transport and remineralized phosphate transport, respectively)**.**

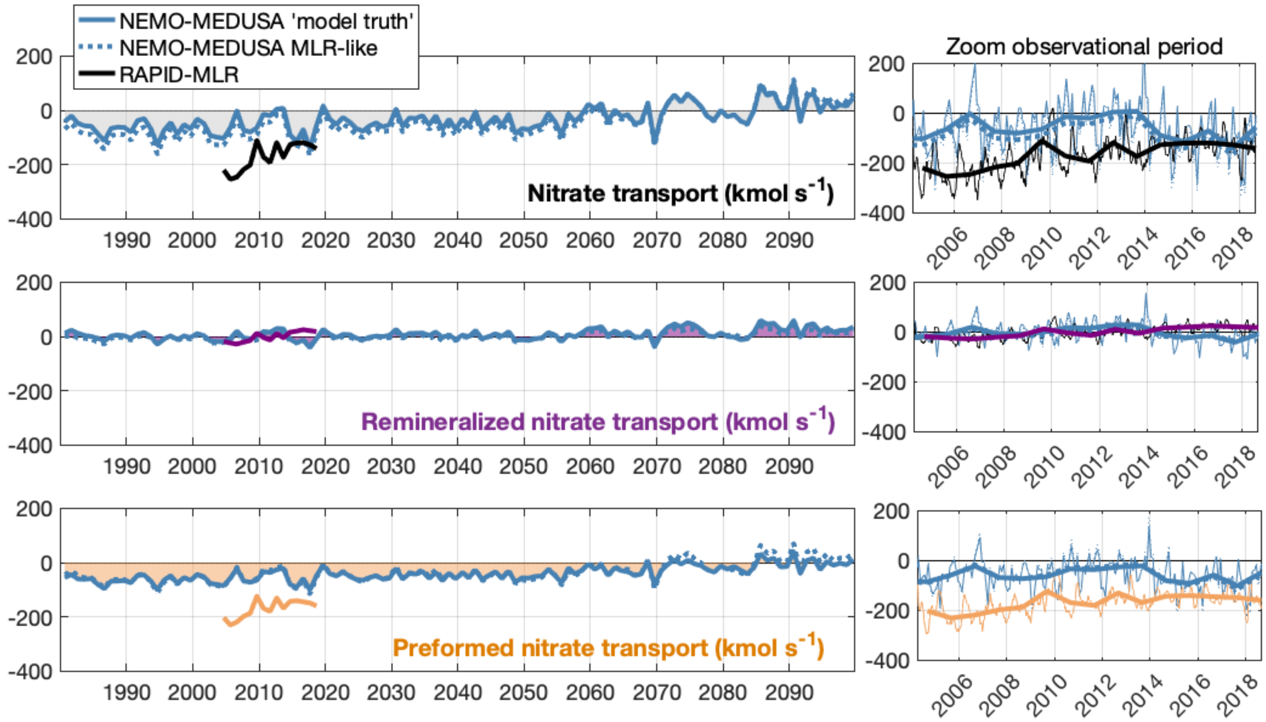

Fig. S7. Application of MLR-nutrient transport calculation methodology to model 1° NEMO-MEDUSA outputs. (**A**) Total, (**B**) remineralized, (**C**) preformed nutrient transport for 1980-2100 (left panels) and 2004-2018 (right panels).

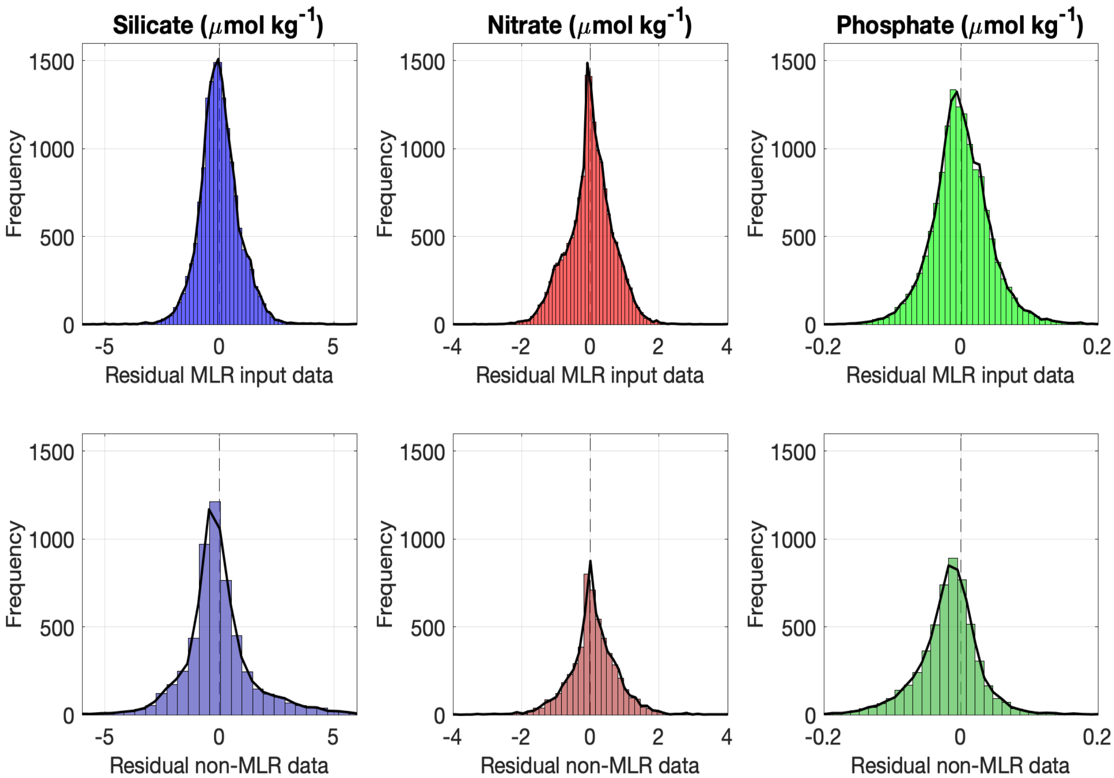

Fig. S8. MLR residuals. Residuals account for the difference between the observed nutrient minus the MLR-predicted value for silicate (in blue); nitrate (in red); and phosphate (in green) (**A, B, C**) All data used as input to the MLR (see table S1); (**D, E, F**) GLODAPv2.2021 data between 22-30°N not used as input to the MLR.

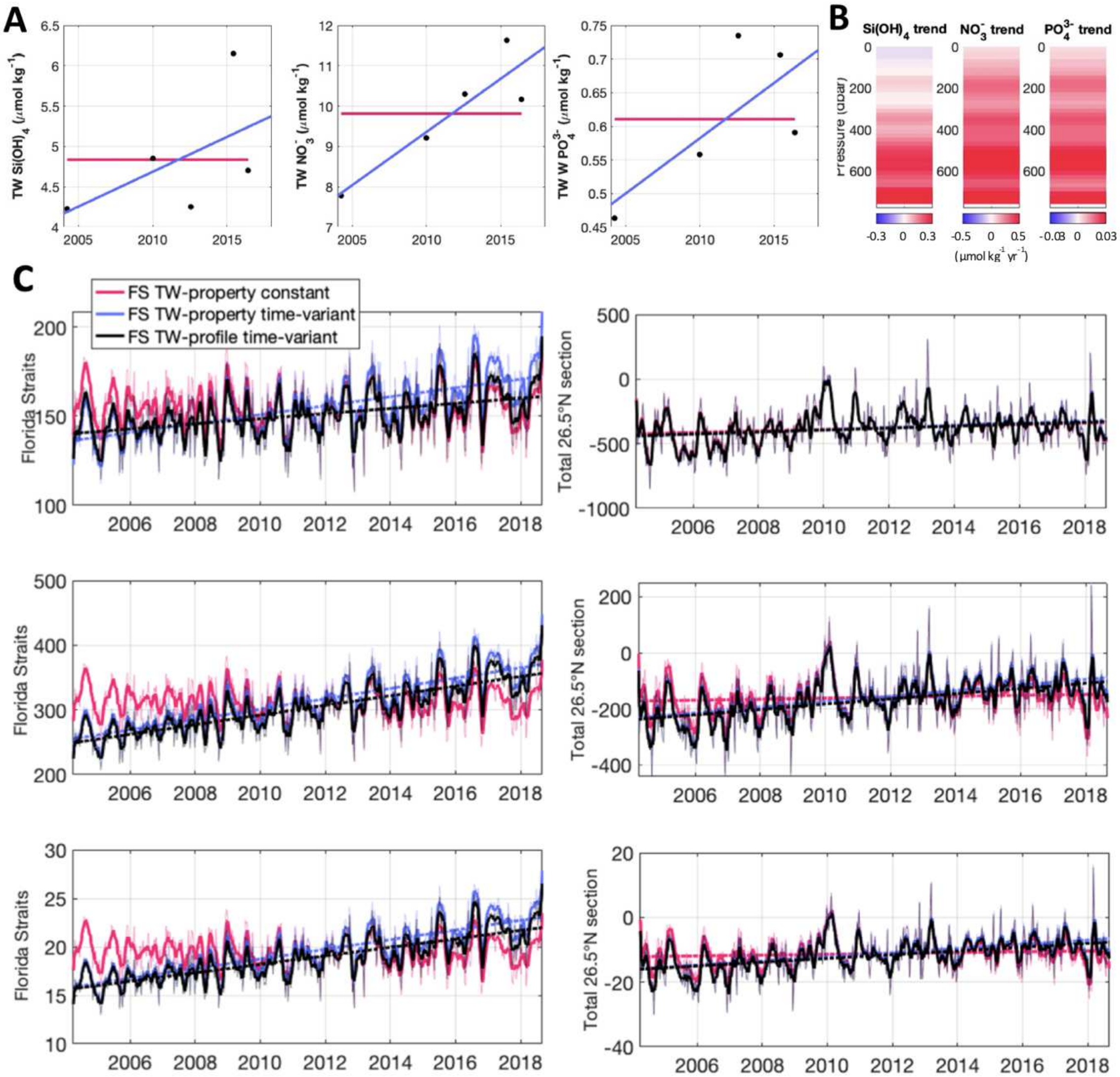

Fig. S9. Florida Straits (FS) nutrient and nutrient transports: sensitivity tests. (**A**) Transport-weighted nutrient concentrations. Pink lines indicate the averages (used in FS-sensitivity test 1), purple lines represent the linear predictive fits (used in FS-sensitivity test 2). (**B**) Water-column nutrient tendencies (used in FS-sensitivity test 3). Tendencies are obtained from the zonally averaged transport-weighted nutrient profiles for the 2004, 2010, 2012, 2015 and 2016 cruises (ref. table S1). (**C**) Time series of silicate, $Si(OH)_4$, nitrate, NO_3^-, and phosphate, PO_4^{3-}, transports across the Florida Straits (left panels) and across the 26.5ºN section (right panels). Colour legend represent the three sensitivity tests performed: test 1, nutrient transport estimates by using a constant transport-weighted property (pink lines); test 2, nutrient transport estimates by using a time-variant transport-weighted property (purple lines); and test 3, nutrient transport estimates by using a vertical time-variant property profile (black lines).

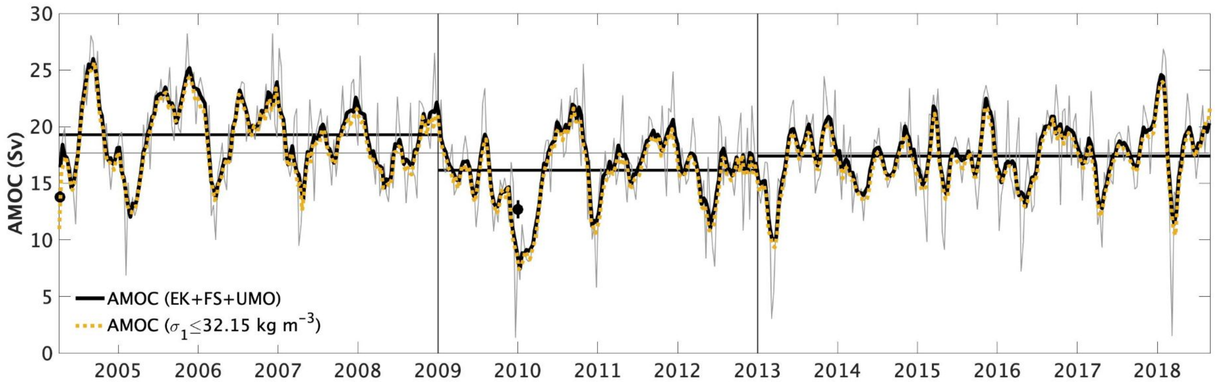

Fig. S10. Atlantic Meridional Overturning Circulation (AMOC) time series: *i)* as the sum of the Florida Current transport, the upper ocean (surface to 1100 dbar) geostrophic transport east of the Bahamas, and the Ekman transport, namely RAPID AMOC time series[17]. Thin grey line is the 10-day time series ad black bold line is the moving average filter of 5-point running mean; and *ii)* as the surface to σ_{moc} integrated transport (orange dotted line), where σ_{moc} accounts for the isopycnal broadly separating the upper and lower limbs of the AMOC, σ_1 **=** 32.15* kg m^{-3} (σ_1 is the potential density referenced to 1000 dbar)[15,16,70]. Black dots are the hydrographic cruise-based estimates (cruise references in table S1).

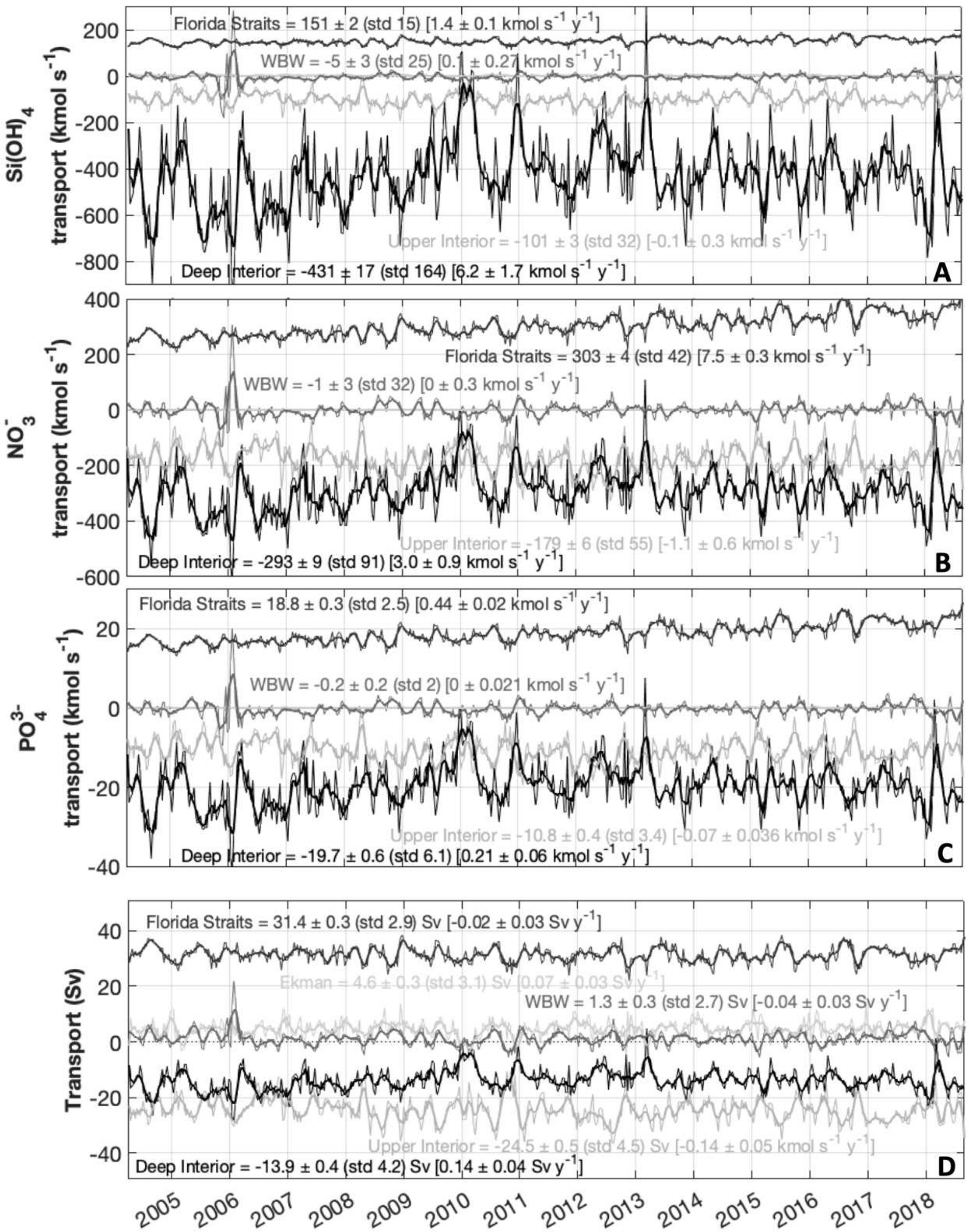

Fig. S11. Nutrient time series by subregions. (**A**) Silicate, (**B**) nitrate, (**C**) phosphate transports (kmol s^{-1}; thin lines) for each (**D**) volume-estimate subregion[29]. Numbers represent the time-period average (in parenthesis, the standard deviation). Thick lines are the (5-point running mean) smoothed transports. Time series run from April 2004 to August 2018. Positive (negative) transports are northward (southward). Note Ekman nutrient transport is close to zero, and therefore is not plotted.

Table S1. List of hydrographic cruises used in this study.

Cruise Name	Section	Date		Vessel	P.I.	#St	Reference
Atlantis 109, Leg 3	FS, Atl	12 Aug-6 Sep	1981	*Atlantis II*	D. Roemmich	90	37,95–97
WOCE A05 HE06	Atl	14 Jul-15 Aug	1992	*Hesperides*	G. Parrilla	118	37,64,96,97
WOCE AR01 (AR05)	FS, Atl	23 Jan-24 Feb	1998	*Ronald H. Brown*	K. Lee	130	64
CLIVAR A05_2004*	FS$^+$, Atl	4 Apr-10 May	2004*	*Discovery*	S. Cunningham	125	64,96
A05*	FS$^+$, Atl	5 Jan-19 Feb	2010*	*Discovery*	B. King	135	64,96
A05	FS, Atl	27 Jan-15 Mar	2011	*Hesperides*	A. Hernández- Guerra	167	64,98
GOMECC-2	FS$^+$	27-30 Jul	2012	*Ronald H. Brown*	R. Wanninkhof	12	99
FC1505	FS$^+$	26-27 May	2015	*Walton Smith*	J.A. Hooper, M.O. Baringer	9	100
FC1507	FS$^+$	14-15 Jul	2015	*Walton Smith*	J.A. Hooper, M.O. Baringer	9	100
FC1509	FS$^+$	8-9 Sep	2015	*Walton Smith*	J.A. Hooper, M.O. Baringer	9	100
FC1511	FS$^+$	10-11 Nov	2015	*Walton Smith*	J.A. Hooper, M.O. Baringer	9	100
A05	FS$^+$, Atl	9 Dec-22 Jan	2015	*Discovery*	B. King	145	64
FC1603	FS$^+$	23-24 Mar	2016	*Walton Smith*	J.A. Hooper, M.O. Baringer	9	101
FC1605	FS$^+$	16-17 May	2016	*Walton Smith*	J.A. Hooper, M.O. Baringer	9	101
FC1607	FS$^+$	13-14 Jul	2016	*Walton Smith*	J.A. Hooper, M.O. Baringer	9	101
FC1609	FS$^+$	15-16 Sep	2016	*Walton Smith*	J.A. Hooper, M.O. Baringer	9	101
FC1612	FS$^+$	12-13 Dec	2016	*Walton Smith*	J.A. Hooper, M.O. Baringer	9	101
A05	FS, Atl	19 Jan-1 Mar	2020	*James Cook*	A. Sanchez-Franks	135	**

P.I. denotes principal investigator, #St the number of stations selected, *FS* refers to the Florida Straits and *Atl* to the Atlantic section east of the Bahamas. Superscript $^+$ indicate the FS data used to assess the FS nutrient trends (fig. S8). Superscript * marks the cruises for which the quasi-synoptic nutrient transports were computed by [15] (Fig. 3, black dots). ** https://cchdo.ucsd.edu/cruise/740H20200119

Table S2. Estimates of nutrient and transport uncertainty. When combined in quadrature each 10-day estimate of nutrient flux has an uncertainty of 39 kmol-Si s^{-1}, 19 kmol-N s^{-1} and 1.6 kmol-P s^{-1}. If we assume that there are 12 independent estimates in the year then the uncertainty on the annual average nutrient transports is $39/(12)^{1/2}=11$ kmol-Si s^{-1}, $19/(12)^{1/2}=6$ kmol-N s^{-1} and $1.6/(12)^{1/2}=0.5$ kmol-P s^{-1}; and $11/(14)^{1/2}=3$ kmol-Si s^{-1}, $6/(14)^{1/2}=1$ kmol-N s^{-1} and $0.5/(14)^{1/2}=0.1$ kmol-P s^{-1} for the full time-series mean. Note the table also shows the standard error of the time series mean, i.e., $std/(df)^{1/2}$, with std the standard deviation of the time series (154 kmol-Si s^{-1}, 90 kmol-N s^{-1}, and 6.0 kmol-P s^{-1}), and df the degrees of freedom (df=91[29]).

	NT *kmol s^{-1}*	σT_{reg} Sv	$\langle N\rangle_{reg}$ μmol kg^{-1}	$\langle N\rangle_{avg}$ μmol kg^{-1}	$\langle N\rangle_{reg}$- $\langle N\rangle_{avg}$ μmol kg^{-1}	σNT_T *kmol s^{-1}*	σN_{reg} μmol kg^{-1}	$\langle T\rangle_{reg}$ Sv	σNT_N *kmol s^{-1}*	**σNT kmol s^{-1}**
Silicate										
Florida Straits	150.7	1.0	8.4	26.1	17.7	*18.4*	5.5	31.4	*15.9*	**24.3**
Ekman	2.4	0.35	0.5	26.1	25.6	*9.5*	0.3	4.6	*0.2*	**9.5**
Wedge	-5.1	0.19	5.94	26.1	20.2	*16.1*	5.8	1.9	*0.2*	**16.1**
Upper interior	-101.2	0.9	10.6	26.1	15.5	*15.0*	6.7	24.5	*0.7*	**15.0**
Deep interior	-430.8	2.0	34.6	26.1	-8.5	*17.0*	9.5	13.9	*0.1*	**17.0**
Compensation	74.4	-	-	-	-	-	1.9	3.0	*6.0*	**6.0**
Bering Strait	18.9	0.2	23.6	25.3	1.7	*0.3*	3.4	0.8	*2.7*	**2.7**
Total uncertainty in individual 10-day silicate transport estimates										**39**
Standard error of the 14-yr mean silicate transport										**16**
Nitrate										
Florida Straits	302.9	1.0	15.4	19.1	3.7	*4.0*	8.7	31.4	*14.6*	**15.2**
Ekman	0.2	0.35	0.04	19.1	19.1	*7.0*	0.1	4.6	*0.2*	**7.0**
Wedge	-0.7	0.19	11.46	19.1	7.7	*6.1*	9.4	1.9	*0.3*	**6.1**
Upper interior	-178.6	0.9	16.3	19.1	2.8	*2.8*	8.1	24.5	*0.90*	**2.9**
Deep interior	-293.3	2.0	20.7	19.1	-1.6	*3.3*	1.3	13.9	*0.1*	**3.3**
Compensation	57.7	-	-	-	-	-	0.5	3.0	*1.4*	**1.4**
Bering Strait	5.9	0.2	7.4	19.3	11.9	*2.4*	2.2	0.8	*1.8*	**3.0**
Total uncertainty in individual 10-day nitrate flux estimates										**19**
Standard error of the 14-yr mean nitrate transport										**9**
Phosphate										
Florida Straits	18.8	1.0	1.0	1.3	0.3	*0.3*	0.6	31.4	*1.04*	**1.1**
Ekman	0.1	0.35	0.01	1.3	1.2	*0.5*	0.02	4.6	*0.04*	**0.5**
Wedge	-0.2	0.19	0.70	1.3	0.6	*0.4*	0.6	1.9	*0.05*	**0.5**
Upper interior	-10.8	0.9	1.0	1.3	0.2	*0.2*	0.5	24.5	*0.11*	**0.3**
Deep interior	-19.7	2.0	1.4	1.3	-0.1	*0.3*	0.1	13.9	*0.01*	**0.3**
Compensation	3.9	-	-	-	-	-	0.03	3.0	*0.09*	**0.09**
Bering Strait	1.2	0.2	1.5	1.3	-0.2	*0.04*	0.2	0.8	*0.16*	**0.2**
Total uncertainty in individual 10-day phosphate flux estimates										**1.6**
Standard error of the 14-yr mean phosphate transport										**0.6**

Table S3. Summary table of the sensitivity test results. Bold numbers correspond to the results presented in the main text shown here as reference, that is, the results by applying the MLR equations to the WOA18 oxygen data with added tendencies as estimated by means of the hydrographic data (table S10); Test 1, refers to the results by applying the MLR equations to the original WOA18 oxygen data (seasonal climatology, no trend); Test 2, comprises the results by using ESPER_LIR_TS (i.e. no oxygen as a predictor variable) instead of the MLR equations; Test 3 (test 4), refers to the results by using lower-bound (upper-bound) stoichiometric ratios to compute the remineralized nutrient fraction (eq. 5, in Materials and Methods). Further details in the 'Sensitivity analysis' section in Supplementary Methods.

		Mean			Observation-period tendencies		
		total	*remin.*	*preform.*	*total*	*remin.*	*preform.*
Phosphate transport by flow components							
Total transport	**Main**	**-11.8 ± 0.6**	**-0.1 ± 0.2**	**-11.8 ± 0.4**	**0.58 ± 0.06**	**0.22 ± 0.02**	**0.36 ± 0.04**
	Test 1	-11.6	0.4	-12.1	0.61	0.33	0.28
	Test 2	-16.3	-1.7	-14.6	0.17	0.03	0.14
	Test 3	-11.8	0.5	-12.3	0.58	0.49	0.09
	Test 4	-11.8	0.2	-12.0	0.58	0.16	0.42
Overturning component	**Main**	**-19.9 ± 0.6**	**-4.9 ± 0.2**	**-15.0 ± 0.4**	**0.15 ± 0.06**	**0.03 ± 0.02**	**0.12 ± 0.04**
	Test 1	-19.9	-5.0	-14.9	0.14	0.02	0.12
	Test 2	-19.6	-5.0	-14.6	0.10	0.02	0.08
	Test 3	-19.9	-7.6	-12.3	0.14	0.05	0.10
	Test 4	-19.9	-2.5	-17.3	0.14	0.02	0.13
Horizontal component	**Main**	**9.6 ± 0.2**	**5.4 ± 0.1**	**4.2 ± 0.1**	**0.43 ± 0.01**	**0.19 ± 0.01**	**0.23 ± 0.01**
	Test 1	9.9	6.0	3.9	0.46	0.31	0.15
	Test 2	5.0	3.9	1.1	0.06	0.01	0.05
	Test 3	9.6	8.9	0.7	0.42	0.44	-0.01
	Test 4	9.6	3.0	6.6	0.42	0.15	0.28
Throughflow component	**Main**	**-1.6± 0.1**	**-0.6± 0.1**	**-1.0± 0.1**	**0.010± 0.003**	**0.003± 0.001**	**0.007± 0.002**
	Test 1	-1.6	-0.6	-1.0	0.010	0.003	0.007
	Test 2	-1.6	-0.6	-1.0	0.009	0.004	0.006
	Test 3	-1.6	-0.9	-0.7	0.010	0.005	0.005
	Test 4	-1.6	-0.3	-1.3	0.010	0.002	0.008
Phosphate transport by regions							
Florida Straits	**Main**	**18.8 ± 0.3**	**11.4 ± 0.1**	**7.5 ± 0.1**	**0.44 ± 0.02**	**0.2 ± 0.01**	**0.23 ± 0.01**
	Test 1	18.8	11.7	7.1	0.43	0.30	0.14
	Test 2	14.4	9.6	4.8	-0.01	-0.01	0.00
	Test 3	18.8	18.1	0.7	0.43	0.46	-0.02
	Test 4	18.8	6.0	12.8	0.43	0.15	0.28
Atlantic basin (≤1100 dbar)	**Main**	**-4.7 ± 0.2**	**-2.9 ± 0.1**	**-1.7 ± 0.1**	**-0.06 ± 0.03**	**-0.04 ± 0.01**	**-0.02 ± 0.01**
	Test 1	-4.7	-2.9	-1.7	-0.04	-0.03	-0.01
	Test 2	-5.0	-2.9	-2.1	-0.02	-0.03	0.01
	Test 3	-4.8	-4.7	-0.2	-0.06	-0.06	0.00
	Test 4	-4.8	-1.6	-3.3	-0.06	-0.02	-0.04
uAMOC (≤1100 dbar)	**Main**	**14.2 ± 0.3**	**8.4 ± 0.1**	**5.7 ± 0.1**	**0.38 ± 0.02**	**0.17 ± 0.01**	**0.21 ± 0.01**
	Test 1	14.1	8.8	5.4	0.40	0.27	0.13
	Test 2	9.4	6.7	2.7	-0.03	-0.04	0.01
	Test 3	14.0	13.4	0.5	0.37	0.40	-0.02
	Test 4	14.0	4.5	9.5	0.37	0.13	0.24
lAMOC (>1100 dbar)	**Main**	**-26.0 ± 0.7**	**-8.5 ± 0.2**	**-17.5 ± 0.5**	**0.21 ± 0.07**	**0.06 ± 0.02**	**0.15 ± 0.05**
	Test 1	-25.8	-8.3	-17.5	0.21	0.06	0.15
	Test 2	-25.6	-8.3	-17.3	0.20	0.06	0.13
	Test 3	-25.8	-13.0	-12.9	0.21	0.09	0.12
	Test 4	-25.8	-4.3	-21.5	0.21	0.03	0.18
Phosphate concentration by regions							
Florida Straits	**Main**	**0.58 ± 0.03**	**0.35 ± 0.01**	**0.23 ± 0.02**	**0.0139 ± n.a.**	**0.0065 ± n.a.**	**0.0073 ± n.a.**
	Test 1	0.58	0.36	0.22	0.014	0.0137	0.0093
	Test 2	0.45	0.30	0.15	0.000	0.0000	0.0000
	Test 3	0.58	0.56	0.02	0.014	0.0138	0.0144
	Test 4	0.58	0.19	0.40	0.014	0.0138	0.0048
Atlantic Basin (≤1100 dbar)	**Main**	**0.33 ± 0.13**	**0.21 ± 0.08**	**0.12 ± 0.06**	**0.0009 ± 0.0017**	**0.0008± 0.0009**	**0.0001 ± 0.0009**
	Test 1	0.32	0.20	0.12	-0.001	-0.0009	0.0000
	Test 2	0.35	0.20	0.15	-0.003	-0.0031	0.0003
	Test 3	0.33	0.32	0.01	0.001	0.0009	0.0013
	Test 4	0.33	0.11	0.22	0.001	0.0009	0.0004
uAMOC (≤1100 dbar)	**Main**	**0.88 ± 0.24**	**0.52 ± 0.17**	**0.36 ± 0.08**	**0.0495 ± 0.0160**	**0.0254 ± 0.0090**	**0.0241± 0.0070**
	Test 1	0.89	0.55	0.34	0.0508	0.0325	0.0183
	Test 2	0.58	0.41	0.17	0.0166	0.0099	0.0066
	Test 3	0.88	0.84	0.03	0.0493	0.0492	0.0002
	Test 4	0.88	0.28	0.60	0.0493	0.0163	0.0330
lAMOC (>1100 dbar)	**Main**	**1.35±0.02**	**0.44±0.02**	**1.35±0.02**	**-0.0008±0.0006**	**0.0001±0.0001**	**-0.0009±0.0005**
	Test 1	1.35	0.43	0.91	-0.0011	-0.0002	-0.0010
	Test 2	1.34	0.43	0.90	-0.0005	-0.0002	-0.0003
	Test 3	1.35	0.68	0.67	-0.0008	0.0002	-0.0010

	Test 4	1.35	0.22	1.12	-0.0008	0.0001	-0.0009

Table S4. Multi-Linear Regression (MLR) vs ESPER_NN (NN) nutrient transports. Silicate, nitrate and phosphate nutrient transports for the MLR regions (fig. S1b) with the lowest MLR performance (i.e. $R^2<0.4$, table S8). For each region, the 2004-2018 average nutrient transport (and time series tendency) was estimated by using the MLR-nutrient and the NN-nutrient fields. The difference between both estimates (MLR minus NN) is also shown. Correlation (%) accounts for the coefficient of determination (in %) obtained by regressing the time series of the MLR-nutrient transport vs NN-nutrient transport. Numbers in italics represent the values for the total section.

Silicate	**Average transport (kmol s^{-1})**			**Tendency (kmol s^{-1} yr^{-1})**			
	-384 ± 16	-382 ± 16		8 ± 2	7 ± 2		
MLR region	MLR	NN	Difference	MLR	NN	Difference	Correlation (%)
3	-0.5	-0.3	0.20	-0.07	-0.07	0.001	88.8
Nitrate	**Average transport (kmol s^{-1})**			**Tendency (kmol s^{-1} yr^{-1})**			
	-170 ± 9	-168 ± 10		9 ± 1	10 ± 1		
MLR region	MLR	NN	Difference	MLR	NN	Difference	Correlation (%)
2	0.7	0.4	0.29	0.06	0.02	0.048	58.9
3	-0.3	0.0	0.30	-0.05	0.00	0.042	29.9
9	-24.1	-24.0	0.06	0.00	0.02	0.020	100.0
10	-15.1	-15.1	0.06	0.15	0.16	0.017	100.0
28	4.2	4.4	0.18	0.11	0.11	0.005	100.0
35	-11.2	-11.3	0.13	0.28	0.28	0.001	99.9
36	1.5	1.5	0.02	0.06	0.07	0.002	100.0
Phosphate	**Average transport (kmol s^{-1})**			**Tendency (kmol s^{-1} yr^{-1})**			
	-11.8 ± 0.6	-11.7 ± 0.6		0.6 ± 0.1	0.6 ± 0.1		
MLR region	MLR	NN	Difference	MLR	NN	Difference	Correlation (%)
2	0.03	0.03	0.000	0.003	0.001	0.0018	57.8
3	-0.01	0.01	0.024	-0.002	0.000	0.0019	0.2
4	0.00	0.00	0.006	-0.001	0.000	0.0006	57.7
9	-1.59	-1.60	0.004	0.001	0.002	0.0004	100.0
28	0.28	0.29	0.008	0.007	0.007	0.0001	100.0
35	-0.76	-0.76	0.000	0.019	0.019	0.0002	99.9
36	0.10	0.10	0.003	0.004	0.004	0.0000	100.0

Table S5. Mean (and observation-period tendencies) of the volume and phosphate transports, and phosphate concentrations, at 26.5°N. Positive (negative) mean volume and nutrient transports refer to northward (southward) advection, but for the overturning and horizontal volume transports, for which positive values account for the total magnitude of each component. Tendencies are the linear fit of the high-frequency time-series over the observation period. Positive (negative) tendencies refer to an increase (decrease) over the period of study: for transports, increase (decrease) refers to a larger (lower) transport to the North over time; for tracer concentration, increase (decrease) accounts for a higher (lower) tracer concentration over time. Units: mean volume transports in Sv (1 Sv = 10^6 m^3 s^{-1}), and tendencies in Sv yr^{-1}; mean tracer transport in kmol s^{-1}, and tendencies in kmol s^{-1} yr^{-1}; mean tracer concentration refers to the transport-weighted property, in µmol kg^{-1}, and tendencies in µmol kg^{-1} yr^{-1}. Uncertainties represent the standard errors. *The notation uAMOC refers to the total integrated transport ≤1100 dbar (roughly equivalent to σ_1≤32.15 kg m^{-3}). ** The notation lAMOC refers to the total integrated transport >1100 dbar (roughly equivalent to σ_1>32.15 kg m^{-3}).

			Volume	Phosphate Total	Phosphate Remineralized	Phosphate Preformed
Volume and phosphate transport by flow components						
Mean		total transport	-1.2 ± 0.2	-11.8 ± 0.6	-0.1 ± 0.2	-11.8 ± 0.4
Mean		overturning component	18.6 ± 4.3	-19.9 ± 0.6	-4.9 ± 0.2	-15.0 ± 0.4
Mean		horizontal component	45.4 ± 5.9	9.6 ± 0.2	5.4 ± 0.1	4.2 ± 0.1
Tendency		total transport	0.007±0.002	0.58 ± 0.06	0.22 ± 0.02	0.36 ± 0.04
Tendency		overturning component	-0.13 ± 0.05	0.15 ± 0.06	0.03 ± 0.02	0.12 ± 0.04
Tendency		horizontal component	-0.09 ± 0.06	0.43 ± 0.01	0.19 ± 0.01	0.23 ± 0.01
Volume and phosphate transport by upper/lower AMOC limbs						
Mean	uAMOC*	Florida Straits	32 ± 3	18.8 ± 0.3	11.4 ± 0.1	7.5 ± 0.1
Mean	uAMOC*	upper interior	-15 ± 4	-4.7 ± 0.2	-2.9 ± 0.1	-1.7 ± 0.1
Mean	uAMOC*	total uAMOC	17 ± 4	14.2 ± 0.3	8.4 ± 0.1	5.7 ± 0.1
Mean	lAMOC**	total lAMOC	-18 ± 4	-26 ± 0.7	-8.5 ± 0.2	-17.5 ± 0.5
Tendency	uAMOC*	Florida Straits	-0.02 ± 0.03	0.44 ± 0.02	0.2 ± 0.01	0.23 ± 0.01
Tendency	uAMOC*	upper interior	-0.12 ± 0.04	-0.06 ± 0.03	-0.04 ± 0.01	-0.02 ± 0.01
Tendency	uAMOC*	total uAMOC	-0.14 ± 0.04	0.38 ± 0.02	0.17 ± 0.01	0.21 ± 0.01
Tendency	lAMOC**	total lAMOC	0.14 ± 0.05	0.21 ± 0.07	0.06 ± 0.02	0.15 ± 0.05
Phosphate concentration						
Mean	uAMOC*	Florida Straits		0.58 ± 0.03	0.35 ± 0.01	0.23 ± 0.02
Mean	uAMOC*	upper interior		0.33 ± 0.13	0.21 ± 0.08	0.12 ± 0.06
Mean	uAMOC*	total uAMOC		0.88 ± 0.24	0.52 ± 0.17	0.36 ± 0.08
Mean	lAMOC**	total lAMOC		1.35 ± 0.02	0.44 ± 0.02	0.91 ± 0.01
Tendency	uAMOC*	Florida Straits		0.0139 ± n.a.	0.0065 ± n.a.	0.0073 ± n.a.
Tendency	uAMOC*	upper interior		0.001 ± 0.002	0.001 ± 0.001	0.000 ± 0.001
Tendency	uAMOC*	total uAMOC		0.050 ± 0.016	0.025 ± 0.009	0.024 ± 0.007
Tendency	lAMOC**	total lAMOC		-0.0008 ± 0.0006	0.0001 ± 0.0001	-0.0009 ± 0.0005

Table S6. Nutrient inputs. Sources (inputs) of silicate, nitrate and phosphate north of the 26.5°N section.

Source	Nutrient flux* ($kmol\ s^{-1}$)	Ref. year**	References
Silicate	**117 ± 12**		
Atm. deposition	0.7 ± 0.7	No time ref.	[102,103]
Fluvial inputs	40 ± 9	No time ref.	[40,76,78]
Arctic sills	64 ± 8	2004, 2010	[40,41,80]
Gibraltar Strait	3.9 ± 0.3	2005-2008	[81]
Other (seafloor weathering, ground water and hydrothermal sources)	8.7 ± 2.2	No time ref.	[76]
Nitrate	**86 ± 14** (no DON = 73 ± 12)		
Atm. deposition	5.9 ± 5.9	2005	[40,51]
Fluvial inputs	3.3 ± 0.5	2000	[40,104]
Arctic sills	21 ± 7	2004, 2010	[40,41,80]
Gibraltar Strait	4.4 ± 0.1	2005-2008	[81]
N_2 fixation	38 ± 8	No time ref.	[40,51,82]
DON	13 ± 6		***
Phosphate	**7 ± 1** (no DOP = 4 ± 1)		
Atm. deposition	0.03 ± 0.03	No time ref.	[75]
Fluvial inputs	0.22 ± 0.06	2000	[40,104]
Arctic sills	3.6 ± 0.6	2004, 2010	[40,41,80]
Gibraltar Strait	0.15 ± 0.01	2005-2008	[81]
DOP	3 ± 1		***

* See Supplementary Methods for derivation of the values; ** Period of time the value accounts for; *** This study.

Table S7. Nutrient time series observation-period tendencies. Linear-fit ± standard error (% explained by the driver, i.e., transport or nutrient concentration). [linear-fit F_N]$_{transport}$ accounts for the contribution due to the change in transport and [linear-fit F_N]$_{nutrient}$ for the contribution due to the change in nutrient concentration. Average nutrient transports, avg(F_N), are also shown for reference. Positive (negative) mean nutrient transports indicate northward (southwards) flux. Positive (negative) tendencies refer to an increase (decrease) of the nutrient transports to the North over the period of study.

		avg(F_N) *($kmol\ s^{-1}$)*	**linear-fit F_N** *($kmol\ s^{-1}\ yr^{-1}$)*	**[linear-fit F_N]$_{transport}$** *($kmol\ s^{-1}\ yr^{-1}$)*	**[linear-fit F_N]$_{nutrient}$** *($kmol\ s^{-1}\ yr^{-1}$)*
Total fraction					
Silicate	*Total*	-384.2	7.6 ± 1.6	4.9 ± 1.6 (65%)	2.7 ± 0.1 (35%)
	Overturning	-439.9	5.7 ± 1.6	5.3 ± 1.5 (92%)	0.4 ± 0.1 (8%)
	Horizontal	88.8	1.8 ± 0.1	-0.2 ± 0.2 (13%)	2.0 ± 0.1 (87%)
	Throughflow	-32.9	0.01 ± 0.07	-0.01 ± 0.07 (39%)	0.02 ± 0.01 (61%)
Nitrate	*Total*	-169.5	9.4 ± 0.85	1.3 ± 0.8 (14%)	8.1 ± 0.1 (86%)
	Overturning	-286.5	1.9 ± 0.9	1.8 ± 0.9 (96%)	0.07 ± 0.02 (4%)
	Horizontal	141.1	7.4 ± 0.2	-0.5 ± 0.2 (7%)	7.9 ± 0.1 (93%)
	Throughflow	-23.8	-0.01 ± 0.05	-0.01 ± 0.05 (73%)	-0.004 ± 0.001 (27%)
Phosphate	*Total*	-11.8	0.58 ± 0.06	0.10 ± 0.06 (17%)	0.48 ± 0.01 (83%)
	Overturning	-19.9	0.15 ± 0.06	0.14 ± 0.06 (91%)	0.01 ± 0.01 (9%)
	Horizontal	9.6	0.43 ± 0.01	-0.03 ± 0.01 (7%)	0.46 ± 0.01 (93%)
	Throughflow	-1.6	-0.0004±0.0034	-0.0007±0.0034 (68%)	0.0003 ± 0.0001 (32%)
Remineralized fraction					
Nitrate	*Total*	0.8	3.6 ± 0.3	0.1 ± 0.3 (3%)	3.5 ± 0.1 (97%)
	Overturning	-81.3	0.5 ± 0.3	0.3 ± 0.3 (69%)	0.2 ± 0.1 (31%)
	Horizontal	90.3	3.2 ± 0.1	-0.2 ± 0.1 (6%)	3.4 ± 0.1 (94%)
	Throughflow	-9.2	-0.008±0.020	-0.004 ± 0.020 (50%)	-0.004 ± 0.001 (50%)
Phosphate	*Total*	0.0	0.22 ± 0.02	0.01 ± 0.02 (3%)	0.21 ± 0.01 (97%)
	Overturning	-4.9	0.03 ± 0.02	0.02 ± 0.02 (69%)	0.01 ± 0.01 (31%)
	Horizontal	5.4	0.19 ± 0.01	-0.01 ± 0.01 (6%)	0.20 ± 0.01 (94%)
	Throughflow	-0.6	-0.0004±0.0012	-0.0002±0.0012 (50%)	-0.0002±0.0001 (50%)
Preformed fraction					
Nitrate	*Total*	-170.3	5.8 ± 0.6	1.2 ± 1 (20%)	4.6 ± 0.1 (80%)
	Overturning	-205.2	1.4 ± 0.6	1.5 ± 0.6 (95%)	-0.07 ± 0.02 (5%)
	Horizontal	50.8	4.2 ± 0.1	-0.3 ± 0.1 (7%)	4.5 ± 0.1 (93%)
	Throughflow	-14.6	-0.01 ± 0.03	-0.01 ± 0.03 (98%)	0 ± 0 (2%)
Phosphate	*Total*	-11.9	0.36 ± 0.04	0.09 ± 0.04 (25%)	0.27 ± 0.01 (75%)
	Overturning	-15.0	0.12 ± 0.04	0.12 ± 0.04 (96%)	0 ± 0 (4%)
	Horizontal	4.2	0.23 ± 0.01	-0.02 ± 0.01 (8%)	0.25 ± 0.01 (92%)
	Throughflow	-1.0	0.0001 ± 0.002	-0.0005±0.0022 (44%)	0.0006±0.0001 (56%)

Table S8. MLR coefficients and statistics. MLR equation is shown in the upper row of the table. MLR No. refers to the specific region in which MLR was applied (MLR-box, fig. S1b). No. Obs. refers to the number of observations by each MLR-box. RMSE is the root mean square error. R^2 is the coefficient of multiple determination, and represents the percentage of the response variable (per one percent) that is explained by the regression model. ct. is the constant (offset) term, and c1 to c6 are the regression coefficients. Summary for (**A**) silicate, (**B**) nitrate (next page), (**C**) phosphate (next page).

$[Si(OH)_4]_{obs}$ – Residual = ct. + c1 θ_{hydro} + c2 S_{hydro} + c3 O_{2hydro} + c4 P_{hydro} + c5 lon_{hydro} + c6 $time_{hydro}$

MLR No.	No. Obs.	RMSE	R^2	ct.	c1	c2	c3	c4	c5	c6
Mixed layer										
2	693	2.41E-06	0.80	-3.85E-04	-5.39E-07	7.30E-09	-5.01E-06	-	-	-
3	368	2.14E-07	0.46	-1.98E-05	5.99E-08	-	-7.40E-09	1.44E-06	-	-4.66E-11
4	413	2.25E-07	0.33	2.22E-05	-2.80E-08	-9.83E-10	-1.43E-08	-1.64E-07	-	-2.11E-11
West western basin										
5	509	2.27E-07	0.41	1.17E-05	-1.66E-07	-8.32E-10	5.11E-09	6.05E-07	-1.80E-08	-3.54E-11
6	999	3.19E-07	0.70	5.87E-05	7.81E-08	4.00E-09	1.42E-08	-1.04E-06	-	-2.86E-11
7	464	4.95E-07	0.99	-5.16E-04	-4.08E-06	-5.60E-09	-	1.71E-05	-5.28E-08	-2.79E-11
8	189	3.84E-07	0.77	1.02E-03	5.19E-07	-	4.78E-08	-2.63E-05	-2.40E-08	-9.96E-11
9	192	3.23E-07	0.88	2.79E-04	-8.92E-07	-	5.40E-08	-4.83E-06	-7.45E-08	-9.65E-11
10	664	6.92E-07	0.90	-7.60E-04	-6.05E-06	2.17E-09	3.15E-08	2.60E-05	-1.98E-07	-8.26E-11
11	619	7.60E-07	0.94	4.59E-03	-	3.20E-09	8.04E-08	-1.25E-04	-4.61E-07	-1.10E-10
12	352	1.49E-06	0.92	1.84E-02	-	-	1.26E-07	-5.16E-04	-2.80E-07	-4.07E-10
East western basin										
13	79	6.54E-07	0.99	1.57E-02	2.66E-06	9.49E-10	-	-4.43E-04	-3.35E-07	-1.28E-10
14	1139	2.94E-07	0.74	4.32E-05	1.45E-07	5.54E-09	1.42E-08	-1.02E-06	-	-1.05E-11
15	773	6.99E-07	0.97	-2.89E-04	-2.74E-06	1.58E-09	-3.39E-08	1.06E-05	-5.84E-08	-5.51E-11
16	422	6.17E-07	0.83	1.02E-03	9.19E-07	7.09E-09	6.15E-08	-2.67E-05	-2.03E-08	-9.34E-11
17	296	4.87E-07	0.91	5.05E-04	-	2.83E-09	6.08E-08	-1.14E-05	-8.31E-08	-9.48E-11
18	876	9.43E-07	0.96	7.23E-04	-5.27E-06	5.93E-09	8.28E-08	-1.45E-05	-2.80E-07	-1.56E-10
19	846	1.20E-06	0.95	7.54E-03	2.41E-06	1.39E-09	1.94E-07	-2.08E-04	-5.07E-07	-1.48E-10
20	482	1.02E-06	0.98	1.41E-02	4.02E-06	-	2.00E-07	-3.96E-04	-3.62E-07	-1.85E-10
West eastern basin										
21	437	8.84E-07	0.95	1.65E-02	4.96E-06	-	3.10E-08	-4.72E-04	-1.05E-07	-
22	527	3.08E-07	0.68	7.84E-05	2.24E-07	5.29E-09	2.14E-08	-1.30E-06	-7.57E-09	-4.42E-11
23	614	7.43E-07	0.96	-5.23E-04	-3.68E-06	-	-1.63E-08	1.81E-05	-5.74E-08	-8.60E-11
24	297	6.65E-07	0.86	8.28E-04	-	2.34E-09	9.05E-08	-2.05E-05	-1.99E-08	-1.16E-10
25	262	6.19E-07	0.66	6.27E-04	-	2.21E-09	1.38E-07	-1.44E-05	-4.50E-08	-1.24E-10
26	501	8.71E-07	0.94	4.89E-04	-2.48E-06	9.73E-09	5.36E-08	-9.12E-06	-1.60E-07	-1.59E-10
27	524	8.42E-07	0.97	7.63E-03	3.37E-06	2.03E-09	9.53E-08	-2.14E-04	-1.83E-07	-1.13E-10
28	268	7.75E-07	0.81	7.03E-03	5.21E-06	1.55E-09	1.14E-07	-1.99E-04	-1.72E-07	-
East eastern basin										
29	208	6.72E-07	0.54	2.99E-03	4.35E-06	5.25E-10	8.90E-08	-8.63E-05	1.13E-07	4.85E-11
30	391	2.84E-07	0.83	4.97E-05	-	-	2.25E-08	-5.06E-07	-3.12E-08	-3.16E-11
31	828	5.72E-07	0.98	-5.47E-04	-3.81E-06	-1.03E-09	-	1.85E-05	-6.76E-08	-6.44E-11
32	379	4.68E-07	0.93	4.56E-04	-1.89E-06	-	6.73E-08	-9.24E-06	-2.50E-08	-1.27E-10
33	257	5.63E-07	0.81	6.69E-04	-	5.92E-09	1.63E-07	-1.58E-05	-2.44E-08	-1.24E-10
34	438	6.81E-07	0.96	5.12E-04	-1.27E-06	1.06E-08	2.24E-07	-1.05E-05	-1.28E-07	-1.37E-10
35	477	7.42E-07	0.98	5.29E-03	2.04E-06	4.48E-09	6.37E-08	-1.47E-04	-2.42E-07	-1.05E-10
36	212	7.28E-07	0.67	4.61E-03	3.58E-06	1.60E-09	5.60E-08	-1.30E-04	-	-4.88E-11

Table S8. MLR coefficients and statistics. (**B**) Summary for nitrate.

$[NO_3^-]_{obs}$ – Residual = ct. + c1 θ_{hydro} + c2 S_{hydro} + c3 O_{2hydro} + c4 P_{hydro} + c5 lon_{hydro} + c6 $time_{hydro}$

MLR No.	No. Obs.	RMSE	R^2	ct.	c1	c2	c3	c4	c5	c6
Mixed layer										
2	810	2.54E-06	0.94	-3.60E-04	-1.34E-06	6.91E-09	-4.96E-06	-	-	-
3	464	9.67E-08	0.08	-2.99E-06	-1.51E-08	-	5.29E-09	7.00E-08	-6.72E-09	3.64E-12
4	535	1.37E-07	0.26	5.06E-06	-3.73E-08	4.13E-10	-	-	-1.94E-08	-
West western basin										
5	745	2.14E-07	0.52	4.62E-05	-1.70E-07	9.45E-10	-2.06E-08	-6.63E-07	-3.33E-08	-1.49E-11
6	1153	5.25E-07	0.95	1.76E-04	-1.31E-07	9.03E-09	2.92E-08	-5.63E-06	-3.26E-08	5.72E-11
7	506	5.74E-07	0.99	3.14E-04	-8.42E-07	-5.04E-09	-	-8.56E-06	-8.18E-08	4.98E-11
8	223	5.60E-07	0.73	9.59E-04	9.93E-07	-1.95E-09	4.90E-08	-2.64E-05	-4.74E-08	-
9	251	5.63E-07	0.78	1.07E-03	-	-	5.42E-08	-2.91E-05	-9.62E-08	-
10	729	5.28E-07	0.17	2.84E-04	6.77E-07	7.82E-10	2.88E-08	-7.87E-06	-5.02E-08	2.92E-11
11	665	4.61E-07	0.35	4.26E-04	1.44E-06	1.06E-09	3.74E-08	-1.21E-05	-8.94E-08	4.94E-11
12	392	8.14E-07	0.56	2.59E-03	9.79E-07	7.01E-10	-	-7.35E-05	-6.24E-08	-
East western basin										
13	82	4.32E-07	0.88	2.35E-03	7.73E-07	7.81E-10	-	-6.65E-05	-6.88E-08	-
14	1234	6.62E-07	0.93	8.30E-05	2.68E-07	2.05E-08	5.79E-08	-3.35E-06	-7.43E-09	5.14E-11
15	822	6.46E-07	0.99	1.88E-04	-9.23E-07	3.52E-09	-	-4.23E-06	-1.22E-07	1.30E-11
16	436	5.88E-07	0.77	3.30E-04	-7.25E-07	2.53E-09	-	-7.43E-06	-1.19E-07	-2.80E-11
17	344	4.39E-07	0.93	4.60E-04	-	-	2.68E-08	-1.15E-05	-8.54E-08	-2.01E-11
18	916	4.32E-07	0.63	4.94E-04	9.50E-07	1.60E-09	3.83E-08	-1.33E-05	-5.61E-08	-
19	877	4.46E-07	0.75	1.65E-03	2.26E-06	-	3.96E-08	-4.67E-05	-9.12E-08	2.56E-11
20	501	4.59E-07	0.86	2.47E-03	2.33E-06	-	3.41E-08	-7.04E-05	-7.67E-08	2.88E-11
West eastern basin										
21	458	4.90E-07	0.64	1.50E-03	3.38E-07	-	-	-4.11E-05	-1.39E-07	-2.01E-11
22	614	7.09E-07	0.91	2.05E-04	7.42E-07	2.43E-08	6.59E-08	-5.25E-06	-1.98E-08	-2.89E-11
23	680	5.03E-07	0.99	1.56E-04	-7.54E-07	8.67E-09	1.95E-08	-2.68E-06	-1.16E-07	-2.55E-11
24	366	5.34E-07	0.77	6.49E-04	5.34E-07	3.49E-09	4.06E-08	-1.62E-05	-7.79E-08	-6.44E-11
25	345	3.82E-07	0.91	5.79E-04	9.31E-07	-	5.05E-08	-1.46E-05	-5.59E-08	-4.81E-11
26	602	3.05E-07	0.65	4.43E-04	-	-	2.53E-08	-1.05E-05	-7.47E-08	-4.80E-11
27	600	2.82E-07	0.75	1.08E-03	9.81E-07	1.78E-10	7.30E-09	-2.90E-05	-6.61E-08	-4.28E-11
28	295	2.78E-07	0.54	1.12E-03	4.88E-07	-	1.29E-08	-3.00E-05	-7.28E-08	-4.32E-11
East eastern basin										
29	220	2.72E-07	0.31	-5.68E-04	3.36E-07	1.45E-10	-	1.75E-05	-	-2.97E-11
30	516	7.00E-07	0.92	1.36E-04	-2.73E-07	-	-	-2.50E-06	-1.07E-07	-1.98E-11
31	982	3.88E-07	1.00	6.33E-05	-1.71E-06	-	-	-	-1.16E-07	-8.35E-12
32	496	4.29E-07	0.92	6.36E-04	-	-	3.25E-08	-1.56E-05	-6.86E-08	-6.61E-11
33	358	3.09E-07	0.92	6.35E-04	1.05E-06	-	2.17E-08	-1.60E-05	-4.21E-08	-6.03E-11
34	583	2.91E-07	0.74	8.01E-04	1.93E-06	4.50E-10	4.00E-08	-2.14E-05	-3.95E-08	-3.54E-11
35	565	2.62E-07	0.85	1.05E-03	1.97E-06	7.23E-10	2.98E-08	-2.89E-05	-4.62E-08	-1.20E-11
36	233	2.47E-07	0.34	8.42E-04	9.00E-07	-	-	-2.30E-05	-	-2.39E-11

Table S8. MLR coefficients and statistics. (**C**) Summary for phosphate.

$[PO_4^{3-}]_{obs}$ – Residual = ct. + c1 θ_{hydro} + c2 S_{hydro} + c3 O_{2hydro} + c4 P_{hydro} + c5 lon_{hydro} + c6 $time_{hydro}$										
MLR No.	**No. Obs.**	**RMSE**	**R^2**	**ct.**	**c1**	**c2**	**c3**	**c4**	**c5**	**c6**
Mixed layer										
2	805	1.84E-07	0.93	-2.88E-05	-8.53E-08	4.80E-10	-3.43E-07	-	-	5.08E-12
3	411	1.63E-08	0.07	9.93E-07	-5.96E-09	-5.38E-11	-	-	-1.22E-09	-7.89E-13
4	453	1.91E-08	0.13	1.40E-06	-4.57E-09	-6.24E-11	1.34E-09	-3.23E-08	-	-
West western basin										
5	608	4.79E-08	0.35	6.61E-07	-2.86E-08	-2.36E-10	3.21E-09	-	-7.64E-09	2.42E-12
6	1075	3.83E-08	0.89	1.02E-05	2.41E-09	6.06E-10	1.37E-09	-3.05E-07	-7.27E-10	1.64E-12
7	502	2.97E-08	0.99	1.87E-06	-1.29E-07	-1.19E-10	-1.24E-09	-	-6.04E-09	2.44E-12
8	231	3.72E-08	0.70	4.45E-05	-	-	-	-1.17E-06	-5.16E-09	-1.10E-12
9	261	2.91E-08	0.85	3.51E-05	-1.62E-07	-1.59E-10	-	-8.45E-07	-9.38E-09	-1.26E-12
10	745	3.66E-08	0.11	1.91E-05	-	3.29E-11	-	-4.80E-07	-4.20E-09	-
11	635	2.54E-08	0.43	-2.57E-05	-3.55E-08	5.86E-11	-	8.24E-07	-6.98E-09	-
12	385	4.28E-08	0.69	1.08E-04	-1.16E-07	4.64E-11	-	-2.96E-06	-5.48E-09	-3.12E-12
East western basin										
13	75	2.37E-08	0.90	1.18E-04	-9.22E-08	4.16E-11	-	-3.23E-06	-5.54E-09	-3.55E-12
14	996	3.99E-08	0.90	6.36E-06	2.83E-08	1.25E-09	3.70E-09	-1.97E-07	-9.92E-10	7.71E-13
15	731	3.15E-08	0.99	-4.32E-06	-1.50E-07	-	-2.23E-09	2.15E-07	-6.90E-09	7.95E-13
16	384	2.31E-08	0.91	4.37E-05	-	9.13E-11	2.19E-09	-1.15E-06	-5.46E-09	-1.04E-12
17	333	2.30E-08	0.96	2.38E-05	-5.68E-08	-	6.54E-10	-5.48E-07	-7.32E-09	-1.63E-12
18	825	2.16E-08	0.77	4.42E-06	-7.11E-08	2.40E-11	-	-	-6.17E-09	-1.84E-12
19	773	2.46E-08	0.84	2.19E-05	-1.25E-07	-2.78E-11	2.29E-09	-4.71E-07	-7.32E-09	-2.24E-12
20	418	2.21E-08	0.93	1.07E-04	-7.35E-08	-	2.85E-09	-2.92E-06	-5.40E-09	-3.31E-12
West eastern basin										
21	375	2.04E-08	0.82	1.26E-04	-9.44E-08	9.16E-12	7.35E-10	-3.48E-06	-2.98E-09	-3.40E-12
22	332	4.63E-08	0.84	4.26E-06	-	1.15E-09	5.58E-09	-4.83E-08	-2.17E-09	-2.60E-12
23	459	4.82E-08	0.98	-6.00E-06	-1.38E-07	3.50E-10	-	3.26E-07	-6.97E-09	-2.68E-12
24	275	2.70E-08	0.89	3.89E-05	-	3.48E-10	2.82E-09	-9.57E-07	-6.01E-09	-3.85E-12
25	278	2.60E-08	0.92	3.23E-05	-	-	1.71E-09	-7.67E-07	-5.85E-09	-3.60E-12
26	433	2.74E-08	0.57	3.42E-05	-3.07E-08	-	2.09E-09	-8.23E-07	-6.53E-09	-3.08E-12
27	424	2.29E-08	0.71	8.04E-05	8.98E-08	1.96E-11	7.88E-10	-2.21E-06	-5.29E-09	-8.13E-13
28	246	2.40E-08	0.53	1.11E-04	1.05E-07	-	-	-3.10E-06	-7.77E-09	-
East eastern basin										
29	170	1.90E-08	0.40	1.47E-06	8.53E-08	1.12E-11	2.47E-09	-	-4.15E-09	1.35E-12
30	388	5.00E-08	0.86	6.12E-06	-1.20E-08	-	5.82E-09	-1.18E-07	-6.03E-09	-
31	776	3.57E-08	0.99	-9.85E-06	-1.64E-07	8.49E-11	8.91E-10	4.39E-07	-7.40E-09	-2.18E-12
32	412	3.23E-08	0.89	3.12E-05	-4.63E-08	1.29E-10	-	-6.98E-07	-5.72E-09	-5.23E-12
33	317	2.91E-08	0.85	3.45E-05	-	-	-	-8.06E-07	-4.80E-09	-4.91E-12
34	484	2.76E-08	0.63	7.79E-05	2.10E-07	6.71E-11	5.32E-09	-2.15E-06	-1.63E-09	-2.03E-12
35	469	2.64E-08	0.79	9.97E-05	2.04E-07	5.34E-11	3.22E-09	-2.80E-06	-4.14E-09	-
36	188	2.76E-08	0.23	1.03E-04	1.07E-07	-	2.20E-09	-2.91E-06	-	-

Table S9. Nutrient and oxygen in situ-data 1981-2015 trends. Nutrients ($Si(OH)_4$, NO_3^-, PO_4^{3-}), oxygen (O_2), apparent oxygen utilization (AOU), and saturation oxygen (O_2sat) change rates (± standard error), in µmol kg^{-1} y^{-1}, estimated in density ranges (delimiting main water masses) at 24.5°N, from hydrographic data (ref. table S1). Superscript 0 (remin.) refers to the preformed (remineralized) nutrient fraction. Note that just those trends significant at 95% of confidence were considered. The standard error or the fitted lines were taken as a measure of the uncertainty. UNACW, Upper North-Atlantic Central Water (γ<26.76 kg m^{-3}); LNACW, Lower North-Atlantic Central Water (26.75 < γ< 27.25 kg m^{-3}); AAIW, Antarctic Intermediate Water (27.25 < γ< 27.65 kg m^{-3}); UNADW, Upper North Atlantic Deep Water (27.65 < γ< 28 kg m^{-3}); LNADW, Lower North Atlantic Deep Water (28 < γ< 28.08 kg m^{-3}); and AABW, Antarctic Bottom Water (γ>28.08 kg m^{-3}). γ refers to neutral density[94]**.**

Water mass	**$Si(OH)_4$**	**NO_3^-**	**$[NO_3]^0$**	**$[NO_3]^{remin-}$**	**PO_4^{3-}**	**$[PO_4^{3-}]^0$**	**$[PO_4^{3-}]^{remin.}$**	**O_2**	**AOU**	**O_2sat**
Florida Straits										
UNACW	-0.066 ± 0.009	-0.10 ± 0.03	-0.03 ± 0.01	-0.07 ± 0.02	-0.006 ± 0.002	-0.0017 ± 0.0006	-0.004 ± 0.001	0.27 ± 0.20	-0.71 ± 0.20	-0.44 ± 0.10
LNACW	-0.05 ± 0.05	-	-	-	-	-	-	0.29 ± 0.10	-	-
AAIW	-0.10 ± 0.05	-	-	-	-	-	-	-0.19 ± 0.20	-	-
Western Atlantic Basin										
UNACW	-0.013 ± 0.001	-	-0.003 ± 0.002	-	-0.0005 ± 0.0003	-	-	-0.09 ± 0.02	-	-0.10 ± 0.02
LNACW	-	0.073 ± 0.010	0.028 ± 0.008	0.044 ± 0.006	0.0038 ± 0.0009	0.0013 ± 0.0005	0.0027 ± 0.0004	-0.41 ± 0.04	0.46 ± 0.06	0.06 ± 0.03
AAIW	-0.036 ± 0.007	-	-0.006 ± 0.004	0.010 ± 0.003	0.0015 ± 0.0004	0.0008 ± 0.0003	0.0006 ± 0.0002	-0.08 ± 0.04	0.11 ± 0.03	0.03 ± 0.02
UNADW	-0.045 ± 0.007	-	0.011 ± 0.002	-0.008 ± 0.004	-	0.0002 ± 0.0001	-0.0005 ± 0.0002	0.10 ± 0.05	-0.08 ± 0.04	0.02 ± 0.01
LNADW	-0.085 ± 0.020	0.008 ± 0.003	0.011 ± 0.002	-0.004 ± 0.002	0.0002 ± 0.0002	0.0003 ± 0.0001	-0.0002 ± 0.0001	0.03 ± 0.02	-0.04 ± 0.02	-
AABW	-0.031 ± 0.030	0.008 ± 0.004	0.004 ± 0.003	0.003 ± 0.002	0.0009 ± 0.0003	0.0006 ± 0.0002	0.0002 ± 0.0001	-0.03 ± 0.02	0.03 ± 0.02	0.003 ± 0.002
Eastern Atlantic Basin										
UNACW	-0.014 ± 0.002	-0.013 ± 0.006	-0.011 ± 0.002	-	-0.0009 ± 0.0004	0.0003 ± 0.0002	-	-0.07 ± 0.04	-	-0.10 ± 0.02
LNACW	-0.024 ± 0.006	0.02 ± 0.01	-	0.02 ± 0.006	-	-0.0012 ± 0.0005	0.0012 ± 0.0004	-0.24 ± 0.05	0.21 ± 0.07	-0.03 ± 0.02
AAIW	-0.038 ± 0.009	-	-0.02 ± 0.004	0.021 ± 0.003	-	-0.0009 ± 0.0004	0.0013 ± 0.0002	-0.18 ± 0.04	0.22 ± 0.04	0.04 ± 0.02
UNADW	-0.020 ± 0.009	-0.015 ± 0.004	-0.023 ± 0.002	0.009 ± 0.004	-0.0016 ± 0.0003	-0.0017 ± 0.0001	0.0005 ± 0.0002	-0.12 ± 0.06	0.10 ± 0.04	-
LNADW	-0.035 ± 0.02	-0.011 ± 0.002	-0.019 ± 0.001	0.008 ± 0.001	-0.0010 ± 0.0002	-0.0012 ± 0.0001	0.0005 ± 0.0001	-0.09 ± 0.01	0.09 ± 0.01	-
AABW	-0.031 ± 0.005	-0.019 ± 0.002	-0.024 ± 0.002	0.006 ± 0.001	-0.0006 ± 0.0002	-0.00093 ± 0.0002	0.0004 ± 0.0001	-0.064 ± 0.008	0.068 ± 0.008	0.003 ± 0.002

Table S10. Total annual nutrient transports. Annual (April to March) averages (and standard deviation, in parenthesis) of the total transport across the 26.5°N section (total) and throughflow, overturning and horizontal components for the transport of (**A**) silicate, nitrate and phosphate, and (**B**) the remineralized and preformed fractions of nitrate and phosphate. % change is the percentage of change of the nutrient transport magnitude between the end and the beginning of the period.

A

	Silicate (kmol s^{-1})				**Nitrate (kmol s^{-1})**				**Phosphate (kmol s^{-1})**			
	throughflow	*overturning*	*horizontal*	*total*	*throughflow*	*overturning*	*horizontal*	*total*	*throughflow*	*overturning*	*horizontal*	*total*
2004	-34 (7)	-461 (167)	78 (11)	-417 (169)	-25 (5)	-288 (94)	94 (16)	-219 (92)	-1.6 (0.3)	-20 (6)	7 (1)	-15 (6)
2005	-38 (6)	-558 (146)	86 (30)	-510 (153)	-27 (4)	-326 (77)	100 (19)	-253 (79)	-1.8 (0.3)	-23 (5)	7 (1)	-17 (5)
2006	-37 (5)	-540 (118)	79 (8)	-498 (122)	-27 (4)	-325 (68)	106 (12)	-245 (70)	-1.8 (0.2)	-23 (5)	8 (1)	-17 (5)
2007	-35 (5)	-484 (126)	83 (9)	-436 (129)	-25 (4)	-308 (68)	116 (14)	-217 (67)	-1.7 (0.2)	-21 (5)	8 (1)	-15 (4)
2008	-34 (5)	-460 (112)	82 (9)	-413 (111)	-25 (4)	-296 (82)	120 (16)	-201 (76)	-1.6 (0.3)	-20 (5)	8 (1)	-14 (5)
2009	-28 (7)	-291 (175)	83 (9)	-236 (179)	-20 (5)	-219 (93)	129 (14)	-110 (93)	-1.3 (0.3)	-15 (6)	9 (1)	-8 (6)
2010	-33 (6)	-403 (143)	88 (10)	-349 (145)	-24 (4)	-282 (79)	135 (14)	-171 (78)	-1.6 (0.3)	-20 (5)	9 (1)	-12 (5)
2011	-35 (4)	-452 (103)	85 (8)	-402 (105)	-25 (3)	-303 (62)	137 (12)	-192 (61)	-1.7 (0.2)	-21 (4)	9 (1)	-13 (4)
2012	-30 (7)	-317 (162)	85 (13)	-263 (164)	-22 (5)	-241 (98)	144 (21)	-118 (93)	-1.4 (0.3)	-17 (7)	10 (1)	-8 (6)
2013	-35 (5)	-468 (104)	89 (12)	-413 (106)	-25 (3)	-303 (65)	156 (19)	-173 (62)	-1.7 (0.2)	-21 (4)	10 (1)	-12 (4)
2014	-32 (4)	-415 (110)	94 (12)	-353 (110)	-23 (3)	-265 (57)	162 (20)	-126 (56)	-1.5 (0.2)	-18 (4)	11 (1)	-9 (4)
2015	-32 (5)	-421 (118)	96 (10)	-357 (119)	-23 (4)	-271 (73)	174 (18)	-120 (68)	-1.5 (0.2)	-19 (5)	11 (1)	-9 (5)
2016	-33 (5)	-432 (117)	106 (16)	-359 (112)	-24 (4)	-285 (75)	191 (26)	-119 (65)	-1.6 (0.2)	-20 (5)	13 (2)	-9 (4)
2017	-34 (8)	-434 (178)	101 (10)	-367 (184)	-24 (6)	-285 (98)	183 (16)	-126 (104)	-1.6 (0.4)	-20 (7)	12 (1)	-9 (7)
% change	8	13	35	21	7	6	117	54	7	7	92	49

B

	Remineralized nitrate (kmol s^{-1})				**Remineralized phosphate (kmol s^{-1})**			
	throughflow	*overturning*	*horizontal*	*total*	*throughflow*	*overturning*	*horizontal*	*total*
2004	-9.5 (1.9)	-81 (34)	73 (10)	-17 (31)	-0.57 (0.11)	-4.9 (2)	4.4 (0.6)	-1 (1.8)
2005	-10.5 (1.7)	-89 (27)	76 (12)	-24 (26)	-0.63 (0.1)	-5.4 (1.6)	4.6 (0.7)	-1.4 (1.6)
2006	-10.3 (1.4)	-91 (25)	74 (8)	-27 (26)	-0.62 (0.08)	-5.5 (1.5)	4.5 (0.5)	-1.6 (1.6)
2007	-9.8 (1.4)	-89 (24)	79 (7)	-20 (23)	-0.59 (0.08)	-5.4 (1.4)	4.7 (0.4)	-1.2 (1.4)
2008	-9.6 (1.5)	-85 (32)	80 (10)	-14 (28)	-0.58 (0.09)	-5.1 (1.9)	4.8 (0.6)	-0.9 (1.7)
2009	-7.9 (1.9)	-63 (33)	84 (8)	13 (32)	-0.47 (0.11)	-3.8 (2)	5 (0.5)	0.8 (1.9)
2010	-9.3 (1.7)	-80 (28)	87 (11)	-3 (27)	-0.56 (0.1)	-4.8 (1.7)	5.2 (0.7)	-0.2 (1.6)
2011	-9.8 (1.2)	-89 (23)	86 (7)	-13 (23)	-0.59 (0.07)	-5.4 (1.4)	5.2 (0.4)	-0.8 (1.4)
2012	-8.4 (1.9)	-69 (35)	89 (12)	11 (32)	-0.5 (0.12)	-4.2 (2.1)	5.3 (0.7)	0.7 (1.9)
2013	-9.7 (1.3)	-89 (25)	94 (11)	-5 (23)	-0.58 (0.08)	-5.3 (1.5)	5.6 (0.7)	-0.3 (1.4)
2014	-9.1 (1.1)	-72 (22)	97 (11)	16 (23)	-0.54 (0.07)	-4.3 (1.3)	5.8 (0.7)	1 (1.4)
2015	-9.1 (1.4)	-74 (27)	103 (12)	20 (26)	-0.55 (0.08)	-4.4 (1.6)	6.2 (0.7)	1.2 (1.6)
2016	-9.3 (1.4)	-81 (28)	115 (17)	25 (23)	-0.56 (0.08)	-4.8 (1.7)	6.9 (1)	1.5 (1.4)
2017	-9.5 (2.2)	-80 (33)	112 (11)	22 (34)	-0.57 (0.13)	-4.8 (2)	6.7 (0.6)	1.3 (2)
% change	6	4	69	202	6	4	69	202

	Preformed nitrate (kmol s^{-1})				**Preformed phosphate (kmol s^{-1})**			
	throughflow	*overturning*	*horizontal*	*total*	*throughflow*	*overturning*	*horizontal*	*total*
2004	-15 (3)	-208 (61)	21 (8)	-202 (64)	-1.06 (0.2)	-15.3 (4.5)	2.7 (0.6)	-13.7 (4.6)
2005	-17 (3)	-237 (51)	24 (8)	-230 (55)	-1.16 (0.18)	-17.5 (3.8)	2.8 (0.6)	-15.9 (3.9)
2006	-16 (2)	-233 (44)	32 (7)	-218 (46)	-1.14 (0.15)	-17.2 (3.2)	3.1 (0.5)	-15.2 (3.2)
2007	-15 (2)	-219 (45)	37 (8)	-197 (46)	-1.08 (0.15)	-16 (3.2)	3.5 (0.6)	-13.6 (3.2)
2008	-15 (2)	-211 (51)	40 (8)	-186 (49)	-1.06 (0.16)	-15.4 (3.6)	3.6 (0.6)	-12.9 (3.4)
2009	-12 (3)	-156 (60)	46 (7)	-123 (62)	-0.87 (0.21)	-11.3 (4.3)	3.8 (0.5)	-8.4 (4.4)
2010	-15 (3)	-202 (52)	49 (8)	-168 (53)	-1.03 (0.19)	-14.7 (3.7)	4.1 (0.5)	-11.6 (3.7)
2011	-16 (2)	-214 (40)	50 (7)	-179 (39)	-1.08 (0.13)	-15.5 (2.9)	4.1 (0.5)	-12.5 (2.8)
2012	-13.3 (3)	-171 (64)	55 (9)	-129 (62)	-0.93 (0.21)	-12.4 (4.5)	4.3 (0.7)	-9 (4.4)
2013	-15.3 (2)	-215 (41)	62 (9)	-168 (40)	-1.07 (0.14)	-15.6 (3)	4.7 (0.7)	-11.9 (2.9)
2014	-14.3 (1.8)	-193 (38)	65 (10)	-142 (36)	-1 (0.12)	-14.1 (2.7)	4.9 (0.8)	-10.2 (2.6)
2015	-14.4 (2.2)	-197 (47)	71 (8)	-140 (44)	-1 (0.15)	-14.4 (3.4)	5.3 (0.6)	-10.1 (3.1)
2016	-14.7 (2.2)	-205 (48)	75 (9)	-144 (44)	-1.02 (0.15)	-15 (3.4)	5.8 (0.7)	-10.2 (3.1)
2017	-15 (3.5)	-204 (66)	71 (8)	-148 (71)	-1.04 (0.24)	-14.9 (4.7)	5.5 (0.5)	-10.4 (5)
% change	7	6	260	36	8	8	126	32